MAX-PLANCK-INSTITUT
FÜR METEOROLOGIE

International Max Planck Research School on Earth System Modelling

Measuring and modeling of methane emissions from ponds in high latitudes

Zoé Rehder

Hamburg 2022

Berichte zur Erdsystemforschung 252
Reports on Earth System Science 2022

Hinweis

Die Berichte zur Erdsystemforschung werden vom Max-Planck-Institut für Meteorologie in Hamburg in unregelmäßiger Abfolge herausgegeben.

Sie enthalten wissenschaftliche und technische Beiträge, inklusive Dissertationen.

Die Beiträge geben nicht notwendigerweise die Auffassung des Instituts wieder.

Die "Berichte zur Erdsystemforschung" führen die vorherigen Reihen "Reports" und "Examensarbeiten" weiter.

Anschrift / Address

Max-Planck-Institut für Meteorologie
Bundesstrasse 53
20146 Hamburg
Deutschland

Tel./Phone: +49 (0)40 4 11 73 - 0
Fax: +49 (0)40 4 11 73 - 298

name.surname@mpimet.mpg.de
www.mpimet.mpg.de

Notice

The Reports on Earth System Science are published by the Max Planck Institute for Meteorology in Hamburg. They appear in irregular intervals.

They contain scientific and technical contributions, including PhD theses.

The Reports do not necessarily reflect the opinion of the Institute.

The "Reports on Earth System Science" continue the former "Reports" and "Examensarbeiten" of the Max Planck Institute.

Layout

Bettina Diallo and Norbert P. Noreiks
Communication

Copyright

Measuring and modeling of methane emissions from ponds in high latitudes

Zoé Rehder

Hamburg 2022

Zoé Rehder

Max-Planck-Institut für Meteorologie
The International Max Planck Research School on Earth System Modelling
(IMPRS-ESM)
Bundesstrasse 53
20146 Hamburg

Tag der Disputation: 29. April 2022

Folgende Gutachter empfehlen die Annahme der Dissertation:
Prof. Dr. Victor Brovkin
Prof. Dr. Lars Kutzbach

Vorsitzender des Promotionsausschusses:
Prof. Dr. Hermann Held

Dekan der MIN-Fakultät:
Prof. Dr. Heinrich Graener

Titelphoto: Zoé Rehder

Berichte zur Erdsystemforschung / Max-Planck-Institut für Meteorologie 252
Reports on Earth System Science / Max Planck Institute for Meteorology 2022

ISSN 1614-1199

Zoé Rehder

Measuring and modeling of methane emissions from ponds in high latitudes

dedicated to
Andrea, Uli, and Mark
for teaching me how to explore

This document was typeset using `classicthesis` developed by André Miede and Ivo Pletikosić available at https://bitbucket.org/amiede/classicthesis/.

ABSTRACT

The Arctic is warming faster than the rest of the Earth, leading to changes in all components of arctic landscapes. Water bodies are one such component, and arctic landscapes abound in water bodies. Among them, ponds are the most numerous water-body type and are especially sensitive to warming. The future of ponds impacts the landscape carbon balance because ponds, like lakes, are carbon sources in a landscape that has acted as a carbon sink for millennia. Notably, water bodies emit methane, with ponds emitting more methane per unit area than larger lakes. However, our understanding of the landscape-scale impact of ponds under current and future climate is lacking. In this dissertation, I identify drivers of spatial variability in pond methane concentrations and estimate the landscape impact of ponds under the current climate and different warming scenarios. I study ponds in the polygonal tundra of the Lena River Delta in Northeast Siberia, which is characterized by a high density of ponds.

I show that geomorphology is one of the most important drivers of methane concentrations. The three distinct pond types of the polygonal tundra (ice-wedge, polygonal-center, and merged polygonal ponds) each have different secondary drivers. These drivers, such as bottom temperature and water depth, directly connect with the geomorphology of the pond types. Water depth is an important driver as it limits the overgrown fraction of the pond. The more of the pond is overgrown, the better is the substrate quality and the higher are the methane concentrations.

Comparing eddy covariance measurements from the tundra and a merged polygonal pond reveals that the pond is a carbon source. In contrast, the tundra is a carbon dioxide sink during the growing season. I show that the landscape uptake of carbon dioxide is overestimated by 11% when neglecting ponds. Methane is highly variable, and one of the measured shores emits significantly more methane than the other landcover types, likely due to seep ebullition. However, methane emissions from open water and from the tundra are of comparable magnitude. Thus, the main landscape-scale impact of pond methane is caused by one local hot spot of emissions.

I estimate an increase in pond methane emissions of 1.08 g CH_4 $year^{-1}$ $°C^{-1}$ per square meter of pond area by employing the novel model MeEP (Methane Emissions from Ponds). This rate translates into an increase of emissions by 180 % if mean annual temperatures rise by 5 °C from present values. Using a historical simulation and simulations with 2.5 °C, 5.0 °C, and 7.5 °C higher annual mean temperatures, I show that most of this emission increase is induced by higher substrate

availability due to elevated vascular-plant productivity under elevated temperatures.

This thesis highlights the importance of polygonal-tundra ponds as carbon sources on the landscape scale. Methane concentrations differ between pond types, and emissions can vary strongly within one pond, especially between the overgrown and open-water areas of a pond. Vascular plants strengthen methanogenesis by improving substrate quality and increasingly do so under warming. Thus, the overgrown fraction of ponds might be an effective proxy for large-scale pond methane emissions, and I demonstrate that plant-mediated fluxes contribute most to the pond emissions on the landscape scale.

ZUSAMMENFASSUNG

Die Arktis erwärmt sich schneller als der Rest der Erde, was zu Veränderungen in allen Komponenten arktischer Landschaften führt. Binnengewässer sind eine solche Komponente, und arktische Landschaften sind reich an Binnengewässern. Unter ihnen sind Tümpel der zahlenmäßig häufigste Gewässertyp und einer, der besonders empfindlich auf die Erwärmung reagiert. Die Zukunft der Tümpel hat Auswirkungen auf die Kohlenstoffbilanz der Landschaft, denn Tümpel wie Seen sind Kohlenstoffquellen in einer Landschaft, die seit Jahrtausenden eine Kohlenstoffsenke ist.

Alle Binnengewässer emittieren Methan, aber Tümpel emittieren mehr Methan pro Flächeneinheit als die größeren Seen. Wir wissen jedoch nicht, wie sich die Methanemissionen von Tümpeln unter jetzigen und zukünftigen klimatischen Bedingungen auf die Kohlenstoffbilanz der Landschaft auswirken. In dieser Dissertation identifiziere ich die Faktoren, die für die räumliche Variabilität von Methankonzentrationen in Tümpeln verantwortlich sind, und ich schätze den Einfluss von Tümpeln auf die Kohlenstoffbilanz der Landschaft unter dem jetzigen Klima und in verschiedenen Erwärmungsszenarien ab. Ich untersuche Tümpel in der polygonalen Tundra des Lena-Flussdeltas in Nordostsibirien. Die polygonale Tundra zeichnet sich durch eine hohe Dichte an Tümpeln aus.

Ich zeige, dass die Geomorphologie einer der wichtigsten Treiber der Methankonzentration in Tümpeln ist. Die drei verschiedenen Tümpeltypen der polygonalen Tundra (Eiskeiltümpel, polygonmittige Tümpel und verbundene polygonale Tümpel) haben jeweils unterschiedliche sekundäre Treiber. Diese Treiber, wie die Bodentemperatur oder die Wassertiefe, stehen in direktem Zusammenhang mit der Geomorphologie der Tümpeltypen. Die Wassertiefe ist ein wichtiger Faktor, da sie den bewachsenen Anteil des Tümpels begrenzt. Je mehr Fläche des Tümpels bewachsen ist, desto besser ist die Substratqualität und desto höher sind die Methankonzentrationen.

Der Vergleich von Eddy-Kovarianz-Messungen der Tundra und eines verbundenen polygonalen Tümpels zeigt, dass der Tümpel eine Kohlenstoffquelle ist. Im Gegensatz dazu ist die Tundra während der Wachstumsperiode eine Kohlenstoffdioxidsenke. Ich zeige, dass die Aufnahme von Kohlenstoffdioxid durch die Landschaft um 11% überschätzt wird, wenn Tümpel vernachlässigt werden. Methanemissionen sind sehr variabel, und eines der gemessenen Ufer emittiert deutlich mehr Methan als die anderen Landschaftstypen, was wahrscheinlich auf einen kontinuierlichen Austritt von Methanblasen zurückzuführen ist. Die Methanemissionen aus offenen Gewässern und aus der Tundra sind ähnlich hoch im Gegensatz zu den Uferemissionen. Methan aus

Tümpeln wirkt sich also hauptsächlich durch lokale Emissionshotspots auf die Kohlenstoffbilanz der Landschaft aus.

Ich berechne einen Anstieg der Tümpelmethanemissionen um 1.08 g CH_4 Jahr^{-1} °C^{-1} pro Quadratmeter Tümpelfläche mit dem neuen Modell MeEP (Methanemissionen aus Tümpeln). Diese Rate entspricht einem Anstieg der Emissionen um 180 %, wenn die mittleren Jahrestemperaturen gegenüber den heutigen Werten um 5 °C steigen. Anhand einer historischen Simulation und von Simulationen mit 2.5 °C, 5.0 °C, und 7.5 °C höheren Jahresmitteltemperaturen zeige ich, dass eine höhere Substratverfügbarkeit aufgrund angestiegener Produktivität von Gefäßpflanzen bei höheren Temperaturen den größten Teil dieses Emissionsanstiegs verursacht.

Diese Arbeit unterstreicht die Bedeutung von Tümpeln in der polygonalen Tundra als Kohlenstoffquellen auf der Landschaftsebene. Die Methankonzentrationen unterscheiden sich je nach Tümpeltyp, und die Emissionen können innerhalb eines Tümpels stark variieren, insbesondere zwischen den bewachsenen und den offenen Wasserbereichen eines Tümpels. Gefäßpflanzen verstärken die Methanogenese, indem sie die Substratqualität verbessern, und tun dies zunehmend bei Erwärmung. Daher könnte der bewachsene Anteil von Tümpeln ein effektiver Indikator für Methanemissionen aus Tümpeln auf größeren räumlichen Skalen sein. Ich zeige, dass pflanzenvermittelte Flüsse den größten Anteil an Tümpelemissionen auf der Landschaftsebene haben.

ACKNOWLEDGMENTS

The content of a Ph.D. project often is not what you thought it would be at the beginning of the project, and this dissertation also evolved with time. Thank you, Victor, for supporting me throughout this evolution, even though there is probably a bigger focus on measurements than you envisioned at the start. Thank you for giving me the opportunity to do fieldwork at all, for trusting me, and for giving me the freedom to develop MeEP how I saw fit. Thomas, without your help, I would have struggled a lot more with MeEP than I did. Thank you for your calm and pragmatic advice. Thank you both for gently steering me back on track when I got lost in some details. Thank you, Lars, for developing the idea of this thesis with me, enabling me to do fieldwork on Samoylov, and your enthusiasm about this project, which always made me more enthusiastic. Martin, you were an excellent panel chair (of course); thank you for providing a safe space for me and my project to thrive.

MeEP would not have been what it is without Victor Stepanenko, who provided the basis for the methane dynamics in the open-water season and discussed the approach to model the ice-covered season with me. Thanks to Moritz, the ponds are safely embedded in mostly frozen soil. I am grateful for the time you took to explain the soil model to me and to help me implement it in MeEP.

The expedition to Samoylov Island was an adventure. Without all the support from Norman, it would have been a chaotic one. Thanks, Norman, for all the troubleshooting and for being there while not being there. Thank you, Anna, for walking all over Samoylov Island and tenaciously sampling the ponds with me (or without me). I also want to thank Andrei Astapov and Waldemar, without whose help I do not think I could have put up the Eddy tower, and Andrei Kartoziia and his students for helping Anna and me and safely bringing us to Kurungakh Island and back. The expedition was an intense experience for me, but it was also a lot of fun, and for that, I want to thank everyone who was at the station with me. Thank you, David Nielsen and Lutz, for babysitting the eddy tower for me. Lutz, I am very happy we wrote a paper together. Working with you was and is very motivating. It taught me a lot. Thank you, David Holl, for all the feedback on both my measurement papers. Thank you, Lotta, for the GIS support.

Thank you, Clara, David Nielsen, and Thomas, for improving the essay so much. And of course, a big thanks to the IMPRS office, Antje, Michaela, and Connie. It is such great relief to know you are there.

You are so on top of the organizational side of the Ph.D. that the bureaucracy was always a breeze.

Doing a Ph.D. is not only about the work, and I am very happy that I got to share an office with Istvan, Sabine, and Alex, who was there for me in the beginning and eased me into life on the 17th floor. In that sense, also thank you to the Land Department and especially all the Land PhDs. Meike, Nora, Guilherme, Mateo, and Josie, thank you for making the office such a pleasant place. Being part of the IMPRS was a great experience for me. Having such a large and kind peer group was very reassuring. Thank you, Arjun, David, Markus, Geet, for being there. Thank you all my friends in Hamburg and elsewhere, for bearing with me. Finally, thank you and sorry for the one person I probably forgot to mention.

Last but not least, I do not think I would be where I am now without my parents and Simon. Thank you for being my haven and backing me up, especially during the last few months. Pinhsin, I do not think you know how much your friendship supported me all this time, and I am deeply grateful to you for making the last years so much happier.

PUBLICATIONS RELATED TO THIS DISSERTATION
Teilveröffentlichungen dieser Dissertation

APPENDIX A:

Rehder Z., Zaplavnova A. and Kutzbach L. (2021). "Identifying Drivers Behind Spatial Variability of Methane Concentrations in East Siberian Ponds." In: *Front. Earth Sci.* 9:617662. DOI: 10.3389/feart.2021.617662

APPENDIX B:

Beckebanze, L.*, **Rehder, Z.***, Holl, D., Wille, C., Mirbach, C., and Kutzbach, L. "Ignoring carbon emissions from thermokarst ponds results in overestimation of tundra net carbon uptake". In: *Biogeosciences* [accepted 29.01.2022]

* These authors contributed equally to this work.

APPENDIX C:

Rehder, Z., Kleinen, T., Kutzbach, L., Stepanenko, V., Langer, M., and Brovkin, V. (2022). "New model for Methane Emissions from Ponds (MeEP) indicates high sensitivity of Arctic ponds to warming". Manuscript in preparation.

CONTENTS

LIST OF FIGURES

UNIFYING ESSAY

1 INTRODUCTION

Pond
noun, countable
an area of water smaller than a lake, often artificially made
— Cambridge Dictionary[1]

1.1 WHAT IS A POND?

Is area enough to define ponds?

What is a pond? The answer to this question seems to be very straightforward. We can probably immediately agree that a pond is like a lake, just smaller. Correspondingly, many studies use size limits to differentiate ponds from lakes (Labrecque et al., 2009; Muster et al., 2017, among others). Yet, the maximum pond sizes differ by orders of magnitude between studies, ranging from 500 m^2 (Polishchuk et al., 2018) to $8 \cdot 10^4$ m^2 (Ramsar Convention Secretariat, 2016). However, the areal extent is not the only property of a pond.

Can ponds sustain fish?

A very descriptive definition of ponds is imposing that ponds are water bodies too shallow to sustain fish (Rautio et al., 2011). The sizes and shapes of water bodies fulfilling this requirement depend on local climatic conditions, which brings us to our study region.

Arctic ponds freeze through in winter.

We concentrate on an arctic permafrost landscape in this work. Ponds are the most common water-body type in the Arctic in terms of numbers (Downing et al., 2006; Polishchuk et al., 2018; Muster et al., 2019). In arctic lowlands, as much as 17 % of the landscape is covered by water bodies (Muster et al., 2017), and ponds cover roughly the same area as lakes in our study area (Muster et al., 2012; Beckebanze et al., 2021a). Shallow water bodies regularly freeze completely in winter in high latitudes. Maximum ice thickness reaches values between two (Arp et al., 2012; Surdu et al., 2014) and five meters (Pienitz et al., 2008). Hence, a water depth of two meters is another possible threshold to differentiate between (arctic) ponds and lakes (Lim et al., 2001). Then, per definition, ponds regularly freeze to the bottom in winter. A complete freeze through has not only implications for fish, but also for the sediment. Water bodies that retain an unfrozen layer of water throughout the year also preserve a layer of unfrozen sediment (talik). These layers can be more than 50 m deep (Ling and Zhang, 2003) and sustain biological productivity throughout the year. Consequently, arctic water bodies' physical, chemical, and biological properties differ substantially depending on their depths.

1 https://dictionary.cambridge.org/dictionary/english/pond, last accessed: 23.12.2021

We define ponds using area and depth.

To account for the freeze through, I define ponds based on both area and depths. In our study region, water bodies can have a large area but still be very shallow, so I choose a generous threshold for pond area of $8 \cdot 10^4$ m^2 (Ramsar Convention Secretariat, 2016). At the same time, I demand that the average pond depth does not exceed two meters and thereby exclude water bodies with talik formation.

1.2 WHY ARE PONDS RELEVANT?

Ponds are better mixed than lakes.

Let us explore another consequence of the differing depths of lakes and ponds. Ponds and lakes are mostly heated from the top, leading to stratification, especially during summer (Boehrer and Schultze, 2008; Kraemer et al., 2015). Wind shear and cooling of water enhance the mixing of water bodies (Pernica et al., 2014) partly reversing the stratification. The resulting typical thermal profile of lakes in summer is usually divided into two parts: The upper part of the lake, the epilimnion, is continuously mixed and shows, if any, only very weak temperature gradients. The lower part, the hypolimnion, is stably stratified, so the oxygen supply is limited. The frequency of a complete mixing, often called *turnover*, depends on climatic conditions and water depths. Some water bodies turn over daily, some once or twice a year, or only once every few years. Some always stay at least partly stratified (Lewis, 1983). The frequency of the turnover has strong implications for the biological processes in the lake, flushing out accumulated dissolved substances and gases, such as methane (Vachon et al., 2019), and raising oxygen concentrations (Lehmann et al., 2015). The shallow depth of ponds enhances mixing, especially convective mixing (Read et al., 2012), and thus expedites diffusive fluxes from the sediment to the atmosphere.

What is the large-scale impact of ponds?

One gas transported from the bottom of water bodies to the atmosphere is methane. On a pan-Arctic scale, estimates of water-body methane emissions range from 13.8 Tg CH_4 yr^{-1} to 17.7 Tg CH_4 yr^{-1} (Tan and Zhuang, 2015; Wik et al., 2016; Matthews et al., 2020). That is about 5 % of the annual antropogenic methane emissions in the years 2000 – 2017 (272 – 394 Tg CH_4 yr^{-1}, Saunois et al., 2020). The water-body methane estimates include both lakes and ponds. Holgerson and Raymond (2016) estimated that globally ponds contribute over 40 % of total diffusive water-body methane emissions. Methane emissions tend to be higher the smaller the water body (Bastviken et al., 2004; Juutinen et al., 2009; Downing, 2010; Kuhn et al., 2021) partly due to more efficient mixing in shallow water bodies (Holgerson and Raymond, 2016). Thus, per unit area, ponds are more potent emitters than lakes.

Where does methanogenesis occur?

The high methane emissions from ponds can also be due to higher rates of methanogenesis[2]. Methane is mostly produced in anoxic

2 microbial production of methane

bottom waters and in the top sediment of lakes and ponds during the decomposition of organic material (Conrad, 1999; Hedderich and Whitman, 2006; Borrel et al., 2011). It is still debated whether methane is additionally produced in the oxic part of the water column (Bogard et al., 2014; Donis et al., 2017; Peeters et al., 2019) or if much of the methane in the epilimnion is produced in the sediments of the littoral[3] zone (Encinas Fernández et al., 2016). However, oxic production is, should it exist, more important in large water bodies than in ponds (Günthel et al., 2020). Since I focus on ponds, I concentrate on benthic[4] methanogenesis.

Methane is emitted through different processes.

Methane produced in the sediment escapes to the atmosphere through one of three mechanisms during the open-water season, first, by the diffusion mentioned above, second, through gas-filled pore spaces in plants (plant-mediated transport), or, third, by bubbling up (ebullition) (Bastviken et al., 2004; Knoblauch et al., 2015, among others). Lastly, methane accumulates under the ice in winter and is abruptly released when the ice opens up in the spring. Estimates of the contribution of this spring flush to the annual water-body methane emissions range from 15 % to more than 50 % (Wik et al., 2016; Matthews et al., 2020; Prėskienis et al., 2021). Ebullition transports three to four times more methane from arctic water bodies to the atmosphere than diffusion (Wik et al., 2016; Prėskienis et al., 2021) during the open-water season. Hardly any study estimates the water-body scale contribution of plant-mediated transport. Juutinen et al. (2003) assessed that emissions from the littoral, overgrown zone of boreal lakes are responsible for 66 – 77 % of total emissions while only making up 8 – 25 % of the lake area. Andresen et al. (2016) focused on an arctic landscape and found that plant-mediated fluxes contribute up to two-thirds of the overall tundra methane emissions even though these fluxes originate in as little as five percent of the area. Thus, ponds are a highly relevant landscape component in the carbon balance. However, since individual ponds are small, they often get neglected in landscape carbon budgets.

1.3 KNOWN METHANE VARIABILITY IN PONDS

Temporal variability of methane emissions

Methane emissions are difficult to upscale because of a high spatial and temporal variability. I already introduced the spring flush, which leads to a pronounced seasonal signal. On the daily scale, fluxes are driven by dynamics in the epilimnion depth (Laurion et al., 2009).

Controls on methane dynamics

Another control on methane concentrations and diffusive emissions is oxygen availability, which fuels methane oxidation in the water column (Osudar et al., 2016; Martinez-Cruz et al., 2015). The rate of methanogenesis, which is another strong control of methane dynamics,

3 near the shore
4 at the bottom of the pond

depends on substrate and nutrient availability (Juutinen et al., 2009; Jong et al., 2018). Temperature impacts methanogenesis, methanotrophy[5], and diffusive processes and is thus another important driver of methane dynamics (Yvon-Durocher et al., 2014).

Pond methane emissions have different drivers in different regions.

On the spatial scale, location and local climate strongly impact methane emissions (Sepulveda-Jauregui et al., 2015; Sabrekov et al., 2017). Regional differences explain part of the large spatial variability of methane concentrations in those studies which aggregate pond concentrations over large areas, for example the West Siberian Lowlands (Polishchuk et al., 2018) or Finland (Juutinen et al., 2009). These two studies report an overarching dependence of methane concentrations and emissions on water-body size despite covering different regions. This dependence, however, has not been observed by Zabelina et al. (2020) underlining the need for further studies on spatial variability. To summarize, methane emissions depend on various environmental, meteorological, and climatic variables and differ substantially between regions.

1.4 WHAT IS THE POLYGONAL TUNDRA?

Polygonal tundra forms through freeze and thaw processes.

The ice-wedge polygonal tundra is a landscape type that typically features a high pond density. It thus offers itself for studies of spatial methane variability in ponds (Fig. 1.1(a)). This landscape type with the characteristic patterned ground is common where the arctic topography is flat and annual mean air temperatures are below $-6\,^{\circ}\mathrm{C}$ (Jorgenson et al., 2015). Polygonal tundra covers roughly 3 % of the landmasses in the Arctic (Minke et al., 2007). It forms because temperatures drop far below freezing in winter; consequently, the soil contracts and tension cracks open up. These cracks fill with meltwater in the spring before the soil can expand again. If this process repeatedly occurs, ice wedges eventually form just below the active layer (Jorgenson et al., 2015). The cracks often occur in shapes that resemble polygons (Cresto Aleina et al., 2013) and the formation of the ice wedges leads to movement of material from the center of the polygon to the edges resulting in dry rims on top of the ice wedges and moist centers in the middle of the polygons (Minayeva et al., 2016).

1.4.1 *PONDS IN THE POLYGONAL TUNDRA*

There are three ponds types in the polygonal tundra.

The frozen soil strongly diminishes sub-surface runoff, and local melting can lead to ground subsidence. If the soil subsides sufficiently, the water table rises above the ground. Depending on where the ground subsides, one of three distinct pond types establishes (Fig. 1.2). If the middle part of a polygon subsides, in between the ice wedges, a nearly circular pond develops with a flat bottom. We call these ponds

5 microbial consumption of methane

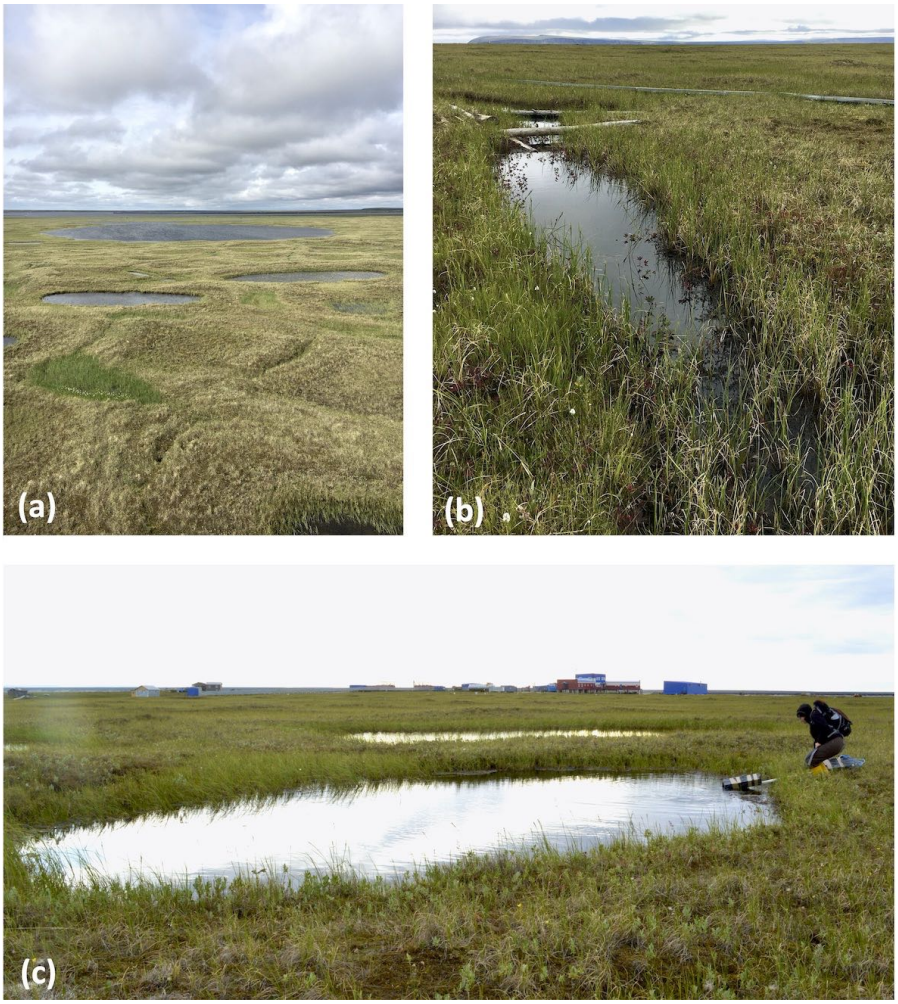

Figure 1.1: Each panel shows different ponds on Samoylov Island. In addition, patterned ground is visible in the foreground of (a). The cracks reveal the location of ice wedges. In the background, we see two polygonal-center ponds with intact rims. The ice-wedge pond in (b) has the typical elongated shape, while the polygonal-center pond in (c) is more circular. In (c), we also see the author of this work for scale and the research station of Samoylov Island in the background. All photos were taken on Samoylov Island in July or August of 2019. The photos (a) and (b) were taken by the author, and (c) by Anna Zaplavnova during joint fieldwork.

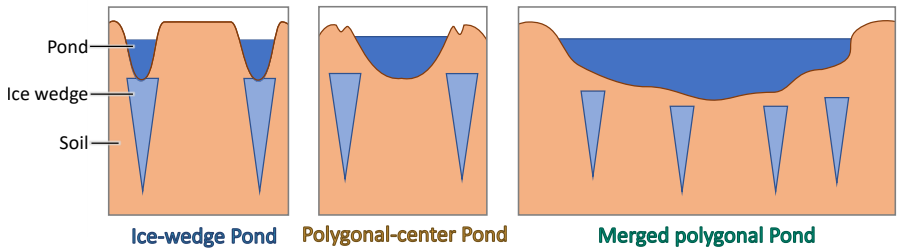

Figure 1.2: Schematic of the different pond types in the polygonal tundra. Ice-wedge ponds form along the edges of polygons on top of ice wedges, have a frozen bottom, and often have an elongated shape and a steep slope. Polygonal-center ponds form in between ice wedges, in the center of the polygons. They tend to be nearly circular. If several polygons subside, merged polygonal ponds form. These ponds are the largest pond type of the three.

polygonal-center ponds (Fig. 1.1(a) & (c)). If the ice wedge itself degrades, a water-filled trough forms on top. These ponds are often elongated, and the remainder of the ice wedge constitutes part of the pond bottom leading to cold bottom temperatures. These ponds are labelled *ice-wedge ponds* (Fig 1.1(b)). Finally, sometimes several polygons subside, leading to comparably large submerged areas, though the polygonal structure is often visible at the pond edge and bottom. We label these ponds *merged polygonal ponds*.

Methane variability in polygonal-tundra ponds

The specific geomorphology of each pond type also has a large impact on the spatial variability of pond methane dynamics (Negandhi et al., 2013; Bouchard et al., 2015; Prėskienis et al., 2021). However, polygonal-tundra ponds have been studied more extensively on the North American continent than in Eurasia, where our study site lies.

1.5 THE LENA RIVER DELTA AND SAMOYLOV ISLAND

The Lena River Delta features many ponds.

I study the three pond types in the Lena River Delta in Northeast Siberia (Fig. 1.3 (a) & (b)). With an annual mean temperature of less than $-12\,°C$, the temperature condition for ice-wedge formation is more than met in this area of continuous permafrost. The sediments in the delta accumulated over the last ten thousands of years, and the delta can be divided into three terraces[6] depending on the age, origin and composition of the sediment (Fig. 1.3(b), Schwamborn et al., 2002). The polygonal structures are most pronounced on the delta's first, youngest river terrace. This terrace formed during the Holocene due to fluvial[7] deposition (Schwamborn et al., 2002; Schneider et al., 2009;

6 A river terrace is a flat area that used to be on the same level as the river but now has a higher elevation than the river. Many floodplains eventually turn into river terraces when they are not regularly flooded anymore.

7 by the river

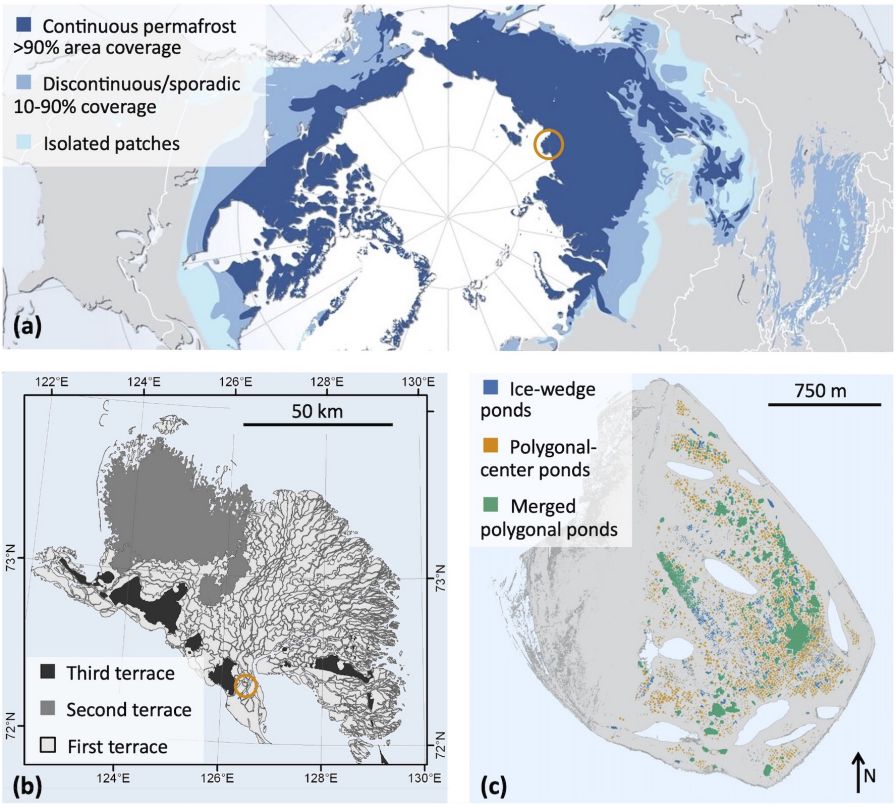

Figure 1.3: Overview of my study area. The map in (a) illustrates the distribution of pan-Arctic permafrost adapted from Ahlenius (2016). The Lena River Delta, situated within the continuous permafrost zone, is marked by a circle. In panel (b) we see a close-up of Lena River Delta adapted from Schneider et al. (2009). The three river terraces of the delta are depicted in gray shades. A circle marks the location of Samoylov Island. The map of Samoylov Island in (c) includes a classification of all ponds on the river terrace (eastern part of the island) based on the landcover classification in appendix B.

Muster et al., 2012) and among the three terraces of the Lena River Delta, the first is the wettest and contains most of the small water bodies. The second terrace features the least ponds and is thus not of interest for this work. The third terrace is the oldest, its origin dating back to the Pleistocene, and comprises sandy deposits overlain by an ice complex. Much of the ice complex is in turn overlain by Holocene deposits (Schwamborn et al., 2002; Wetterich et al., 2008). Part of the third terrace also exhibits weak polygonal structures and, in some parts, a high pond density, though less so than the first terrace. Besides the three terraces, the delta includes floodplains regularly overflown by the river.

Samoylov Island is divided into a river terrace and a floodplain.

Samoylov Island, my study site, is split into two parts: The smaller western part is a floodplain covering about 2 km^2. In contrast, the eastern part (about 3 km^2) belongs to the first river terrace with a

partly degraded polygonal tundra and numerous ponds (Fig. 1.3 (c)). The island lies in the southern part of the delta at 72 ° 22′ N and 126 ° 30′ E (Fig. 1.3 (b)) and hosts a research station. This work follows in the footsteps of more than twenty years of research on Samoylov Island, which is subject to long-term observations of the permafrost, meteorological conditions (Boike et al., 2019), and greenhouse-gas fluxes, like carbon dioxide (Holl et al., 2019b).

1.6 OPEN QUESTIONS ON PONDS AND METHANE

This thesis explores methane dynamics in ponds of the Lena River Delta from various angles. First, I focus on the dissolved methane concentration in the surface waters of ponds since the variability of methane emissions and concentrations is larger in ponds than in lakes (Juutinen et al., 2009; Laurion et al., 2009; Sepulveda-Jauregui et al., 2015; Holgerson and Raymond, 2016). The causes of this high variability are not fully constrained, leading to our first research question:

1st research question

WHAT DRIVES THE SPATIAL VARIABILITY OF METHANE CONCENTRATION IN POLYGONAL-TUNDRA PONDS?

I investigate the role of the ponds as a landscape source of carbon. As mentioned above, only a few studies directly compare carbon fluxes from ponds with carbon fluxes from the surrounding landscape. Jammet et al. (2017) found that lakes act as carbon sources within a subarctic fen, which is otherwise a carbon sink. Comparable measurement studies do not exist for tundra landscapes, which, as we have seen, tend to be rich in ponds. Thus, our second research question is:

2nd research question

WHAT IS THE IMPACT OF POLYGONAL-TUNDRA PONDS ON THE LANDSCAPE CARBON BUDGET?

Lastly, climate change is hard to ignore when researching the Arctic since high latitudes are warming at an above-average rate (Chapman and Walsh, 1993; Bekryaev et al., 2010; Serreze and Barry, 2011). Warmer temperatures alter many components of the local system, which in turn modify methane emissions. For example, vegetation may green or brown (Villarreal et al., 2012; Winkler et al., 2021) leading to lower of higher methane emissions. Ponds may form or vanish due to hydrological changes (Christensen et al., 2004; Bring et al., 2016). Higher temperatures and longer open-water seasons are expected to raise pond methane emissions (Zhu et al., 2020). To sum up, many of the individual drivers of changes in methane emissions under warming are known. However, the combined effect of these direct and mediated impacts on methane emissions from ponds are under-explored. So, I ask:

HOW DO METHANE EMISSIONS FROM POLYGONAL-TUNDRA PONDS CHANGE UNDER WARMING?

3rd research question

While I address the first two questions using measurements, I exploit simulations from a dedicated pond model for the last research question.

2 DRIVERS OF SPATIAL VARIABILITY

2.1 CONNECTING METHANE CONCENTRATIONS AND EMISSIONS

Methane emissions are more complex to measure than methane concentrations.

Ponds emit methane, and emissions are fluxes; they have a spatial and temporal dependency, making them a bit more of a headache to measure than state variables, such as, for example, air temperature. There is a range of techniques to measure greenhouse-gas fluxes, and I will explore one sophisticated, though stationary, method in the next chapter. Firstly, however, we are more interested in spatial than temporal variability. To assess spatial variability, we need to measure various ponds in a short amount of time to minimize the impact of seasonal variability. The most reasonable approach is to measure methane concentrations instead of emissions. The diffusive fluxes and the methane concentrations in the surface water of a pond are tightly connected. The diffusive flux across the water-air interface F_{diff} (e.g. mol m^{-2} s^{-1}) is commonly expressed based on Fick's law of diffusion (Fick, 1855) via

$$F_{diff} = k(C_{aq} - C_{eq}). \tag{2.1}$$

This equation is commonly called the turbulent boundary layer equation (TBL equation). C_{eq} (e.g. mol m^{-3}) is the methane concentration if the water body were in equilibrium with atmospheric methane concentrations. The equilibrium depends on the solubility of a specific gas and on temperature (Sander, 2015). C_{aq} (e.g. mol m^{-3}) is the actual (measured) water methane concentration. Finally, k (e.g. m s^{-1}), the diffusion coefficient or piston velocity, summarizes all the difficult physics of diffusion in a rate parameter. While determining the concentrations is straight-forward, estimating k ideally encompasses time-intensive water-body specific measurements (Cole and Caraco, 1998; Wanninkhof, 1992; Matthews et al., 2003). Alternatively, we could deploy a parameterization. However, a simple, wind-based parameterization introduces considerable uncertainty, especially for small water bodies and low wind speeds (Cole et al., 2010; MacIntyre et al., 2010). Since I focus on small water bodies, a reasonable parameterization of k requires information on convective turbulence (MacIntyre et al., 2010; Read et al., 2012; Heiskanen et al., 2014). We need information on heat fluxes, which are again less straightforward to measure than methane concentrations.

Methane concentrations can be used as a proxy for diffusive fluxes.

In this study of spatial variability, I opted for investigating methane concentrations directly rather than translating them into emissions to avoid the uncertainty introduced by parameterizing k. However,

to account for the processes relevant for connecting emissions and concentrations, I measure variables that act as proxies for the mixing strength, such as the wind speed and pond bottom temperatures compared to surface-layer temperatures. To summarize, I investigate the spatial variability of methane concentration as a proxy for spatial variability of diffusive methane emissions. We note that methane concentrations can only give limited insight into the magnitude of ebullition or plant-mediated fluxes. However, I expect general trends of higher and lower emissions in specific ponds to be consistent over methane emission pathways. The complete study is available in appendix A.

2.2 MEASUREMENTS

We measured methane concentrations in 41 ponds in the Lena River Delta.

To grasp the spatial variability of methane concentrations in Lena River Delta ponds, I sampled 41 ponds in the summer of 2019 with assistance from Anna Zaplavnova, a Master's student at the University of Novosibirsk. The sampled ponds are divided nearly equally among the pond types; we sampled 15 polygonal-center ponds, 13 ice-wedge ponds, and 14 merged polygonal ponds. Most of these ponds are on Samoylov Island, but eleven were sampled on the southern tip of Kurungakh island, where the first and the third terrace are close to each other. We included six ponds from the third terrace and five ponds from the first terrace on Kurungakh island (Fig. A.2). We measured on 22 days between mid-July and the end of August. This period falls well within the growing season, which usually lasts from mid-June to mid-September (Kutzbach et al., 2007). Measurements were always taken at a similar time (mid-day to afternoon). Each time we examined a pond, we took water samples at several points in the pond, both from the surface water and from the water column, to determine the methane concentration (section A.2.2). In addition, we measured the dissolved oxygen concentration, the water temperature (both near the surface and at the bottom of the pond), the thaw depths under the pond, the water depths, and the organic content of the pond sediment near the shore. We combined this data with stationary meteorological measurements of incoming short-wave radiation and wind speed (section A.2.3). Last but not least, we used information on the pond area, as well as the fraction of each pond covered by moss and vascular plants[1] (section A.2.4) using an orthophoto map of both islands, which was taken in 2016 (Kartoziia, 2019).

2.3 EACH POND TYPE HAS UNIQUE DRIVERS

All pond types are supersaturated in methane.

I find that all pond types are super saturated in methane with highest

1 All plants which have tissues transporting water, nutrients and minerals are vascular plants.

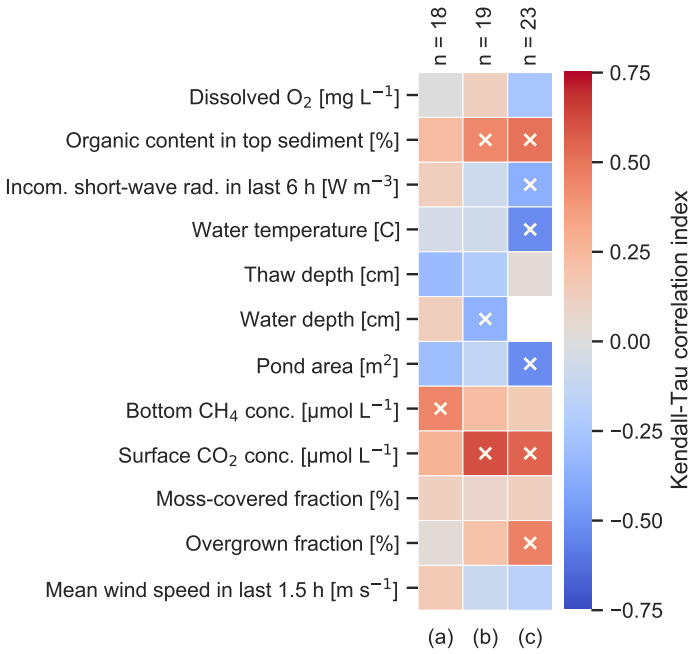

Figure 2.1: Kendall-Tau correlation index of different variables with surface methane concentrations in (a) ice-wedge ponds, (b) polygonal-center ponds, (c) merged polygonal ponds. Significant correlations ($p < 0.05$) are marked by a white cross. Number of measurements per pond type (n) is indicated at the top of each column. The white tile is due to missing data.

median concentrations of 2.4 µmol L^{-1} (25 - 75th percentile: 0.9-7.1 µmol L^{-1}) in ice-wedge ponds. Polygonal-center ponds have concentrations of 0.6 µmol L^{-1} (25 - 75th percentile: 0.4-1.5 µmol L^{-1}) which are comparable to the concentrations in merged polygonal ponds of 0.7 µmol L^{-1} (25 - 75th percentile: 0.5-1.2 µmol L^{-1}). Polygonal-center ponds have a slightly higher variability. While two of the pond types have similar concentrations, I find that each pond type has a distinct set of controls on surface-water methane concentrations.

Each pond type has a different set of dominant drivers.

To get a first idea of the drivers, I correlate all additional variables we collected with the surface-water methane concentrations. I use the Kendall-Tau correlation, which does not assume a linear relationship between the two considered variables (Knight, 1966, or section A.2.5). I find that each pond type correlates significantly with a different set of variables and that the main processes governing surface methane concentrations are unique between pond types.

2.3.1 *ICE-WEDGE PONDS*

Ice-wedge ponds are often stratified.

Surface methane concentrations in ice-wedge ponds only significantly correlate with bottom methane concentrations; this correlation is es-

pecially strong for higher wind speeds (Kendall-tau correlation between bottom and surface methane concentrations for all wind speeds: $p < 0.05$, for wind > 4 m s^{-1} : $p < 0.01$). At lower wind speeds, the surface methane concentrations are also lower. This pattern is due to stratification: Ice-wedge ponds have lower bottom temperatures than the other two pond types (5.9(2.5) °C versus 9.5(2.2) °C (mean with standard deviation)). This lower temperature leads to a more stable stratification in ice-wedge ponds than in other pond types (Prėskienis et al., 2021). When the wind is strong enough, methane accumulated in the hypolimnion is mixed towards the pond surface. Thus, both bottom and surface methane concentrations depend strongly on wind speed.

Larger ice-wedge ponds are more degraded.

Apart from the correlation with wind speed, bottom methane concentrations correlate with pond area. In ice-wedge ponds, the pond area plays a special role. When polygonal landscapes degrade, this degradation usually leads to an increased formation of ice-wedge ponds. Thus, leaching of dissolved organic materials is more common in ice-wedge than in other ponds (Negandhi et al., 2014). The larger an ice-wedge pond, the more advanced is the degradation (Liljedahl et al., 2016), and leaching of freshly thawing labile carbon becomes more unlikely again (Koch et al., 2018). In addition, the larger the pond, the more efficient is the wind-based mixing (Bastviken et al., 2004; Read et al., 2012).

Suppose I use a pond area, wind speed, and bottom concentrations in a multiple linear regression to predict surface methane concentrations. In that case, I can explain more than half of the variability of surface methane concentrations (predictive[2] $R^2 = 0.6$).

2.3.2 POLYGONAL-CENTER PONDS

Water depths is an important predictor in polygonal-center ponds.

Instead of area, water depth is a more important predictor in polygonal-center ponds (Fig. 2.1), in line with Juutinen et al. (2009) who also identified water depth as a more important predictor of methane emissions than area. Interestingly, water depth does not strongly correlate with pond area for this pond type ($p = 0.3$). In shallower ponds, methane has to bridge a shorter distance from the sediment to the atmosphere, and the well-mixed epilimnion makes up a larger fraction of the water column.

Methane concentrations in polygonal-center ponds are limited by substrate quality.

In addition to water depth, the amount of organic carbon in the top sediment has a significant correlation with surface methane concentrations; both of these variables have, in turn, a significant correlation with the overgrown fraction of the pond ($p < 0.05$). The shallower the pond, the larger is the fraction of the pond shallow enough for vascular

2 the predictive R^2 measures how well the regression model predicts values which were not used to construct the model. See section A.2.5

plants. Apart from enabling plant-mediated transport, macrophytes[3] improve substrate availability and elevate the organic content in the sediment (Joabsson and Christensen, 2002; Ström et al., 2003) fueling methanogenesis. Using the first principal component of these three variables as input for a linear regression on the surface concentrations yields a predictive R^2 of 0.6.

2.3.3 *MERGED POLYGONAL PONDS*

Methane concentrations in merged polygonal ponds are controlled by stratification

Among the three pond types, merged polygonal ponds correlate significantly with the largest number of environmental variables (Fig. 2.1). The significant variables can be divided into two groups. Incoming short-wave radiation in the last six hours, water (surface) temperature, and pond area (as a proxy for wind fetch and water depths) correlate negatively with surface methane concentrations, similar to results in a study by Burger et al. (2016). The process I consider to be driving this correlation is stratification. Since merged polygonal ponds are deeper than the other pond types, the sunlight warms only the upper layer of the pond and inhibits the mixing of surface and bottom waters. Thus, methane produced in the sediment is trapped in the hypolimnion.

Methane concentrations in merged polygonal ponds are controlled by substrate.

The second group of variables encompasses the organic content in the top sediment, the overgrown fraction, and, as the first group, area. These variables constrain substrate availability for methanogenesis. The fact that they correlate significantly with surface methane concentrations indicates that merged polygonal ponds are driven by substrate quality analogous to polygonal ponds and tundra soils in our study area (Wagner et al., 2003). I combine variables from both groups by using (a) incoming short-wave radiation and dissolved oxygen as proxies for stratification, (b) the overgrown fraction and organic content for substrate quality, and pond area, which is relevant for both processes. These variables' first two principal components result in a predictive R^2 of 0.6 in a multiple linear regression of surface methane concentrations.

2.4 OVERARCHING PATTERNS

Stratification matters in two out of three pond types.

We find that the intensity of mixing impacts surface methane concentrations substantially. While stratification is highly dependent on meteorological conditions, like incoming radiation or wind speed, some ponds promote stratification more than others. We determine that ice-wedge ponds and large merged polygonal ponds are predisposed to stratification (Negandhi et al., 2014; Prėskienis et al., 2021).

Vascular plants regulate substrate quality.

In both polygonal-center and merged polygonal ponds, we observe a dependence of surface methane concentrations on substrate quality (Jong et al., 2018), depicted by the organic content in the top sediment

3 Aquatic plants visible to the naked eye

and the overgrown fraction. We assume that smaller ice-wedge ponds exhibit higher concentrations due to a more pronounced input of allochthonous[4] substrate, another form of substrate dependence. We conclude that substrate quality is closely linked to the abundance of vascular plants in polygonal tundra ponds. The higher the macrophyte cover, the higher is the rate of methanogenesis. This conclusion is supported by previous findings that ponds emit mostly contemporary carbon (Bouchard et al., 2015).

Pond emissions depend on substrate availability.

Though surface methane concentrations only directly relate to diffusive fluxes, substrate limitation impacts all transport mechanisms. Thus, I conclude that the overgrown fraction of ponds is an important driver for the rate of methanogenesis (Joabsson and Christensen, 2002; Kim, 2015). Furthermore, we know that plant-mediated transport is a very efficient pathway for methane (Knoblauch et al., 2015) further elevating the role of vegetation for total pond methane emissions.

Geomorphology governs methane concentrations.

Since water depth limits vegetation cover and the bathymetry of a pond depends on the type, geomorphology is an important driver of surface methane concentrations and emissions (Sepulveda-Jauregui et al., 2015; Juutinen et al., 2009). Further, the pond type affects stratification by controlling water depth, area, and bottom temperature.

Our findings might hold for other polygonal-tundra landscapes.

The geomorphological features of the three pond types are also prevalent in polygonal-tundra landscapes other than the one studied here. Strikingly, the mean surface concentrations we measured are very similar to concentrations in polygonal-tundra ponds sampled in the Canadian Arctic (mean with standard deviation in parenthesis: ice-wedge ponds 4.1(4.7) µmol L-1; polygonal-center ponds 1.3(1.7) µmol L-1; Laurion et al., 2009; Negandhi et al., 2013). Though the results of this study can not be generalized for ponds in all landscapes, the results might apply to other polygonal-tundra ponds.

4 not originating in the pond

3

LANDSCAPE IMPACT OF POLYGONAL-TUNDRA PONDS

What is the landscape impact of ponds?

While I have emphasized the relevance of ponds as methane sources, I have hardly focused on the landscape surrounding the ponds. We have discussed ground heterogeneity and how it governs pond properties so far. Next, we focus on the magnitude of carbon fluxes from ponds and compare them to the carbon balance of the tundra surrounding the ponds to assess the landscape impact of ponds.

3.1 THE CARBON BALANCE OF THE TUNDRA

Arctic soils are a sink of carbon dioxide and a methane source.

What do we know about the carbon balance of the tundra? Circumpolar soils have been a sink of carbon for a long time, storing large amounts of it. Hugelius et al. (2014) estimated that more than 1300 Pg of organic carbon are stored in the three uppermost meters of circumpolar soils, which is about twice the carbon content of the atmosphere. The polygonal tundra on Samoylov Island is still a stable carbon dioxide sink throughout the growing season (Holl et al., 2019b). However, due to the high water saturation in the soils, the polygonal tundra is a net source of methane. Similar to the high spatial variability of methane emissions from ponds, methane emissions from the polygonal tundra as a whole are also highly variable. The geomorphology drives much of this variability. Even when ponds do not form, the typical microtopography of the polygonal tundra modulates the water table, and the water-table height is an important control on tundra methane emissions (Kutzbach et al., 2004; Sachs et al., 2010): The rims of polygons are slightly elevated compared to polygonal centers, which are wetter than the rims and have a higher water-table height. Since methanogenesis requires anoxic conditions, the methane in the centers is produced closer to the top of the soil, and less of it is oxidized on its way to the atmosphere since methanotrophs are more abundant in the rims than in the centers (Liebner and Wagner, 2007). Hence, polygonal centers are stronger emitters of methane than the rims.

Ponds add to the landscape heterogeneity.

Besides polygonal centers and rims, ponds add to the spatial heterogeneity of the landscape. In a region as rich in water bodies as the polygonal tundra of Samoylov Island, the question of the landscape impact of ponds is self-evident.

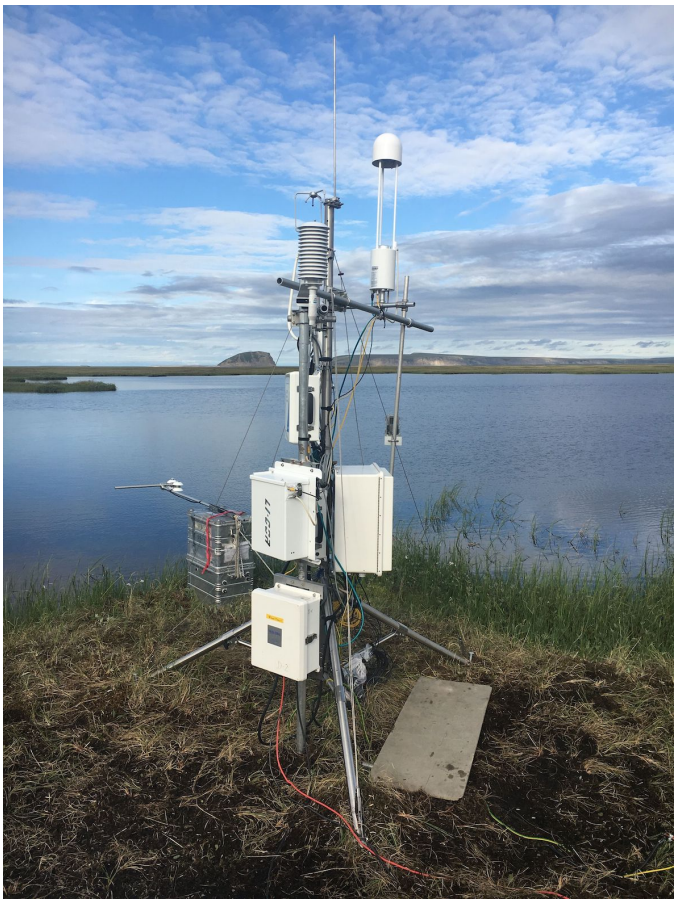

Figure 3.1: Photograph of the eddy covariance tower next to a merged polygonal pond. Since the tower was located at the shore of a large pond, it measured both tundra (westerly wind) and pond (easterly wind). The photo was taken on 11 July 2019 by the author.

3.2 EDDY COVARIANCE MEASUREMENTS

I used eddy covariance measurements.

I mentioned earlier that measuring fluxes is more intricate than measuring state variables. A key component of this chapter is a measurement technique called eddy covariance. I will first give an overview of the associated assumptions, advantages, and limitations before we examine the landscape impact of pond carbon emissions. With eddy covariance measurements, we can observe fluxes at a high temporal resolution, usually half-hourly fluxes, from the area surrounding the tower on which the instruments are mounted. By strategically placing a tower at the shore of a large pond, we can quantify pond and tundra fluxes and compare them. For the full study, which I conducted in close cooperation with Lutz Beckebanze, a Ph.D. candidate at the Universität Hamburg, please refer to appendix B.

3.2.1 *HOW DO EDDY COVARIANCE MEASUREMENTS WORK?*

With eddy covariance, we determine turbulent fluxes.

With eddy covariance, we quantify turbulent fluxes only. Additional transport mechanisms like molecular diffusion or advection are not assessed. However, if turbulence is well developed, the contribution of molecular diffusion and advection to gas and heat fluxes is negligible. We measure air properties at a high frequency and a certain height, usually between 1.5 and 150 m above the ground (Burba, 2013), and calculate the fluxes from those measurements. Air passes by the instruments, and this air consists of little parcels, which we call eddies. The area where the air parcels most likely last made contact with the surface is called the *footprint*. We assess fluxes between this footprint and the atmosphere with the eddy covariance technique. If we quantify all upwards and downwards moving parcels as well as their gas concentrations, we can infer the net gas fluxes (F), such as the methane flux, as

$$F \approx \overline{\rho}\ \overline{w' c'}. \tag{3.1}$$

$\overline{\rho}$ is the mean air density during one flux interval. w stands for the vertical velocity, and c is the gas concentration. Using the apostrophe indicates that we are only considering the deviations of a variable around its mean value of each flux interval. The vertical bar signifies the temporal mean over each flux interval. Thus, it is enough to measure ρ with a low temporal resolution. For w and c, we need high-frequency measurements. Nevertheless, if the average value of one of these two variables is off, we still compute the correct flux. More detail on eddy covariance fluxes can be found in, for example, Burba (2013), and in section B.2.3.

Assumptions needed for eddy covariance measurements

Eq. 3.1 is only valid under three main assumptions:

- Turbulence is well developed and dominates the gas flux.
- The area around the eddy covariance instruments is flat.
- There is no divergence or convergence of air around the instruments.

The advantage of this method is that it does not disturb the surface, in contrast to, for example, chamber measurements. The disadvantage is that we average over the entire footprint, which in our case has a diameter of a few hundred meters, and cannot resolve small-scale point sources.

3.2.2 *EDDY COVARIANCE MEASUREMENTS IN THIS WORK*

How and where did I install the eddy covariance tower?

The instruments to measure ρ, w, and different gas concentrations c are usually attached to a tower. For this work, I set up a tower at the western shore of a large merged polygonal pond on the river terrace

of Samoylov Island. Only large merged polygonal ponds are extensive enough to fit the scale of the eddy covariance measurements. The tower recorded the three-dimensional wind speed and gas fluxes of water, carbon dioxide, and methane at a frequency of 20 Hz (section B.2.2 and Fig. 3.1). The tower operated for about 60 days, from mid-June to mid-September in the summer of 2019. When the wind blew from the west, the tower measured mostly tundra fluxes, including some small polygonal-center ponds. The merged polygonal pond dominated the measured fluxes when the wind blew from the east. Using a land-cover classification, we can determine the relative contribution of different surface classes to the footprint area at each half-hourly flux interval.

3.3 A SHORT EXCURSION ON CARBON DIOXIDE

Including ponds lowers the estimated landscape carbon uptake by 11%.

Since the tundra is a carbon dioxide sink, I first delve into the carbon dioxide dynamics of pond versus tundra. In contrast to methane, the carbon dioxide dynamics of the tundra can be approximated by an empirical model (Runkle et al., 2013). We fit the model to our tundra measurements for moving five-day periods. In this way, the model captures seasonal variability. We can extract the water-body fluxes from the mixed signal measured by the tower by exploiting the modeled fluxes. Applying this model to the total measurement period, we find that on average, the tundra takes up 0.27 ± 0.01 g m^{-2} day^{-1} carbon in the form of carbon dioxide per day. Note that the uncertainty indicates the model error, not the daily variations of the fluxes, which vary from net uptake during the day to a net release of carbon dioxide during the night. The merged polygonal pond is a stable source of carbon dioxide, emitting on average 0.13 g CO_2-C m^{-2} day^{-1}. When weighting the two fluxes with the area they cover on the river terrace of Samoylov Island, the landscape takes up 11% less carbon dioxide than it would without ponds.

3.4 METHANE EMISSIONS FROM TUNDRA AND POND

We study methane emissions based on wind sectors.

Let us come back to the primary trace gas of this study. Methane exhibits more spatial variability than carbon dioxide. Since there is no comparable model to the empirical one we used for carbon dioxide fluxes from the tundra, it is not possible to extract the fluxes from the pond from a mixed signal. We instead investigate methane fluxes based on wind sectors (Fig. 3.2). We divide the landscape into a tundra section, two shore sections, and one section dominated by open water from the merged polygonal pond.

Methane fluxes from pond and tundra are comparable.

The fluxes from the direction of the pond (13.90 $^{18.46}_{11.02}$ mg m^{-2} d^{-1}, $\mathrm{Median}\ ^{75\%\mathrm{Percentile}}_{25\%\mathrm{Percentile}}$) are slightly higher than the fluxes from the tundra (12.55 $^{16.07}_{9.65}$ mg m^{-2} d^{-1}) but the difference is well within statistical uncertainty. This finding agrees with results by Knoblauch

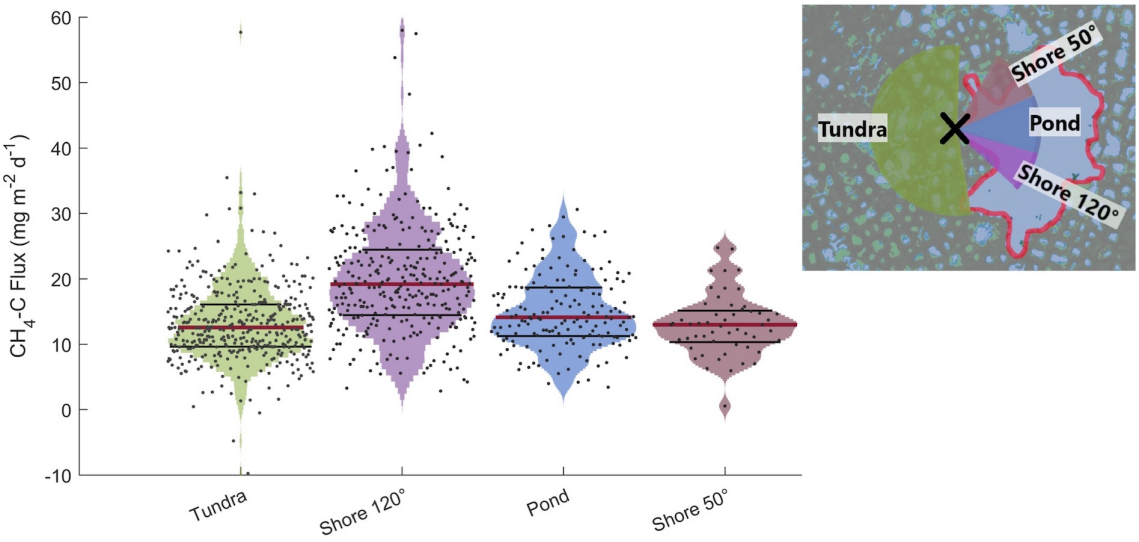

Figure 3.2: Violin plots of observed CH_4 emissions at the EC tower separated into four different wind direction classes. A violin plot shows the distribution of measurements along the y-axis - the width of the curves expresses the density of data points at each y-value. Medians of CH_4 emission distributions are shown as red lines, and 75^{th} & 25^{th} percentile are shown as black lines. On the right, we see the location of the eddy covariance tower within the land-cover classification. Light blue background colors indicate open water. The merged polygonal pond, our main focus, is marked by a red outline. The wind sectors are shown as colored wedges.

et al. (2015) who also reported emissions from pond centers of a similar magnitude to tundra fluxes. Knoblauch et al. (2015) investigated smaller ponds also on Samoylov Island. Nevertheless, the similarity between the two landscape classes is noteworthy since processes of methane transport differ substantially between them. Bigger differences between the two land-cover classes have been recorded in other regions (Jammet et al., 2017).

One shore section displays higher methane emissions.

Most interestingly, methane fluxes to the atmosphere are especially high from one of the shores (Fig. 3.2, Shore 120 °: 19.18 $^{24.47}_{14.26}$ mg m^{-2} d^{-1}, $\mathrm{Median}\ ^{75\%\mathrm{Percentile}}_{25\%\mathrm{Percentile}}$). With the measurements we conducted, we can not identify the reason for these higher emissions. Through testing, we can exclude meteorological conditions like wind speed or temperature, a specific vegetation coverage favoring exceptionally high plant-mediated transport, recent shoreline degradation, and ebullition events. The most reasonable process which we suspect is seep ebullition, which is simply ebullition occurring over a prolonged period (Walter et al., 2006). In contrast, ebullition events are short-lived and are often caused by air pressure changes, which should have been detectable in the eddy covariance output (Iwata et al., 2018).

3.5 CONSOLIDATING THE CARBON IMPACT OF PONDS

Carbon fluxes are comparable to other studies.

As emissions of ponds tend to be higher the smaller the pond (Holgerson and Raymond, 2016; Wik et al., 2016), the estimate of carbon emissions from the merged polygonal pond might be a conservative estimate for pond emissions from our study site. Nevertheless, the main finding that open-water emissions are comparable to tundra emissions is consistent with findings by Knoblauch et al. (2015). The methane and carbon dioxide fluxes from the pond studied here fall into the range of prior measurements (Tab. B.1 including Eugster et al. (2003), Jonsson et al. (2008), Sepulveda-Jauregui et al. (2015), Wik et al. (2016), and Jammet et al. (2017)).

We only consider the open-water season.

When the ice melts in spring, the methane and carbon dioxide which accumulate in the water column and under the ice are rapidly released. However, like many of the studies above, we only report fluxes from the open-water season. Prėskienis et al. (2021) documented that up to 52 % of the annual pond methane emissions are emitted in spring, and up to 13 % of the annual lake emissions. The spring flush contributed up to 80 % of the annual emissions for carbon dioxide in their study. These are rather high estimates, and Wik et al. (2016) estimated an average methane spring flush of 27 % for pan-Arctic thermokarst water bodies. Jansen et al. (2019) assessed that 15-30 % of the annual carbon dioxide emissions are emitted during spring. Regardless of the estimate, we can conclude that a substantial fraction of the annual emissions arise in spring, strengthening ponds' landscape impact.

The more ponds there are, the smaller is the landscape carbon uptake.

Nevertheless, during the open-water season, the landscape impact of ponds in terms of methane emissions is moderate but uncertain. In our study, one of the pond's shorelines features above-average emissions, probably due to seep ebullition. We still need further studies to constrain better the causes and locations of seep ebullition in our study region. Possible methods to identify seep ebullition include counting bubbles in the ice in winter or employing funnels or chambers. Only then can we better constrain the landscape impact of methane emissions. We find that ponds are a carbon source rather than a sink like the surrounding landscape. To conclude, the higher the pond coverage, the lower is the carbon sink function of the overall landscape.

4

CHANGING POND EMISSIONS UNDER WARMING

4.1 ARCTIC AMPLIFICATION AND PONDS

What is Arctic amplification?

The high latitudes are warming faster than the rest of the world (Chapman and Walsh, 1993; Bekryaev et al., 2010). For the Northern Hemisphere, the term *Arctic amplification* was coined to describe the above-average warming rate. The reasons for this phenomenon are complex (Serreze and Barry, 2011). Much of the Arctic amplification has been attributed to the loss of sea ice (Screen and Simmonds, 2010b; Dai et al., 2019). Sea-ice loss alters the surface energy fluxes and ultimately leads to an increased energy transfer from the ocean to the atmosphere (Deser et al., 2010; Screen and Simmonds, 2010a; Chemke et al., 2021). In addition, the dynamics of atmospheric and oceanic energy transport into the Arctic modulate the strength of Arctic amplification (Graversen et al., 2008; Chylek et al., 2009; Yang et al., 2010), as do the dynamics in atmospheric moisture transport and changes in cloud cover (Intrieri et al., 2002; Barton and Veron, 2012; Sang et al., 2022).

arctic vs. global temperatures

Despite interdecadal variation in strength, it has been shown that in recent decades the Arctic has warmed about twice as fast as the rest of the world (Chylek et al., 2009). That implies that even with a global mean temperature increase of 1.5 °C, we expect the Arctic to warm by more than 3 °C (Hoegh-Guldberg et al., 2018).

4.1.1 *RAMIFICATIONS OF WARMING FOR PONDS*

Ponds are vulnerable to warming.

This pronounced warming brings about numerous changes in arctic tundra landscapes, and ponds are especially vulnerable to these changes. This vulnerability partly originates in their small size compared to lakes, which leads to low thermal inertia. In other words, pond temperatures respond faster to atmospheric temperature changes than lake temperatures because ponds are shallower than lakes. The responsiveness also enhances evaporation. In addition, total annual evaporation rises with a longer ice-free season, as does subsurface runoff (Riordan et al., 2006; Anderson et al., 2013). The continued existence of ponds and lakes in permafrost regions is often dependent on the frozen ground, which limits the subsurface runoff of water. The deeper the unfrozen soil layer in summer and the longer part of the soil stays unfrozen, the more water drains from the water bodies. Thus, thawing permafrost can induce drainage, especially of shallow water bodies, like ponds (Jepsen et al., 2013). Disappearing ponds have

already been observed in several regions of the Arctic (Riordan et al., 2006; Andresen and Lougheed, 2015).

warming can cause pond inception.

In our study region, however, rising temperatures can also initiate pond formation. When the ice wedges, the characteristic of the polygonal tundra, start melting, new ponds can form on top of them (Jorgenson et al., 2006; Liljedahl et al., 2016). While already-existing ponds emit predominantly contemporary carbon (Negandhi et al., 2013; Bouchard et al., 2015; Dean et al., 2020), ponds formed on top of degrading ice wedges might emit older carbon providing additional greenhouse-gas forcing to the climate system (Prėskienis et al., 2021).

Biological response to warming

Apart from these physical processes, warming also has biological implications. Higher temperatures can shift the methanogenic communities in the pond and make them much more productive, leading to substantially higher methane emissions from ponds (Zhu et al., 2020). Furthermore, we can already observe changes in arctic vegetation in response to higher temperatures and resulting changes in arctic hydrology (Bhatt et al., 2013; Winkler et al., 2021). With increasing productivity of macrophytes, we also expect an improved substrate quality leading to higher pond methane emissions (Joabsson et al., 1999; Joabsson and Christensen, 2002; Ström et al., 2012). This chapter investigates the response of methane emissions from ponds to rising temperatures. How much more methane is released per degree of local warming? Which processes and methane pathways are responsible for the emission increases?

4.2 INTRODUCING MeEP

MeEP was developed for polygonal-tundra ponds.

My target is to assess and understand the changes of pond methane emissions with warming on the landscape scale. I develop the model MeEP, which stands for *Methane Emissions from Ponds*, to investigate these changes. I design MeEP having the polygonal tundra in mind. Thus, MeEP accounts for the three dominant pond types of the polygonal tundra: ice-wedge ponds, polygonal-center ponds, and merged polygonal ponds. In addition, MeEP includes freeze and thaw processes of both the ponds and the surrounding soils. The polygonal tundra of Samoylov Island has been extensively measured, including measurements of pond methane fluxes. Using the data published by Knoblauch et al. (2015), I can tune the individual pathways of methane and the overall magnitude of methane emissions from overgrown and open-water areas of ponds to fluxes measured in our study region. Comparing all individual measured and modeled fluxes results in a root-mean-squared error of 9.7 nmol m^{-2} s^{-1} at an average flux of 13.6 nmol m^{-2} s^{-1}. Emissions range from 0.007 nmol m^{-2} s^{-1} to 62.8 nmol m^{-2} s^{-1}. The model captures 65 % of the variability in the measurements. Please refer to appendix C for more detail on the tuning

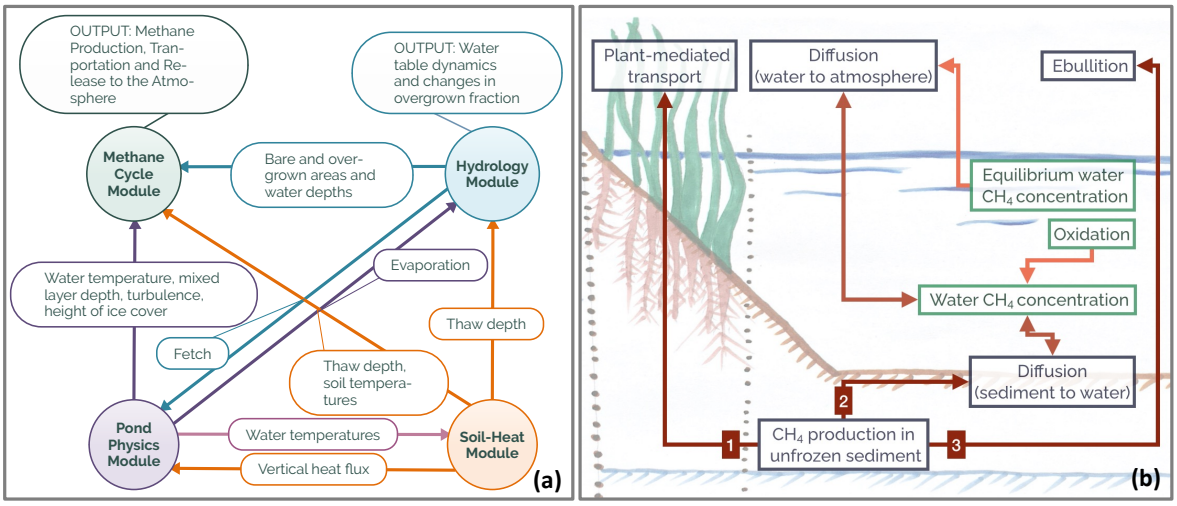

Figure 4.1: Schematics visualizing the structure of MeEP. Modules constituting MeEP are shown in (a) as colored circles. The variables used to couple the modules are labeling the arrows between the modules. The relevant output variables of the methane and hydrological module are listed above the respective module. In (b), we see an overview of the pathways of methane to the atmosphere in MeEP during the open-water season, including the order in which the different emission pathways of methane are computed (numbers in brown boxes). Production is computed separately for the overgrown and open-water part of the pond to account for the additional substrate provided by the macrophytes in the overgrown pond fraction. We compute the plant-mediated transport in the overgrown part of the pond, while diffusion and ebullition are computed for both pond parts.

and for the complete study. Before summarizing the main findings, I will give a short overview of how MeEP works in the following.

4.2.1 *MeEP STRUCTURE*

MeEP simulates ponds and the surrounding soil.

MeEP consists of four modules (Fig. 4.1(a)). The pond physics module uses an adapted version of the lake bulk model FLake (Mironov, 2005) to simulate water temperatures, ice dynamics, and energy fluxes between the water and the atmosphere. The soil physics are computed with a simplified version of the CryoGrid permafrost model, similar to the one applied in Langer et al. (2016). This model computes sediment temperatures and thaw depth. I develop a hydrological module for a first-order estimate of water-table dynamics and a module for methane dynamics. Here, I will introduce the methane module briefly. A detailed description of the hydrological module and the methane module is part of appendix C.

4.2.2 *THE METHANE MODULE*

MeEP simulates diffusion, ebullition, and the plant-mediated transport.

The methane module is separated into a description of the open-water season (Fig. 4.1(b)), and one for the ice-covered season. Independent of the season, methane is produced in the unfrozen layer of the sediment. When the sediment eventually freezes at the beginning of winter, methanogenesis ceases. If the pond is ice-covered, the methane remains in the water column, either dissolved or in gaseous form, and can be oxidized as long as oxygen is available. During the open-water season, the pond is divided into an open-water and an overgrown part. We compute the plant-mediated transport only for the overgrown part. There, the plant-mediated transport is the first flux type MeEP determines. Next, MeEP computes diffusive fluxes based on a concentration gradient between the pond sediment and the atmosphere and based on oxidation. All the methane left in the sediment, after diffusive fluxes were computed, emitted through ebullition. This means methane production and emissions are considered to be in equilibrium in each time step.

4.2.3 *SIMULATION OVERVIEW*

I study ponds on the landscape scale.

I simulate pond methane emissions under rising temperatures. To determine the landscape-scale pond methane emissions, I use the landcover classification described in the last chapter. The landcover classification provides data on each water body on Samoylov Island, including area, overgrown fraction, and the type of each pond (ice-wedge, polygonal-center, or merged polygonal ponds). With this classification, I can upscale the model output to the landscape scale since we know the total area covered by each pond type. The classified ponds are shown in Fig. 1.3(b).

Simulations cover present-day climate and warmer climatic conditions.

I force the model with a mix of data from reanalysis (ERA5, Hersbach et al., 2020) and remote sensing (MODIS, Myneni et al., 2015). I always use the grid cell covering Samoylov Island in the Lena River Delta. The remote-sensing data is used for the vegetation-related forcing variables (leaf-area index and net-primary productivity). Reanalysis and remote-sensing provide forcing for a historical period, and I employ them in a simulation covering the years 2002 – 2019 (simulation name *hist_all*). I then adapt this forcing to simulate the Arctic with higher mean temperatures.

Forcing for warmer climatic conditions

To imitate higher temperatures using the forcing for the historical period, I exploit MPI-ESM[1] simulations (Mauritsen et al., 2019; Wieners et al., 2019) from the 1pctCO2-scenarios of CMIP6[2] (Eyring et al.,

1 MPI-ESM is the earth system model developed at the Max-Planck Institute for Meteorology (Giorgetta et al., 2013; Mauritsen et al., 2019)

2 CMIP6 stands for the sixth phase of the *Coupled Model Intercomparison Project*, which assesses the performance of several earth system models by comparing standardized simulations.

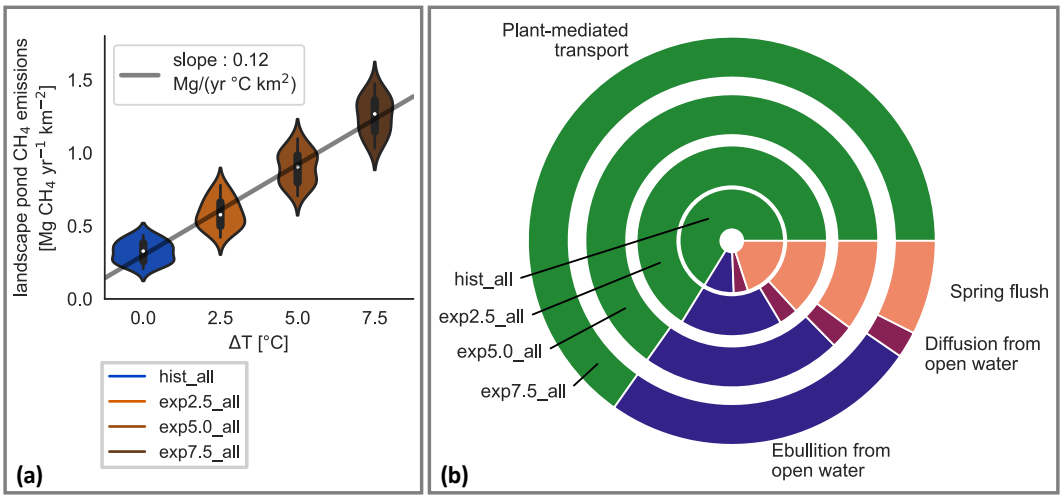

Figure 4.2: MeEP simulation results. In panel (a), we see a linear regression of the annual pond methane emissions per square kilometer of river terrace versus the local increase in local annual mean temperature of each simulation. The distribution of annual emissions per year in each simulation is depicted as a violin plot: The more often a certain y-value occurs within a simulation, the wider the shape is. The y-axis indicates the sum of the annual methane emissions of all ponds on Samoylov Island. In panel (b), the contribution of each flux type to annual mean emissions is depicted by the size of the respective circle segment. The area of each circle is proportional to the absolute methane emissions of the average year in each simulation.

2016). In the 1pctCO2-scenario, the carbon dioxide concentration in the atmosphere is consistently increased by 1 % per year resulting in steady global warming. I fit linear or quadratic regressions to the monthly means of the forcing variables I need against the annual mean air temperature using again the grid cell covering Samoylov Island. With the regressions, I compute the monthly response ΔX of a forcing variable X to a given local increase in the local annual air temperature of ΔT. To each forcing variable X from the forcing for the historical period, I add ΔX. In this way, I obtain a forcing for a 2.5 °C, a 5.0 °C and 7.5 °C warmer Arctic, and run one simulation for each case (simulation names *exp2.5_all*, *exp5.0_all*, and *exp7.5_all*, respectively).

Isolating drivers

I investigate the drivers of emissions changes with additional simulations, which mix the forcing for the historical period with the forcing of a 5 °C warmer Arctic. These simulations isolate the impact of hydrology, of vegetation, and of the combined effect of higher temperatures and a longer open-water season on emissions.

4.3 POND METHANE EMISSIONS IN A WARMER ARCTIC

Pond areas decrease slightly with rising temperatures.

Landscape-scale pond methane emissions increase with the annual average of the air temperature by 1.08 g CH_4 $year^{-1}$ $°C^{-1}$ per square meter of pond area (Fig. 4.2). This emission increase corresponds to 180 % higher emissions in the exp5.0_all simulation than in the hist_all simulation. Pond areas decrease slightly with warming by 2 ± 3 % (mean $\pm$ standard deviation) between the historical simulation and the simulation with a temperature increase of 7.5 °C. Thus, water-table changes lead to a slight decrease in landscape-scale pond methane emissions. This projection is a first-order estimate of water-table and pond-area dynamics. It does not include processes like pond formation, which is likely to occur especially along currently undegraded ice-wedges (Bouchard et al., 2020; Wickland et al., 2020). I also do not account for channel formation along connected ponds, which might intensify pond drainage (Cresto Aleina et al., 2015). Thus, trends in pond cover may be largely over- or underestimated, while I expect a reasonable seasonal cycle.

Vegetation changes drive methane emissions increases.

More abundant and more productive macrophytes, as well as a longer, warmer open-water season, raise annual emissions in contrast to water-table dynamics, which reduce landscape-scale pond methane emissions. Vegetation has a much stronger impact compared to changes in length and temperature of the open-water season. In MeEP, the impact of macrophytes on methanogenesis is prescribed using a linear relationship. We know that vascular plants strongly impact tundra methane emissions by providing substrate to methanogenesis (Joabsson et al., 1999; Andresen et al., 2016; Turner et al., 2020). Unfortunately, data regarding the strength of this relationship is lacking. There are no measurements that constrain the impact of emergent macrophytes on methanogenesis in arctic ponds. With future measurements, the parameterization in MeEP could be improved, and uncertainty regarding the strength of the emission increase reduced. Nevertheless, my findings highlight the importance of the connection between methanogenesis and macrophyte productivity as a driver of pond methane dynamics.

Plant-mediated transport is the dominating emission pathway.

The share of plant-mediated transport is nearly the same in all simulations regarding the relative contribution of the methane pathways to the overall pond emissions. This indicates that the macrophytes' capacity to conduct methane increases at least at the same rate as the methanogenesis. However, we observe changes in the relative contribution of the spring flush, diffusive fluxes, and ebullition in the open-water parts of ponds. While the relative contribution of the spring flush decreases, ebullition becomes a more important methane-emission pathway. Since only little of the methane emitted through ebullition is oxidized, more methane produced in the sediment can reach the surface.

In conclusion, the simulations with MeEP indicate that ponds will become stronger sources of methane in the future and that much of the emission increase is mediated through increased biomass and productivity of macrophytes.

4.4 MEEP ON A PAN-ARCTIC SCALE

MeEP is a versatile tool.

MeEP can easily be applied to the pan-Arctic, either as a whole or only using some of the modules, making it a versatile tool for landscape-scale and large-scale studies. There are still uncertainties regarding trends of pond evolution, both on the landscape and on the pan-Arctic scale (Bring et al., 2016). Including these processes in MeEP is beyond the scope of this thesis. However, the results from the study above show that even combining MeEP with a rough estimate of future pond coverage can give valuable insight into future pond methane emissions. Ideally, such a large-scale approach would also account for the dynamics in macrophytes. At the moment, MeEP does not differentiate between different plant species. However, some species are more efficient than others in conducting methane (Knoblauch et al., 2015). Incorporating species information in MeEP will improve my emission estimates, but data on macrophyte distribution are hard to come by.

Impacts of macrophytes on methane dynamics should be included on the large scale.

When considering present-day pond emissions, combining MeEP with a map of dominant macrophyte species can improve estimates of pan-Arctic methane emissions. Even without this map, the big advantage of MeEP is that it accounts for all three pathways of methane emissions from ponds, in contrast to previous upscaling efforts (Wik et al., 2016; Polishchuk et al., 2018; Zabelina et al., 2020) which do not include plant-mediated methane emissions. I show that this emission pathway is the most important in our study region.

5 SUMMARY AND CONCLUSIONS

5.1 MY FINDINGS ON PONDS AND METHANE

In the introduction, I posed three research questions. We have explored various aspects regarding each of them and can now briefly summarize our answers.

WHAT DRIVES THE SPATIAL VARIABILITY OF METHANE CONCENTRATION IN POLYGONAL-TUNDRA PONDS?

1st research question

In the polygonal tundra, I find that geomorphology is one of the most important drivers of pond methane concentrations as it controls many pond properties. First and foremost, due to distinct geomorphology, the ponds can be divided into three types, which have specific properties: ice-wedge ponds, polygonal-center ponds, and merged polygonal ponds.

- Due to their geomorphology, *ice-wedge ponds* have an elongated shape and cold bottom temperatures. These two characteristics support stratification in ponds of this type. Consequently, surface methane concentrations depend strongly on the amount of methane accumulated in the hypolimnion and wind speed, which enhances mixing.
- In *polygonal-center ponds*, water depth is an important driver of surface methane concentrations. Shallower ponds mix more efficiently. Furthermore, they have a higher overgrown fraction enhancing the soil's organic content. Since methanogenesis depends on substrate availability, a higher macrophyte cover results in higher surface methane concentrations.
- *Merged polygonal ponds* are the deepest and largest ponds. Surface methane concentrations depend on how well-developed stratification is due to their larger size compared to the other pond types. Similar to polygonal-center ponds, methane concentrations in this pond type are substrate-dependent: the shallower the ponds, the higher the vegetation cover, and the higher the surface methane concentrations.

WHAT IS THE IMPACT OF POLYGONAL-TUNDRA PONDS ON THE LANDSCAPE CARBON BUDGET?

2nd research question

Using eddy covariance measurements of both the tundra and a larger merged polygonal pond, I show that the tundra is a net sink of carbon

dioxide during the open-water season. In contrast, the pond is a source. Not accounting for ponds leads to an overestimation of the landscape uptake by 11%.

Methane emissions from pond and tundra are comparably high, but pond methane emissions show substantial spatial variability. One of the shore regions emits significantly more methane than the rest of the measured area. We hypothesize that this increase is due to seep ebullition, which warrants more measurements using, for example, funnels or chambers.

In conclusion, ponds are a relevant landscape source of carbon with strong variability in methane emissions.

3rd research question

HOW DO METHANE EMISSIONS FROM POLYGONAL-TUNDRA PONDS CHANGE UNDER WARMING?

Employing the novel model MeEP, which resolves the three distinct pond types of the polygonal tundra, I show that pond methane emissions increase by 1.08 g CH_4 $year^{-1}$ $°C^{-1}$ per square meter of pond area. At the same time, the projected pond area only decreases slightly. However, the modeled water-table dynamics are only a first-order estimate. Better projections of future pond areas, including pond formation, drainage, and shore erosion, are needed to estimate future pond methane emissions conclusively. Nevertheless, ponds will emit more methane per unit area as the climate warms, and much of this emission increase is caused by macrophytes. Vascular-plant productivity increases with warming and provides more substrate for methanogenesis. In all simulations, plant-mediated transport is the mechanism contributing most to methane emission on the landscape scale. Moreover, I find that ebullition becomes more important as the climate warms while the influence of the spring flush decreases.

5.2 IMPLICATIONS OF THIS DISSERTATION

Variability of methane

This dissertation investigates methane dynamics in polygonal-tundra ponds on the landscape scale. We know that methane is highly variable, and I show that much of this variability is connected to the geomorphology of ponds. The drivers of spatial variability might be transferable from our study region to other polygonal-tundra landscapes. However, I want to highlight one finding, which I deem relevant for other landscape types as well: a higher vegetation cover leads to higher methane concentrations in polygonal-center and merged polygonal ponds. The same trend might apply to ice-wedge ponds but could be masked by stratification in our measurements.

Ebullition needs sufficient substrate.

We could not extract the emissions from the overgrown water from the eddy covariance measurements in the second study, and we only suspect seep ebullition to be the cause of the high emissions from one

shore. Nevertheless, we know that methane productivity and ebullition are linked (DelSontro et al., 2016) and that vascular plants enhance substrate quality (Joabsson and Christensen, 2002; Ström et al., 2003). Thus, a reasonable hypothesis is that the locally high emissions are fueled by substrate derived from the nearby macrophytes.

Emissions from the littoral zone are high.

Lastly, my model simulations project that the impact of vegetation will only become more pronounced with warming due to increases in biomass and vascular-plant productivity. The estimate from MeEP relies on a parameterization that needs to be improved with additional measurements, which are not available at the moment. This leads to uncertainty regarding the strength of the pond-methane response, but, generally, the response we see is in line with my first study, which concludes that ponds are substrate-limited at present. Hence, the additional substrate provided by emergent macrophytes leads to rising methane emissions. We know that the vegetated littoral zone contributes out-of-proportion to the methane budget of boreal lakes (Juutinen et al., 2003). Thus, I expect plant-mediated transport and vegetation cover are important for pond methane emissions on the pan-Arctic scale. Most upscaling studies neglect the impact of vegetation. These studies might substantially underestimate pond methane emissions.

Ponds in the spotlight

If a study concentrates solely on ponds, the focus usually lies on individual ponds. If water bodies are studied in general, the focus often lies on larger lakes. This dissertation highlights ponds as an important landscape feature of the polygonal tundra. It presents the first study that estimates landscape-scale methane emissions from tundra ponds including not only diffusive fluxes and ebullition but also plant-mediated transport.

APPENDICES

A

IDENTIFYING DRIVERS BEHIND SPATIAL VARIABILITY OF METHANE CONCENTRATIONS IN EAST SIBERIAN PONDS

The work in this appendix has been published as:

Rehder Z., Zaplavnova A. and Kutzbach L. (2021). "Identifying Drivers Behind Spatial Variability of Methane Concentrations in East Siberian Ponds." In: *Front. Earth Sci.* 9:617662. DOI: 10.3389/feart.2021.617662

AUTHOR CONTRIBUTIONS

ZR: conceptualization (equal), formal analysis (lead), investigation (lead), and writing - original draft. AZ: formal analysis (supporting) and investigation (supporting). LK: conceptualization (equal), formal analysis (supporting), and writing - review and editing. All authors contributed to the article and approved the submitted version.

DATA AVAILABILITY

Data has been published at https://doi.org/10.1594/PANGAEA.922399 (Rehder et al., 2020)

Identifying drivers behind spatial variability of methane concentrations in East Siberian ponds

Zoé Rehder [1,2], **Anna Zaplavnova** [3,4] **and Lars Kutzbach** [5]

Received: 15 October 2020 – Accepted: 01 March 2021 – Published: 26 March 2021.

[1] Max Planck Institute for Meteorology, Hamburg, Germany

[2] International Max Planck Research School on Earth System Modelling, Hamburg, Germany

[3] Department of Geology and Geophysics, Novosibirsk State University, Novosibirsk, Russia

[4] Trofimuk Institute of Petroleum Geology and Geophysics of Siberian Branch of Russian Academy of Sciences, Novosibirsk, Russia

[5] Institute of Soil Science, Universität Hamburg, Hamburg, Germany

ABSTRACT

Waterbody methane emissions per area are negatively correlated with the size of the emitting waterbody. Thus, ponds, defined here as having an area smaller than $8 \cdot 10^4$ m^2, contribute out of proportion to the aquatic methane budget compared to the total area they cover and compared to other waterbodies. However, methane concentrations in and methane emissions from ponds show more spatial variability than larger waterbodies. We need to better understand this variability to improve upscaling estimates of freshwater methane emissions. In this regard, the Arctic permafrost landscape is an important region, which, besides carbon-rich soils, features a high pond density and is exposed to above-average climatic warming. We studied 41 polygonal-tundra ponds in the Lena River Delta, northeast Siberia. We collected water samples at different locations and depths in each pond and determined methane concentrations using gas chromatography. Additionally, we collected information on the key properties of the ponds to identify drivers of surface water methane concentrations.

The ponds can be categorized into three geomorphological types with distinct differences in drivers of methane concentrations: polygonal-center ponds, ice-wedge ponds and larger merged polygonal ponds. All ponds are supersaturated in methane, but ice-wedge ponds exhibit the highest surface water concentrations. We find that ice-wedge ponds feature a strong stratification due to consistently low bottom temperatures. This causes surface concentrations to mainly depend on wind speed and on the amount of methane that has accumulated in the hypolimnion. In polygonal-center ponds, high methane surface concentrations are mostly determined by a small water depth. Apart from the influence of water depth on mixing speed, water depth controls the overgrown fraction, the fraction of the pond covered by vascular plants. The plants provide labile substrate to the methane-producing microbes. This link can also be seen in merged polygonal ponds, which furthermore show the strongest dependence on area as well as an anticorrelation to energy input indicating that stratification influences the surface water methane concentrations in larger ponds. Overall, our findings underpin the strong variability of methane concentrations in ponds. No single driver could explain a significant part of the variability over all pond types suggesting that more complex upscaling methods such as process-based modelling are needed.

A.1 INTRODUCTION

Ponds are small waterbodies that are often defined by their area with varying thresholds. Here, we follow the Ramsar classification scheme, which sets a comparably high limit of $8 \cdot 10^4$ m^2 (Ramsar Convention Secretariat, 2016). Notably, ponds are the most common waterbody type in the Arctic (Muster et al., 2017) and emit more methane (CH_4) per area than larger lakes (Juutinen et al., 2009; Downing, 2010; Holgerson and Raymond, 2016; Wik et al., 2016). Thus, they are important contributors to the methane budget of the Arctic. The variability of methane emissions and concentrations is also higher in ponds than it is in lakes (Juutinen et al., 2009; Laurion et al., 2009; Sepulveda-Jauregui et al., 2015; Holgerson and Raymond, 2016) and uncertainty remains as to what causes the variability. In this study, we focus on identifying drivers of local methane concentration variability. A good grasp on the main mechanisms responsible for spatial variability is essential to improve upscaling and modeling of water methane emissions.

Previous upscaling efforts of methane emissions from lakes and ponds differ considerably. Holgerson and Raymond (2016) estimate global waterbody methane emissions of 12 Tg CH_4-C yr^{-1} through diffusion only. Accounting additionally for ebullition Wik et al. (2016) estimates that ponds and lakes north of 50 °N alone emit the same amount. DelSontro et al. (2018), on the other hand, state an estimate for global emissions from lakes and reservoirs of 112 Tg CH_4-C yr^{-1}. This is nearly ten times as high as the estimate from Holgerson and Raymond (2016) who exclude reservoirs but still assume a larger total waterbody area than DelSontro et al. (2018). All three estimates are all based on varying total areas of lakes and ponds, but part of the spread can also be explained by varying upscaling methods. Each study assumes a different main predictor of water methane concentrations: While Holgerson and Raymond (2016) use size classes and Wik et al. (2016) waterbody type as the predictor, DelSontro et al. (2018) use chlorophyll (a proxy for the trophic state of the waterbody and its productivity). This approach is supported by Rinta et al. (2017) who find higher methane emissions from (more productive) central European as opposed to boreal lakes. Contrastingly, Arctic waterbodies tend to still have significant carbon emissions but low primary productivity due to low energy input and due to nutrient deficiencies (Anderson et al., 2001; Hamilton et al., 2001; Ortiz-Llorente and Alvarez-Cobelas, 2012). These waterbodies are very sensitive to changes in allochthonous carbon and nutrient inputs, changes we expect due to climate-change-induced permafrost thaw (Vonk et al., 2015; Burpee et al., 2016). Note, that small absolute changes in inputs have a stronger impact the smaller the waterbody is due to a smaller water volume.

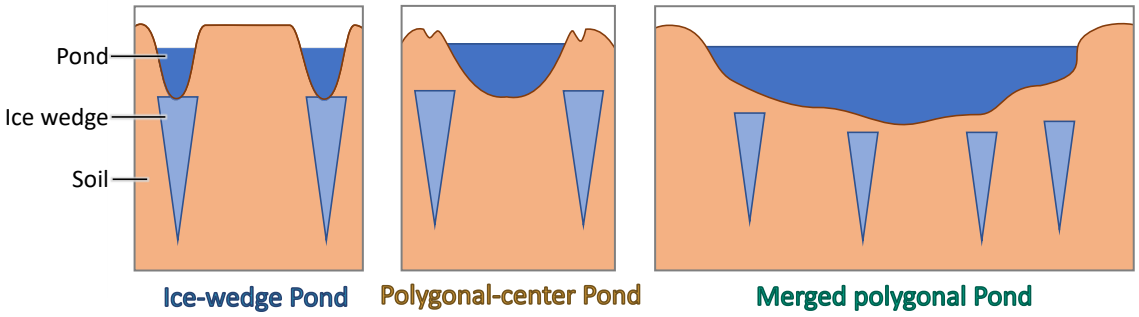

Figure A.1: Schematic of the different pond types in the polygonal tundra. Ice-wedge ponds form along the edges of polygons on top of ice wedges, have a frozen bottom and have often an elongated shape and a steep slope. Polygonal-center ponds from in between ice wedges, in the center of the polygons. They tend to be nearly circular. If several polygons subside, merged polygonal ponds form. These ponds are the largest pond type of the three.

Lake size, with depth being a better predictor than area, is the main predictor in a study of small Finnish lakes (Juutinen et al., 2009). Secondary drivers include the oxygen status and nutrient availability within the lake. Even when considering these drivers, the authors find a large variability in methane concentrations ($r^2_{adj.} < 0.4$ for surface concentrations) with an average summer surface concentration of 0.25 µmol L^{-1}. Higher average concentrations have been found in the Western Siberian Lowlands (0.98 µmol L^{-1} in waterbodies larger than $5 \cdot 10^{-4}$ km^2 and 9 µmol L^{-1} in waterbodies smaller than $5 \cdot 10^{-4}$ km^2). Note that small waterbodies have concentrations one order of magnitude greater than larger lakes. Even though this relation is striking, the spread around it is still broad ($r^2 < 0.3$) (Polishchuk et al., 2018).

Both the study by Polishchuk et al. (2018) and the study by Juutinen et al. (2009) cover a large area. Focusing on a specific region reduces driver variability due to deviating environmental conditions. For the polygonal tundra of northern Canada, Negandhi et al. (2013) found that methane concentration depend on waterbody type (Fig. A.1): In the polygonal tundra, waterbodies can form in the center of polygon (polygonal-center ponds) or along the edges of a polygon. These edges are underlain by ice wedges, so ice-wedge ponds still have ice at their bottom. According to Negandhi et al. (2013), ice-wedge ponds exhibit significantly higher methane emissions than polygonal-center ponds, which contain a higher number of methane-consuming microbes (methanotrophs) and more dissolved oxygen, while the methane-producing microbes (methanogens) in ice-wedge ponds are more adapted to high substrate availability. But even when separating by pond type, the standard deviation of the surface methane concentra-

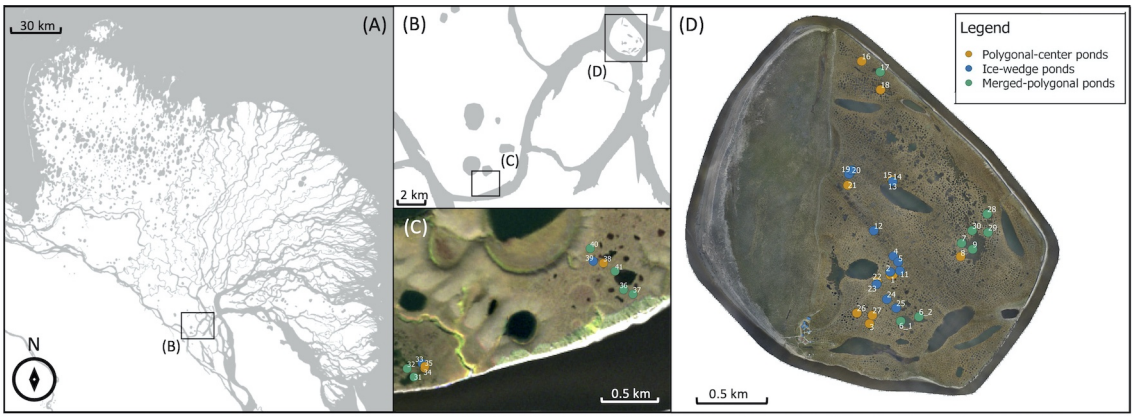

Figure A.2: Overview of study region. The Lena River Delta (A) is located in Eastern Siberia at the coast of the Laptev Sea. Samoylov and Kurungakh Island are situated in the southern end of the Delta ((B) - (D)).

tions is still approximately as high as the respective mean, indicating that there is still strong variation in surface methane concentrations within each group which needs an explanation.

Polygonal tundra is prevalent throughout the lowlands of the Arctic, and often peatlands form in these patterned-ground landscapes characterised by a pronounced microrelief (French, 2007; Minayeva et al., 2016). Especially in the centers of the polygons, where the water table is higher than along the rims of the polygons, peat forms. These landscapes feature a high density of small waterbodies and carbon-rich soils. Here, we build on the work by Negandhi et al. (2013) and investigate what drives variability in methane concentrations of ponds in the polygonal tundra of Eastern Siberia. We include a wide range of variables, from wind speed over vegetation cover to geomorphological pond type. Notably, we also include the effect of submerged mosses on methane-concentration variability. These mosses photosynthesize and create an oxic zone at the bottom to the pond, where methane can be oxidized. This layer is often strongly enriched with methane, and concentrations drop steeply above the moss layer (Liebner et al., 2011; Knoblauch et al., 2015). Though these effects are known, it is unknown how submerged mosses impact methane concentrations on the scale of a whole pond.

A.2 MATERIALS AND METHODS

A.2.1 *SITE DESCRIPTION*

We studied 41 ponds on the islands Samoylov and Kurungakh (Fig. A.2). The two islands are located in the Lena River Delta of Eastern Siberia in a zone of continuous permafrost with an annual mean tem-

perature of -12.5 °C (Boike et al., 2013). The delta can be divided into three terraces of different genesis. The first terrace is the youngest, it formed in the Holocene through fluvial deposition. This terrace is the wettest, has the most pronounced microtopography due to active ice-wedge polygon formation and consequently the highest density of small-scale waterbodies (Schwamborn et al., 2002; Schneider et al., 2009; Muster et al., 2012). Both Samoylov and the southern tip of Kurungakh belong to the first terrace, and here we sampled 35 ponds in total. Six additional ponds were measured further north on Kurungnakh on the third terrace. The third terrace consists of sandy deposits overlain by an ice complex which formed in the Pleistocene. This organic-rich ice complex then is often overlain again by Holocene deposits (Schwamborn et al., 2002; Wetterich et al., 2008). The locations we sampled on the third terrace exhibited only weak polygonal structures, and especially smaller waterbodies were more sparse than on the first terrace. Still, overall roughly 20% percent of the delta (excluding the river) are covered by waterbodies — in the first terrace we find most small waterbodies while the third terrace has a higher fraction of large thermokarst lakes (Muster et al., 2012). The second terrace features less ponds and has not been sampled.

We divided the waterbodies into three groups based on their geomorphology (Fig. A.1). Ponds which formed in the center of a single polygon with intact rims are labelled polygonal-center ponds. These ponds are mostly circular and only seldomly deeper than one meter. Ice-wedge ponds are ponds which formed on top of a thawing ice wedge along the edge of one or several polygons. These ponds tend to have an elongated shape and highly variable water depth with steep margins. Lastly, if several neighbouring polygons including their rims are inundated, we call them merged polygonal ponds. These ponds are the largest and differ most in size. They also usually have the gentlest slope. We sampled 15 polygonal-center ponds with areas ranging from 24 m^2 to 200 m^2, 13 ice-wedge ponds with areas between 13 m^2 and 252 m^2, and 14 merged polygonal ponds (area range 214 m^2 – 24301 m^2).

In the shallow parts and along the margins of all pond types, vascular plants species such as Carex aquatilis or Artcophila fulva grow (Knoblauch et al., 2015). On the bottom of many ponds, submerged brown mosses form a thick layer (Liebner et al., 2011; Knoblauch et al., 2015).

A.2.2 *GAS CONCENTRATION MEASUREMENTS*

We conducted the field measurements on 22 days between mid-July and the end of August during mid-day to afternoon. In each pond several water samples were taken within an hour. The number of samples was dependent on ground-cover heterogeneity: The ground

of a pond was either covered by vegetation like vascular plants or submerged mosses or vegetation free. For each pond, we took at least one sample over each ground-cover type, on average we took two samples. In total, we collected 116 surface water sample, 44 samples over sediment, 37 over moss and 33 in the overgrown part of ponds. The overgrown fraction got sampled least, as it covers a smaller part of the average pond than mosses. Most samples were taken over sediment, because most of the area of larger ponds has bare ground. To get a better estimate by including more spatial variability, in large ponds surface concentrations over sediment were taken more than once. Water samples were taken through three aluminum tubes which were fixed to a larger 2 m pipe. To this pipe, two floating bodies were attached (see Supplementary Fig. A.8). We carefully placed the pipe in the pond away from the margin with little disturbance of the water. Up to three samples were taken at one spot within the pond: One five centimeters below the water surface through the first aluminum tube; one at the bottom of the pond through a second aluminum tube which end could be lowered; and, if the water was deeper than about half a meter, one additional sample was taken at about 55 cm depth through a third aluminum tube. Water was sucked through the respective tube with 50 mL syringes. After flushing the syringes, a 30 mL water sample was inserted into 50 mL injection bottles, which, beforehand, had been evacuated and then filled with nitrogen. The samples were stored dark between sampling and measuring to avoid photolysis and microbial breakup of dissolved organic carbon. The gas in the headspace of the injection bottles was analyzed within 12 hours of sampling using a gas chromatograph (Agilent GC 7890, Agilent Technologies, Germany) with an flame ionization detector (FID). The headspace pressure in the injection bottle was measured with a digital manometer (LEO1, Keller, Switzerland). We estimate a loss of methane due to oxidation between sampling and gas chromatography measurement well below 5%. For this estimate, we use the mean potential methane oxidation rate for Alaskan non-yedoma lakes as determined by Martinez-Cruz et al. (2015) and the approach of the same authors to infer the in-situ oxidation rates by a double Monod model.

We computed the methane and carbon dioxide concentrations using the measured partial pressure of the respective gas in the headspace of the injection bottle, the ideal gas law and Henry's law with a temperature-dependent Henry's constant (Sander, 2015). The gas content of each injection bottle was measured at least twice.

A.2.3 *ENVIRONMENTAL SAMPLING*

Using the handheld meter WTW Multi 340i (Xylem Analytics, Germany) and, on the last day of measurements, a WTW Multi 350i, equipped with a CellOx325 probe we measured dissolved oxygen in

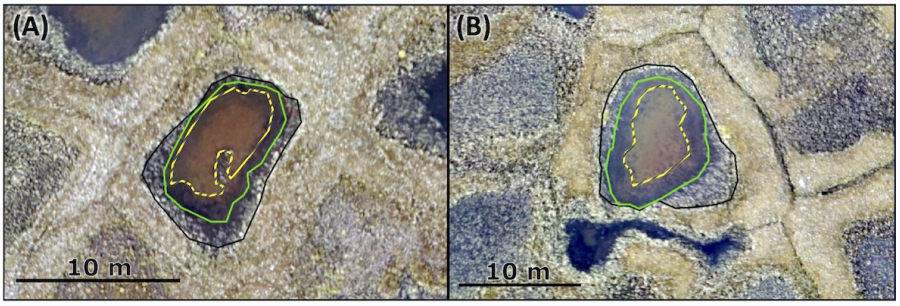

Figure A.3: Excerpt of the orthophoto shows two exemplary polygonal-center ponds, (A) shows pond 3, (B) shows pond 21. Both are located on Samoylov Island. The black line marks the edge of the pond, the green line delimits the overgrown area, and the yellow dashed line marks the moss-covered parts of the pond.

the pond water and water temperature with a SenTix41 probe. After each water sampling, we estimated the thaw depth of the ponds by driving a metal rod into the sediment until it hits the frozen ground. To assess water depth, we submerged a water-level logger Mini-Diver (DI501, Schlumberger Water Services, Netherlands) in the middle of the ponds. This diver measured temperature and hydrostatic pressure. Using a second diver which measured atmospheric pressure and the difference between the hydrostatic and atmospheric pressure, we computed water depth.

In each pond we collected two subaquatic top-sediment samples near the shore. The sediment sampling was done directly after the water sampling. According to Knoblauch et al. (2015) the top sediment exhibits higher methane production rates than deeper soil layers. We removed large roots from the samples, dried the sample for 24 hours at 105 °C and measured the sample mass. We then determined the organic fraction of the sample by burning it in a muffle furnace for four hours at 550 °C and remeasuring the mass.

For incoming short-wave radiation, data from a four-component net radiation sensor (NR01, Campell Scientific, UK) was used. Wind speed was measured with a omnidirectional ultrasonic anemometer (R3-50, Gill Instruments, UK). Both of these instruments were stationary installed on Samoylov Island, data was recorded at half-hourly intervals.

A.2.4 *IMAGERY*

We used an orthophoto map of Samoylov and Kurungakh obtained in 2016 (Kartoziia, 2019) to determine the area of each pond, the area covered by moss and the area overgrown by plants. The map has a resolution of 0.05 m px^{-1} thus providing enough detail to differentiate between surface types (see Fig. A.3). The orthophoto map

was loaded into the GIS software ArcGIS 10.2.2, in which the groundcover types were circled manually. The calculations of the enclosed areas were made in automatic mode in the GIS software QGIS. For very small ponds and for quality control, the areas computed through imaginary were compared to measurements of the pond diameter (see Supplementary Tab. A.2) and to measurements of the width of the overgrown margin taken during the measurement campaign with a measuring tape. When possible, we also visually estimated the moss-covered fraction, to compare with the orthophoto map. For ponds, where the orthophoto map resolution was insufficient, the area approximated by the tape measurements was used.

A.2.5 *STATISTICAL ANALYSIS*

For each time a pond was measured (water and environmental sampling), we averaged all measurements of surface methane concentrations and computed the standard deviation. To assign a standard deviation to those ponds with only one sample, we performed a linear regression between the standard deviation and the mean concentration of the ponds with more than one sample ($R^2 = 0.8$) and used the regression to predict the standard deviation of the ponds with one sample.

As a measure of correlation we applied the Kendall rank correlation index (Knight, 1966). The advantage of this Kendall's tau is that it does not assume a linear relation between the two variables in question. This is achieved by always comparing a pair of two points: If both variables show the same trend (increase or decrease) between two points, it is counted towards the concordant pairs. If one variable shows an increase and the other a decrease, the pair is counted towards the discordant pairs. The index then is computed as the difference between the concordant and the discordant pairs divided by the absolute number of pairs while accounting for ties. Analogously to the more common Pearson correlation, an index of 1 indicates a strong positive correlation, -1 indicates a strong negative correlation, and 0 indicates no correlation.

To investigate the relation between methane concentrations and individual drivers in depth, we used linear regressions based on ordinary least squares, with log-transformed variables when looking at the relation between pond area and surface methane concentrations. To evaluate the goodness of the fit, we utilize the error on the slope parameter and the root mean squared error (RMSE) as well as the predictive R^2. The predictive R^2 gives a measure of how well the regression model predicts new observations. It is determined by removing one measurement from the dataset, redoing the regression and predicting the removed measurement. After repeating this procedure for all measurements in the dataset, the predictive R^2 is computed

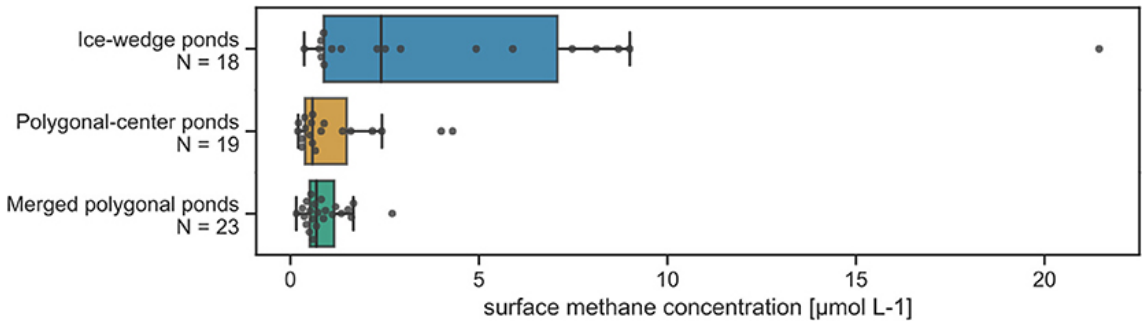

Figure A.4: Distribution of surface concentrations separated by pond type. Boxplots with median as well as all data points are displayed. Number of measurements (N) is stated below each boxplot.

using the true and the predicted values of the target variable. The predictive R^2 is sensitive to overfitting.

To determine if two distributions are statistically different we used the Kolmogorov-Smirnov test (Hodges, 1958), which is a general, non-parametic test, which is sensitive both to the shape and to the location of a distribution. All analysis was done in python 3.6 using the packages numpy 1.17 (Harris et al., 2020), scipy 1.5 (Virtanen et al., 2020), scikit learn 0.21 (Pedregosa et al., 2011) and matplotlib 3.2 (Hunter, 2007).

A.2.6 *EQUILIBRIUM CONCENTRATIONS*

The dissolved gas concentrations of methane and carbon dioxide for equilibrium conditions were computed using the mean measured water temperature, the mean air pressure, the mean atmospheric methane and carbon dioxide concentrations as measured by a nearby eddy-covariance station. Using a temperature-dependent Henry's constant $H(T)$ Sander (2015), the concentrations were computed via

$$c = H(T) \cdot p, \tag{A.1}$$

where c is the equilibrium concentration in water, and p is the partial pressure (atmospheric pressure multiplied by the mole fraction of methane or carbon dioxide).

A.3 RESULTS

Median concentrations in ice-wedge, polygonal-center and merged polygonal ponds, respectively, are 2.4 µmol L^{-1} (25 - 75th percentile: 0.9-7.1 µmol L^{-1}), 0.6 µmol L^{-1} (25 - 75th percentile: 0.4-1.5 µmol L^{-1}) and 0.7 µmol L^{-1} (25 - 75th percentile: 0.5-1.2 µmol L^{-1}). All these values are far higher than the average methane equilibrium concentration of 0.004 µmol L^{-1}, which was computed using the

Table A.1: Environmental conditions and geomorphological properties of the three pond types during the measurement campaign: dissolved oxygen (O_2), organic content in subaquatic topsoil (C_{org}), mean incoming shortwave radiation in the last 6 hrs after water sampling (SW_{in}), surface water temperature (T), thaw depth beneath the pond (TD), water depth (WD), area (A), bottom methane concentration (CH_4^{bot}), surface carbon dioxide concentration (CO_2), moss-covered fraction of the pond surface (f_{moss}) and fraction of pond overgrown by vascular plants (f_{veg}).

Pond type		**O_2** mg L^{-1}	**C_{org}** %	**SW_{in}** W m^{-3}	**T** C	**TD** cm	**WD** cm	**A** m^2	**CH_4^{surf}** µmol L^{-1}	**CH_4^{bot}** µmol L^{-1}	**CO_2** µmol L^{-1}	**f_{moss}** %	**f_{veg}** %	**wind speed** m s^{-1}
ice-	median	5	10	74	9	22	86	70	2.4	196.2	170	95	72	5
wedge	max	11	40	582	12	43	113	252	21.45	815.0	351	100	83	6
ponds	min	2	3	35	5	0	21	32	0.4	17.9	26	20	34	1
polygonal-	median	8	6	139	11	33	59	94	0.6	66.2	20	100	41	4
center	max	10	25	541	17	74	95	188	4.3	445.0	143	100	100	8
ponds	min	2	2	31	8	24	17	24	0.2	0.2	11	50	17	1
merged	median	11	6	81	10	44	na	1440	0.7	8.6	22	23	22	5
polygonal	max	12	17	468	14	81	na	24301	2.7	73.3	118	84	100	7
pond	min	5	2	44	8	37	na	214	0.2	0.5	5	0	6	3

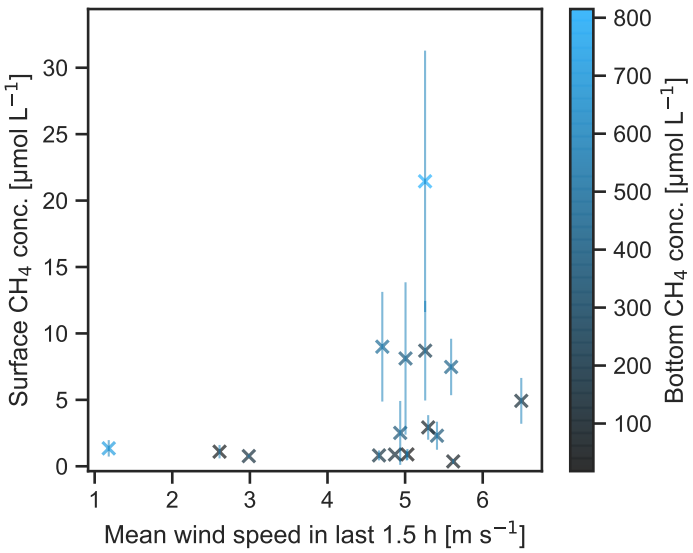

Figure A.5: Surface methane concentrations of the ice-wedge ponds in relation to mean wind speed in the last 1.5 hours and methane bottom concentrations.

mean water temperature of 9.7 °C, mean air pressure of 101.144 kPa and mean methane air concentration of 2 ppm. Additionally, all ponds exhibited stratification. When comparing surface concentrations to bottom concentrations over sedimented areas in the ponds, where mixing is not obstructed, bottom concentrations in ice-wedge ponds are on average more than 100 times larger than surface concentrations. For polygonal-center ponds and merged polygonal ponds, bottom concentrations still exceed surface concentrations by a factor of 42 and 38 on average (see Tab. A.1).

ICE-WEDGE PONDS

Ice-wedge ponds exhibit by far the highest methane concentrations and the largest spread in the distribution (Fig. A.4). In ice-wedge ponds, the surface concentrations tend to be low when wind speed is below 4 m s^{-1} (Fig. A.5). In this regime, the pond is stratified because bottom temperatures are much lower than in the other two pond types (5.9(2.5) °C versus 9.5(2.2) °C (mean with standard deviation)). With raising wind speeds maximum surface concentrations steeply increase. The strength of this increase mainly correlates with the bottom concentrations – the more methane there is at the bottom, the more gets mixed up (Kendall-tau correlation between bottom and surface methane concentrations for all wind speeds: $p < 0.05$, for wind > 4 m s^{-1} : $p < 0.01$). Both the bottom and the surface methane concentrations significantly correlate solely to each other.

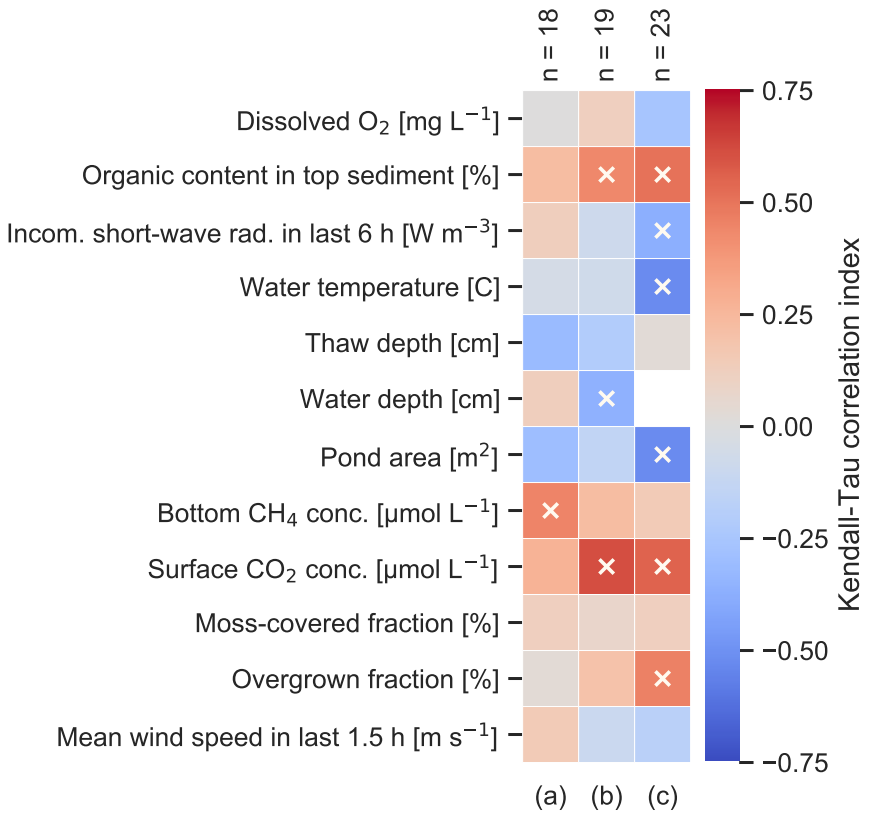

Figure A.6: Kendall-Tau correlation index of different variables with surface methane concentrations in (a) ice-wedge ponds, (b) polygonal-center ponds, (c) merged polygonal ponds. Significant correlations ($p < 0.05$) are marked by a white cross. Number of measurements per pond type (n) is indicated at the top of each column.

The next-strongest correlation of the bottom concentrations is with area ($p = 0.2$). Using area, wind speed and bottom concentrations as regressors in a multiple linear regression, we achieve a predictive R^2 of 0.6.

POLYGONAL-CENTER PONDS

While area was a good predictor for ice-wedge ponds, water depth is more potent for polygonal-center ponds (Fig. A.6). Water depth and area do not significantly correlate for this pond type ($p = 0.3$). Apart from water depth, surface methane concentrations in polygonal-center ponds also significantly correlate with organic content in the top sediment, and these two are slightly correlated with each ($p = 0.07$) and both significantly correlated with the overgrown fraction ($p < 0.05$). Using the first principle component of these three variables as input for a linear regression on the surface concentrations yields a predictive R^2 of 0.6.

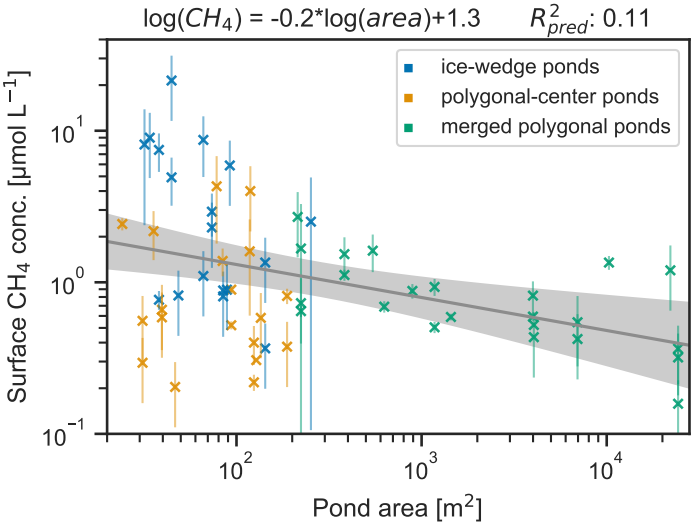

Figure A.7: Linear regression between the natural logarithm of methane surface concentrations and the natural logarithm of pond area. Shaded area indicates the 95% confidence band.

MERGED POLYGONAL PONDS

Polygonal-center and merged polygonal ponds have a similar range of methane surface concentrations, but merged polygonal ponds have the least skewed distribution among the three pond types (Fig. A.4). These ponds also correlate significantly to the largest number of environmental variables, like water temperature and incoming shortwave radiation (Fig. A.6). Using the first two principle components of the pond area, the overgrown fraction, the incoming shortwave radiation, dissolved oxygen and the organic content yields a predictive R^2 of 0.6.

POND-TYPE INDEPENDENT RESULTS

The relation between surface methane concentration and pond area can be approximated by a log-log relation (Fig. A.7). While the relation between area and methane concentration for merged polygonal ponds is strongest among the three pond types ($R^2_{pred} = 0.21$), the deviation from the regression model increases for small ponds and no clear trend with area is visible. Compared to the linear regression, ice-wedge ponds have higher-than-expected concentrations, while polygonal-center ponds have lower-than-expected concentrations for a given area.

The fraction covered by mosses has no clear influence on surface methane concentrations. For all three pond types, the error on the slope parameter of a linear regression between surface methane con-

centrations and moss cover is far larger than the slope parameter (see Fig. A.9). This indicated that the sign of the regression can not be determined.

A.4 DISCUSSION

The surface methane concentrations measured in this study fall in the range of concentrations measured on Samoylov Island before (Abnizova et al., 2012; Knoblauch et al., 2015). The concentrations in the polygonal tundra of the Lena River Delta are lower than the mean concentration of small ponds in the permafrost-affected parts of Western Siberian Lowlands Polishchuk et al., 2018, 9 µmol L-1. A large fraction of the West Siberian Lowlands is characterized by peatlands and many ponds and lakes formed through thermokarst. Only part of the West Siberian Lowlands is covered by polygonal tundra. A major difference between the two landscapes, which could explain the difference in concentrations, is the water depth of the ponds. The ponds in our study tend to be more than four times deeper (depths of ice-wedge and polygonal-center pond range from 17-117 cm) than ponds of the same area in the Western Siberian Lowlands (Polishchuk et al., 2018). When comparing to the more similar landscape of polygonal tundra in Northern Canada, we find that the concentrations and particularly the differences between the two small pond types match very well Laurion et al., 2009; Negandhi et al., 2013, mean with standard deviation in parenthesis: ice-wedge ponds 4.1(4.7) µmol L-1, polygonal-center ponds 1.3(1.7) µmol L-1. We can thus assume these concentration ranges hold as well for other regions that contain similar pond types, and that the drivers we identify here might apply in other regions, too. We find that the drivers and the distribution of methane concentrations differ between pond types:

ICE-WEDGE PONDS

Surface methane concentrations in ice-wedge ponds can be reasonably well predicted using area, wind speed and bottom concentrations. However, bottom concentrations in turn do not exhibit a correlation to any of the measured variables. This might be due to stratification, which we observe and has also been observed in ice-wedge ponds by Negandhi et al. (2014). We hypothesize that both bottom and surface concentrations depend on the current and past mixing efficiency, which determines the time methane accumulated in the hypolimnion. Because of this accumulation process, the dependency of bottom concentrations on other drivers, like substrate availability, could be masked. This decoupling between methane production and release has been observed by Sachs et al. (2008) in the polygonal tundra of

Samoylov Island. Nevertheless, in Swedish lakes, Juutinen et al. (2009) found that bottom concentrations correlate with nutrient content. We might not capture this dependency in ice-wedge ponds because the organic content in the top sediment might not be representative for the substrate availability in this pond type: Koch et al. (2018) found that especially in newly-formed ice-wedge ponds old carbon leeches into the pond along the edge, which is consistent with results by Negandhi et al. (2013) and Laurion et al. (2009), who find that this pond type emits a larger fraction of old carbon compared to polygonal-center ponds. More of the methanogenesis might be fueled by this leaching of dissolved organic matter, which is a different substrate source than the organic content in the top sediment that was measured in this study. Negandhi et al. (2014) found methane produced from leached organic material to be slightly more abundant in ice-wedge than in polygonal-center ponds. Therefore, the negative dependence of surface methane concentrations in ice-wedge ponds on area could be driven by two mechanisms. First, gas-exchange velocities increase the larger the area of the pond is (Bastviken et al., 2004; Read et al., 2012; Negandhi et al., 2014), and, second, as ice-wedge pond formation is a type of permafrost degradation, the larger the pond, the more advanced is the degradation (Liljedahl et al., 2016). The more degraded the permafrost around the pond is, the less likely is it that labile old permafrost is leached. Reinforcing this, the larger the pond, the smaller the fraction of the pond bottom that is comprised of ice: we found that larger ponds have a deeper than average thaw depth ($p < 0.05$). To sum up, the typical features of ice-wedge ponds tend to be less pronounced the larger the area of an ice-wedge pond, and the ponds become more similar to polygonal-center ponds. The reverse effect can also be observed in Fig. A.7: The smaller the ice-wedge and polygonal center ponds are, the larger is the difference between their methane concentrations.

POLYGONAL-CENTER PONDS

Surface area and water depth of waterbodies regulate diffusive gas transport in a similar manner. The larger or the shallower the pond, the better mixed it is: Larger surface areas promote wind-induced mixing and thus a deeper mixed layer as well as a higher gas exchange velocity (Bastviken et al., 2004; Read et al., 2012). The deeper the pond, the longer the distance the gas has to travel from its source in the sediment to the surface. Though depth and area are often correlated (Wik et al., 2016), in our study, we find that water depth and area are hardly correlated for polygonal-center ponds (Fig. A.6). When comparing their relative importance, water depth has a stronger impact than area on surface methane concentrations in polygonal-center ponds. This is in line with Juutinen et al. (2009) and Wik et al. (2016) who found that

generally for all waterbody types water depth is a better predictor of methane fluxes than area.

Instead of area, water depth in polygonal-center ponds is highly correlated with the overgrown fraction of the ponds in our study — wherever the water is shallow enough, plants tend to take root. Vascular plants also have a strong impact on the carbon cycling in ponds. For example, vascular plants are known to enhance methane emissions by acting as chimneys through which the methane produced at the sediments can bypass the oxidation zone (Kutzbach et al., 2004; Knoblauch et al., 2015). Further, vascular plants are known to increase substrate quality, consequently enhancing methanogenesis in the sediment (Joabsson and Christensen, 2002; Ström et al., 2003). This second effect might be the reason that ponds with the highest overgrown fraction also are likely to contain high organic fraction in the top sediment. Consequently, shallow polygonal-center ponds are mixed better and have a higher substrate availability as they are overgrown to a greater extent. Since we observe that out of the three drivers, which together well explain the variability of surface methane concentrations, two are connected to substrate availability, we conclude that polygonal-center ponds are substrate-limited. Additionally, the strongest driver of the variability between the ponds is due to variations in topography, primarily water depth.

MERGED POLYGONAL PONDS

Compared to the other two pond types, merged polygonal ponds are the largest, the deepest and, consequently, the pond type with least moss cover and the smallest overgrown fraction. A larger surface area increases the gas-exchange velocities, and a vegetation-free pond bottom promotes faster upward mixing into the water column. Therefore, we hypothesize that the coupling between the production of methane in the sediment and surface methane concentrations is strongest in merged polygonal ponds among the pond types. The stratification of ice-wedge and polygonal-center ponds might at least partly mask the influence of environmental variables, like water temperature, on surface methane concentrations. Thus, that methane concentrations in merged polygonal ponds significantly correlate with the largest number of variables might be due to their better-mixed state. The negative correlation of methane surface concentrations with incoming solar radiation and water temperature has been observed before in a study by Burger et al. (2016) but stands in contrast to other studies (Yvon-Durocher et al., 2014; Natchimuthu et al., 2015; Jansen et al., 2020, e.g.), which find that methane concentrations and fluxes increase with increasing temperatures. We cannot conclusively determine the mechanisms responsible for the negative correlation but offer several arguments. Warmer temperatures strengthen both methanogenesis,

which increase surface methane concentrations, and the oxidation of methane in the water column, which decreases methane surface concentrations. Studies come to varying results regarding which of the two processes has a stronger temperature dependency (Duc et al., 2010; Borrel et al., 2011; Lofton et al., 2014; Negandhi et al., 2016). However, in Arctic soils methanogenesis is less temperature-dependent than in warmer regions as the methanogenic communities are adapted to cold temperatures (Tveit et al., 2015). Additionally, the merged polygonal ponds have the lowest overgrown fraction and the lowest fraction of organic content in the top sediment. The temperature dependence of the methanogenesis might also be dampened because of substrate limitation (Lofton et al., 2014; DelSontro et al., 2016), specifically as methanogenesis in the study area is known to depend on substrate quality (Wagner et al., 2003). At the same time, mainly when the ponds are deeper, the water temperature, which was used in the correlation analysis, can be assumed to be more variable than the sediment temperatures, which more directly affect methane concentrations. The methanotrophs benefit before the methanogens, when water warms. Ensuing temperature differences between water surface and sediment might also enhance stratification: Stratification slows down the transport of methane through the water by inhibiting turbulent mixing, and, if there is still oxygen in the water column, additionally enhances oxidation efficiency.

Rather than water temperature, the incoming radiation in the last six hours is more likely the root cause of enhanced stratification, as a measure of how much energy got absorbed by the lake in the last six hours. Supporting this, we find that incoming radiation predicts surface methane concentrations better than the water temperature for predicting surface methane concentrations in merged polygonal pond types together with dissolved oxygen, pond area, organic content in the top sediment and the overgrown fraction. Dissolved oxygen was measured close to the surface making this parameter an indicator of how well the surface layer is mixed and how much oxygen is available for methanotrophs. Both mixing and oxidation decrease methane surface concentrations. Overgrown area can, like for polygonal-center ponds, be seen as a proxy for both the substrate quality and the mean water depth. Especially as the organic content and the overgrown fraction of merged polygonal ponds are smaller than in polygonal-center ponds, we can analogously infer that merged polygonal ponds are substrate-limited and, more than polygonal-center ponds, dependent on those environmental conditions, which influence stratification. Lastly, we note that both stratification and vegetated fraction are at least partly regulated by the topography and mean water depth of the ponds.

DRIVERS OF METHANE VARIABILITY BETWEEN POND TYPES

The three geomorphological pond types have varying drivers of type-internal methane variability, and concurrently, the distributions and mean values of surface methane concentrations of the three pond types differ as well.

Ice-wedge ponds are the most stratified and exhibit other bacterial communities than polygonal-center ponds (Negandhi et al., 2014); merged polygonal ponds are the largest, the best mixed pond type with the highest gas-exchange velocities (Bastviken et al., 2004; Read et al., 2012), and the pond type with the least substrate, the smallest overgrown and moss-covered fraction. Polygonal-center ponds are of the same size than ice-wedge ponds, but for many properties, like dissolved oxygen or thaw depth, fall into the middle of the other two ponds. A reason why the surface methane concentrations of polygonal-center ponds are not as high as would be expected from the log-log regression between methane concentrations and area (see Fig. A.7) might lie with water depth. In polygonal-center ponds, surface methane concentrations strongly depend on water depth, but water depth is not strongly correlated with area. Thus, though polygonal-center ponds have a smaller area than merged polygonal ponds, they might not be shallower.

AREA

As previous studies (DelSontro et al., 2018; Zabelina et al., 2020) suggest, we find that pond area alone is not sufficient to explain variability in methane concentrations. Yet, the observed trend is in agreement with prior studies (Juutinen et al., 2009; Wik et al., 2016), and the relation between pond size and methane concentrations is very similar to the estimate by Polishchuk et al. (2018) — their regression line follows $\log([CH_4]) = -0.258 \cdot \log(\text{area}) + 0.635$. This similarity especially in the slope (our result: -0.2) is astounding since Polishchuk et al. (2018) covered a much larger spatial area, spanning from continuous to sporadic permafrost zones. We conclude that, especially for ponds larger than roughly 10 m^2, an area-based upscaling can be a reasonable choice in permafrost-affected landscapes, but that for smaller ponds additional predictors need to be taken into consideration.

MOSS COVER

Most of the subaquatic soils of the ponds in the study area are at least partly covered by submerged mosses (*Scorpidium scorpioides*). This moss photosynthesises at the bottom of the pond and creates an oxic layer where methane can be oxidised. Additionally, the thick moss captures bubbles and thus suppresses ebullition (Liebner et al., 2011; Knoblauch et al., 2015). Suprisingly, we do not find that moss cover reduces

surface methane concentration on the pond scale (Supplementary Fig. A.9). However, we find that moss does inhibit diffusion, if we look at stratification: Bottom methane concentrations in the moss layer are on average (with standard deviation) 1.8(1.2) times higher than in open water. To reconcile these two findings, we hypothesize that moss cover has a counterbalancing effect: If moss also enhances methanogenesis by providing additional organic substrate similar to what has been shown for vascular plants (Joabsson and Christensen, 2002; Ström et al., 2003), then even though moss leads to enhanced oxidation at the bottom of the pond, the higher productivity might balance out the loss through oxidation. Additionally, the accumulation of methane in the moss layer creates a gradient between moss-covered and moss-free areas in the ponds which are not completely covered by moss. Through lateral mixing part of the methane might escape the moss layer and reach the surface.

The mosses in our study area should not be confused with mosses of the genus *Sphagnum*. Kuhn et al. (2018) found that for sphagnum-dominated ponds diffusive methane fluxes are lower than for ponds with open water, but in contrast to the submerged mosses in our study side, *Sphagnum* stays at the water surface, and thus has a direct impact on the gas exchange at the water-air interface.

CARBON DIOXIDE

All ponds show a positive correlation between surface methane and carbon dioxide concentrations (Fig. A.6). This correlation was expected, since carbon dioxide is produced during acetoclastic methanogenesis, which is assumed to be the most prominent pathway of methanogenesis in cold lakes and ponds (Borrel et al., 2011; Negandhi et al., 2013; Tveit et al., 2015). Additional carbon dioxide is produced during the oxidation of methane, and the oxidation rates have been found to be coupled to methane production rates (Duc et al., 2010). Thus, at least part of the production of carbon dioxide in the pond is closely coupled to methanogenesis. Additionally, the carbon dioxide produced independently of the methane might follow similar drivers.

A.5 CONCLUSIONS

The dominant drivers of methane emissions differ depending on the pond type. We consider substrate availability to be an important driver of methane concentrations markedly in polygonal-center and merged polygonal ponds. Smaller, shallower ponds tend to be richer in substrate (more organic content in the sediment and higher overgrown fraction) and thus exhibit higher concentrations. Accordingly, substrate availability is at least partly determined by the topography of the pond. This finding matches results from prior studies (Juutinen et al., 2009; Sepulveda-Jauregui et al., 2015). The easiest-to-measure topographical

property of ponds is area, and, for merged polygonal ponds, area is a good predictor of methane concentrations. But for polygonal-center ponds, water depth is a far better predictor. Water depth, overgrown fraction (as both a proxy for mean water depth and for substrate availability) and organic fraction in the top sediment are enough to predict surface methane concentrations reasonably well in polygonal-center ponds. In our study, the incoming short-wave radiation over the past six hours was the best proxy for stratification, much improving the statistical model for merged polygonal ponds.

Lastly, ice-wedge ponds are the most distinct pond type. Ice-wedge ponds are strongly stratified as they are narrow, steep and feature a large temperature gradient in summer. If bottom waters are mixed up, surface methane concentrations spike. Additionally, these ponds tend to be richer in substrate and have been shown to emit a larger fraction of old carbon than polygonal-center ponds (Laurion et al., 2009; Negandhi et al., 2013). We find that ice-wedge ponds feature the highest concentrations and, thus, likely also the highest diffusive emissions.

We do not find that the moss-covered fraction of a pond controls methane surface concentrations, as moss might enhance local methanogenesis by providing substrate and lateral mixing might reduce the dampening effect of moss on diffusion.

Climate changes at an above-average rate in the Arctic, and there is growing evidence that global warming will enhance methane emissions from ponds (e.g. Vonk et al., 2015; Tan and Zhuang, 2015; Wik et al., 2016; Aben et al., 2017; Yvon-Durocher et al., 2017), especially so from ice-wedge ponds, which are expected to increasingly form (Liljedahl et al., 2016; Martin et al., 2017). When including small waterbodies in large-scale studies, it is import to choose an appropriate representation for the ponds. As it is not possible to approximate the behaviour of all pond types in our study with the same drivers, let alone use a single driver to approximate the behaviour of all ponds, we conclude that process-based models which ideally capture the different waterbody types will be useful in the improvement of upscaling of pan-Arctic waterbody-methane emissions.

A.6 SUPPLEMENTARY MATERIAL

A.6.1 *SUPPLEMENTARY TEXT*

GAS CHROMATOGRAPHY

A 10mL sample was injected into a sample loop and separated on to the detector by nitrogen as carrier gas. To separate methane and carbon dioxide a PoraPakQ column was used and carbon dioxide was methanized with an nickel catalyst. Before each use the gas

chromatograph was calibrated using three control concentrations per measured gas.

A.6.2 *SUPPLEMENTARY FIGURES AND TABLES*

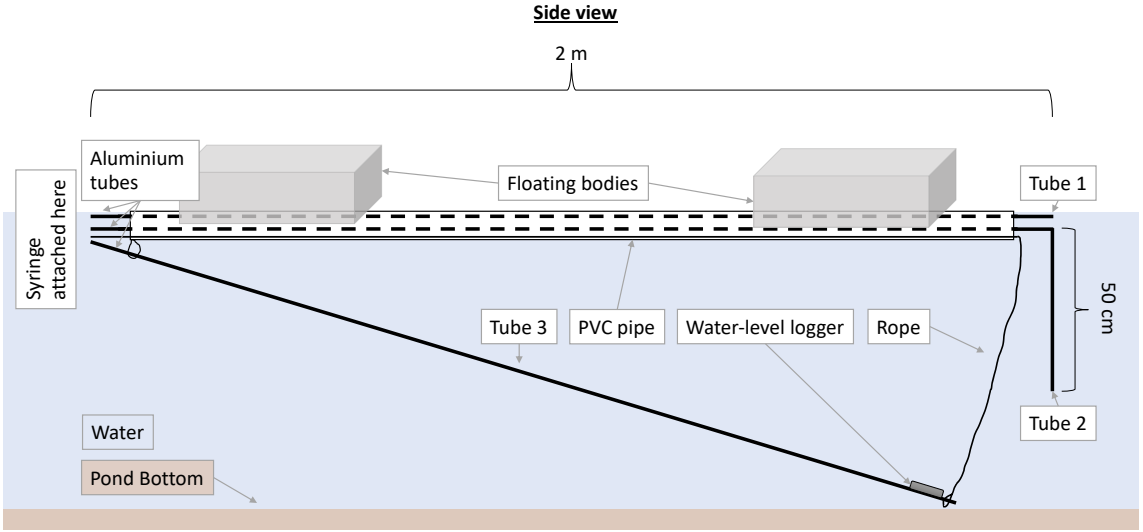

Figure A.8: Sketch of water sampling device. Water samples are taken through three aluminum tubes, which is fixed to a larger 2 m pipe. Two tubes are within the pipe (Tube 1 and 2) and one attached to the outside of the pipe (Tube 3). Tube 1 is used to sample the surface water and is located at 5 cm below the water surface. Tube 2 is used to sample water at 50 cm depth. Tube 3 can be lowered to the bottom of the pond by releasing the rope. A water-level logger Mini-Diver (DI501, Schlumberger Water Services, Netherlands) is attached to the end of this tube, to measure the depth at which the sample was taken. To keep the pipe afloat, two floating bodies are attached.

Table A.2: Quality control of a selection of small and round ponds. Diameter was measured several times along different section over each pond. Using the mean diameter and the assumption that the pond is a perfect circle, the approximated area was computed. The relative difference between approximated area and the area retrieved from the orthophoto map differ between 20% and 2% indicating that both methods provide comparable results.

POND	DIAM. [m]	A (FIELD) [m^2]	A (IMAG.) [m^2]	DIFF. [frac.]
2	8.2	53.0	44.6	-0.19
3	11.3	99.8	93.7	-0.06
13	6.7	34.7	31.1	-0.12
16	13.4	140.3	127.9	-0.10
22	12.4	120.8	117.9	-0.02
27	9.8	74.9	78.1	0.04

Diam, Diameter; A (Field), area measured in the field; A (Imag.), area obtained through orthophotomap; Diff, difference between the areas.

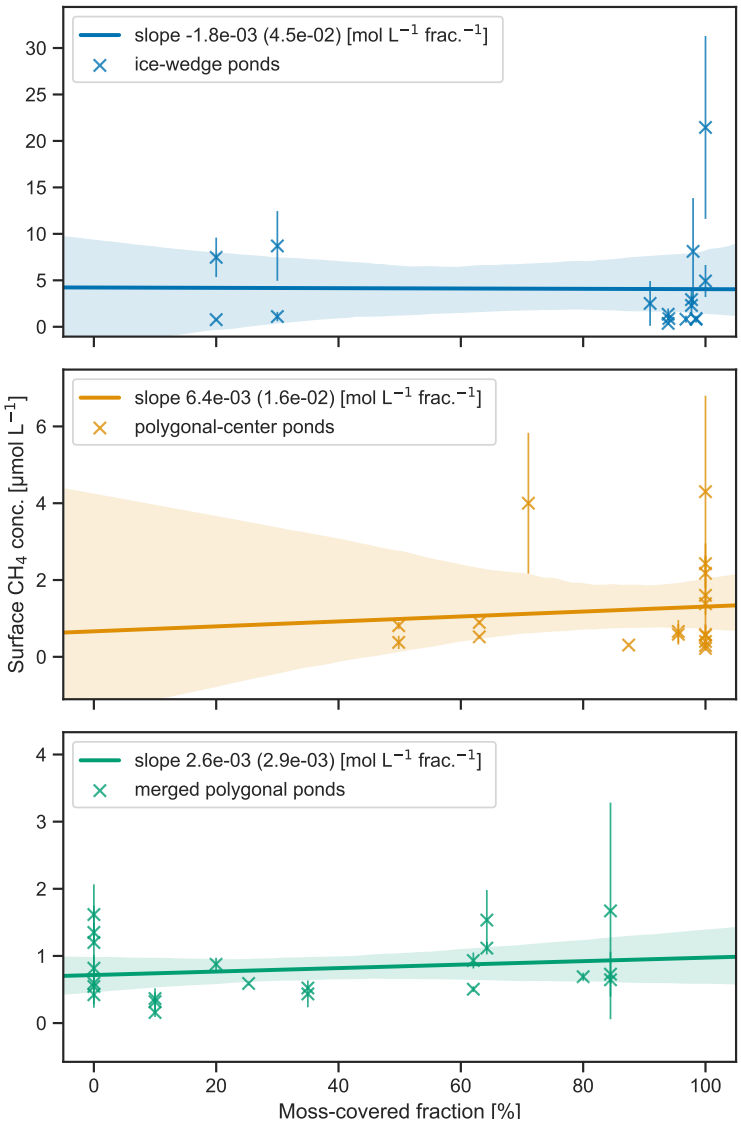

Figure A.9: Methane surface concentrations in each pond type as a function of the moss-covered fraction of each pond. Shaded area indicates the 95% confidence bands.

B

IGNORING CARBON EMISSIONS FROM THERMOKARST PONDS RESULTS IN OVERESTIMATION OF TUNDRA NET CARBON UPTAKE

This manuscript has been accepted for publication in *Biogeosciences*. An earlier version has been published as a preprint:

Beckebanze, L.*, **Rehder, Z.***, Holl, D., Mirbach, C., Wille, C., and Kutzbach, L. (2021). "Small waterbodies reduce the carbon sink of a polygonal tundra landscape". In: *Biogeosciences Discuss.* [preprint]. DOI: 10.5194/bg-2021-212, in review.

* These authors contributed equally to this work.

In this appendix you find the newest, accepted version of the manuscript.

AUTHOR CONTRIBUTIONS

ZR and LK designed the experiments, ZR and LB carried out the fieldwork. ZR, LB, and LK developed the idea for the analysis, and CW and LB prepared the data. The formal analysis and data visualization were performed by LB and ZR with supervision by DH and LK. Resources (land cover classification) have been provided by CM. LB and ZR prepared the manuscript with contributions from all co-authors.

DATA AVAILABILITY

Data will been published at https://doi.pangaea.de/10.1594/PANGAEA.937594 (Beckebanze et al., 2021b) upon publication of the paper.

Ignoring carbon emissions from thermokarst ponds results in overestimation of tundra net carbon uptake

Lutz Beckebanze [1,2,*], **Zoé Rehder** [3,4,*], **David Holl** [1,2], **Christian Wille** [5], **Charlotta Mirbach** [1,2] **and Lars Kutzbach** [1,2]

Received: 09 August 2021 – Discussion started: 12 August 2021 –
Revised: 28 Jan 2022 – Accepted: 29 Jan 2022

[1] Institute of Soil Science, Universität Hamburg, Hamburg, Germany

[2] Center for Earth System Research and Sustainability (CEN), Universität Hamburg, Hamburg, Germany

[3] Max Planck Institute for Meteorology, Hamburg, Germany

[4] International Max Planck Research School on Earth System Modelling, Hamburg, Germany

[5] Helmholtz-Zentrum Potsdam – Deutsches Geo Forschungs Zentrum (GFZ), Potsdam, Germany

[*] These authors contributed equally to this work.

ABSTRACT

Arctic permafrost landscapes have functioned as a global carbon sink for millennia. These landscapes are very heterogeneous, and the omnipresent water bodies within them act as a carbon source. Yet, few studies have focused on the impact of these water bodies on the landscape carbon budget. We deepen our understanding of carbon emissions from thermokarst ponds and constrain their impact by comparing carbon dioxide and methane fluxes from these ponds to fluxes from the surrounding tundra. We use eddy covariance measurements from a tower located at the border between a large pond and semi-terrestrial tundra.

When we take the open-water areas of thermokarst ponds into account, our results show that the estimated summer carbon uptake of the polygonal tundra is 11% lower. Further, the data show that open-water methane emissions are of similar magnitude as polygonal tundra emissions. However, some parts of the pond's shoreline exhibit much higher emissions. This finding underlines the high spatial variability of methane emissions. We conclude that gas fluxes from thermokarst ponds can contribute significantly to the carbon budget of arctic tundra landscapes. Consequently, changes in the water body distribution of tundra landscapes due to permafrost degradation may substantially impact the overall carbon budget of the Arctic.

B.1 INTRODUCTION

Water bodies make up a significant part of the arctic lowlands with an areal coverage of about 17 % (Muster et al., 2017), and act as an important carbon source in a landscape that is an overall carbon sink (Kuhn et al., 2018). Intensified permafrost thaw in the warming Arctic will change the distribution of water bodies, and thereby change their contribution (Andresen and Lougheed, 2015; Bring et al., 2016) to the landscape carbon budget (Kuhn et al., 2018) of tundra landscapes. However, data on greenhouse gas emissions from arctic water bodies are still sparse, especially data with high temporal resolution and from non-Yedoma regions (Vonk et al., 2015).

Our study site in the Lena River Delta, Siberia, is located on an island mostly characterized by non-Yedoma polygonal tundra (Fig. B.1). This landscape features many ponds; we define ponds as water bodies with an area of less than $8 \cdot 10^4$ m^2, following Ramsar Convention Secretariat (2016) and Rehder et al. (2021). Within our area of interest, ponds cover about the same area as lakes (Abnizova et al., 2012; Muster et al., 2012). The ponds on Samoylov Island have formed almost exclusively through thermokarst processes: The soil has a high ice content, so when the ice melts, the ground subsides, and thermokarst ponds form (Ellis et al., 2008). These thermokarst ponds are often only as large as one polygon (polygonal ponds). When several polygons are inundated, this can cause larger shallow thermokarst ponds to form, which we term merged polygonal ponds (Rehder et al., 2021). Holgerson and Raymond (2016) as well as Wik et al. (2016) report that ponds emit more greenhouse gases per unit area than lakes, defined here as water bodies with an area larger than $8 \cdot 10^4$ m^2. Thus, in our study area, they have a greater potential than lakes to counterbalance the carbon uptake of the surrounding tundra (McGuire et al., 2012; Jammet et al., 2017; Kuhn et al., 2018). To better understand the impact of thermokarst ponds on the landscape carbon flux, we compare carbon dioxide (CO_2) and methane (CH_4) fluxes from thermokarst ponds to fluxes from the semi-terrestrial tundra. The semi-terrestrial tundra consists of wet and dry tundra, and overgrown shallow water, which are the terrestrial land-surface types used by Muster et al. (2012) to classify Samoylov Island.

The main geophysical and biochemical processes that drive CH_4 fluxes are different to the ones that drive CO_2 fluxes. The microbial decomposition of dissolved organic carbon, which is introduced laterally into the aquatic system through rain and meltwater (Neff and Asner, 2001), dominates aquatic CO_2 production. When supersaturated with dissolved CO_2, ponds emit CO_2 into the atmosphere through diffusion. While photosynthetic CO_2 uptake has been observed in some clear arctic water bodies (Squires and Lesack, 2003), most arctic water bodies are net CO_2 sources (Kuhn et al., 2018). Estimates of

CO_2 emissions range from close to zero (0.028 g m^2 d^{-1} by Treat et al. (2018), and 0.059 g m^2 d^{-1} by Jammet et al. (2017)) to substantial (1.4–2.2 g m^2 d^{-1} by Abnizova et al. (2012)).

Within just one site, CH_4 emissions from a water body can vary by up to five orders of magnitude: 0.5–6432 mg m^2 d^{-1} (Bouchard et al., 2015). The CH_4 that ponds emit is mostly produced in sub-aquatic soils and anoxic bottom waters (Conrad, 1999; Hedderich and Whitman, 2006; Borrel et al., 2011). Additionally, CH_4 might also be produced in the oxic water column (Bogard et al., 2014; Donis et al., 2017), though this location of methanogenesis is only significant in large water bodies (Günthel et al., 2020). Moreover, there is still ongoing debate as to whether methanogensis occurs in oxic waters at all (Encinas Fernández et al., 2016; Peeters et al., 2019). CO_2 is also formed as a byproduct of the methanogensis process (Hedderich and Whitman, 2006). Water bodies emit CH_4 produced in their benthic zone through diffusion, ebullition (sudden release of bubbles), or plant-mediated transport. The varying contributions of these three local methane emissions pathways lead to high spatial variability between water bodies and within a single water body (Sepulveda-Jauregui et al., 2015; Jansen et al., 2019). In particular, local seep ebullition causes high spatial variance of CH_4 emissions within one water body (Walter et al., 2006). Variability in the coverage and composition of vascular plant communities in a water body can also increase CH_4 variability because CH_4 transport efficiency can be species-specific (Knoblauch et al., 2015; Andresen et al., 2016).

To study spatial and temporal patterns of carbon emissions from thermokarst ponds, we analyzed land-atmosphere CO_2 and CH_4 flux observations from an eddy covariance (EC) tower on Samoylov Island, Lena River Delta, Russia. We set up the EC tower within the polygonal tundra landscape at the border between a large merged polygonal pond and the surrounding semi-terrestrial tundra for two months in summer 2019. The polygonal structures were still clearly visible along the shore and underwater, and most of the pond was shallow (Rehder et al., 2021). Due to the tower's position, fluxes from the merged polygonal pond were the dominant source of the observed EC fluxes under easterly winds. From other wind directions, the observed EC fluxes were dominated by semi-terrestrial polygonal tundra with only a low influence from small polygonal ponds. This paper aims to deepen the understanding of carbon emissions from thermokarst ponds and constrain their impact on the landscape carbon balance. We (1) examine the temporal and spatial patterns of NEE and the spatial pattern of CH_4 flux from semi-terrestrial tundra and thermokarst ponds, and (2) investigate the influence of the thermokarst ponds on the landscape NEE of CO_2 during the months June to September 2019. To this end, we use a footprint model and model net ecosystem

exchange (NEE) of CO_2 using the footprint weights of semi-terrestrial tundra and thermokarst ponds.

B.2 METHODS

B.2.1 *STUDY SITE*

Samoylov Island (72°22'N, 126°28'E) is located in the southern part of the Lena River Delta (Fig. B.1, b). It is approximately five km^2 large and consists of two geomorphologically different components. The western part of the island (~2 km^2) is a floodplain, which is flooded annually during the spring. The eastern part of the island (~3 km^2), a late-Holocene river terrace, is characterized by polygonal tundra. The partially degraded polygonal tundra at this study site features high spatial heterogeneity on a scale of a few meters in several aspects, including vegetation, water table height, and soil properties. Dry and wet vegetated parts of the semi-terrestrial tundra are interspersed with small and large thermokarst ponds (1–10,000 m^2) and with larger lakes (up to 0.05 km^2, Boike et al. (2015a) and Kartoziia (2019)). The island is surrounded by the Lena River and sandy floodplains, creating additional spatial heterogeneity on a larger scale.

This study focuses on a merged polygonal pond (Fig. B.1, d, and B.7) on the eastern part of the island. This merged polygonal pond has a size of 0.024 km^2 with a maximum depth of 3.4 meters and a mean depth of 1.2 meters (Rehder et al., 2021; Boike et al., 2015a). In an aerial image of the pond, the polygonal structures are clearly visible under the water's surface (Boike et al., 2015c). The vegetated shoreline of this merged polygonal pond is dominated by *Carex aquatilis*, but it also features *Carex chordorrhiza*, *Potentilla palustris*, and *Aulacomnium spp.*. These plants grow in the water near the shore while the deeper parts of the merged polygonal pond are vegetation-free.

B.2.2 *INSTRUMENTS*

We measured gas fluxes using an eddy covariance (EC) tower between July 11 and September 10, 2019. The EC tower was located on the eastern part of Samoylov Island, directly at the western shore of the merged polygonal pond (Fig. B.1, d). The EC instruments were mounted on a tripod at a height of 2.25 meters (Fig. B.7). The tower was equipped with an enclosed-path CO_2/H_2O sensor (LI-7200, LI-COR Biosciences, USA), an open-path CH_4 sensor (LI-7700, LI-COR Biosciences, USA), and a 3D-ultrasonic anemometer (R3-50, Gill Instruments Limited, UK). All instruments had a sampling rate of 20 Hz. We also installed radiation-shielded temperature and humidity sensors at the EC tower (HMP 155, Vaisala, Finland) and used data from a photosynthetically active radiation (PAR) sensor mounted on a

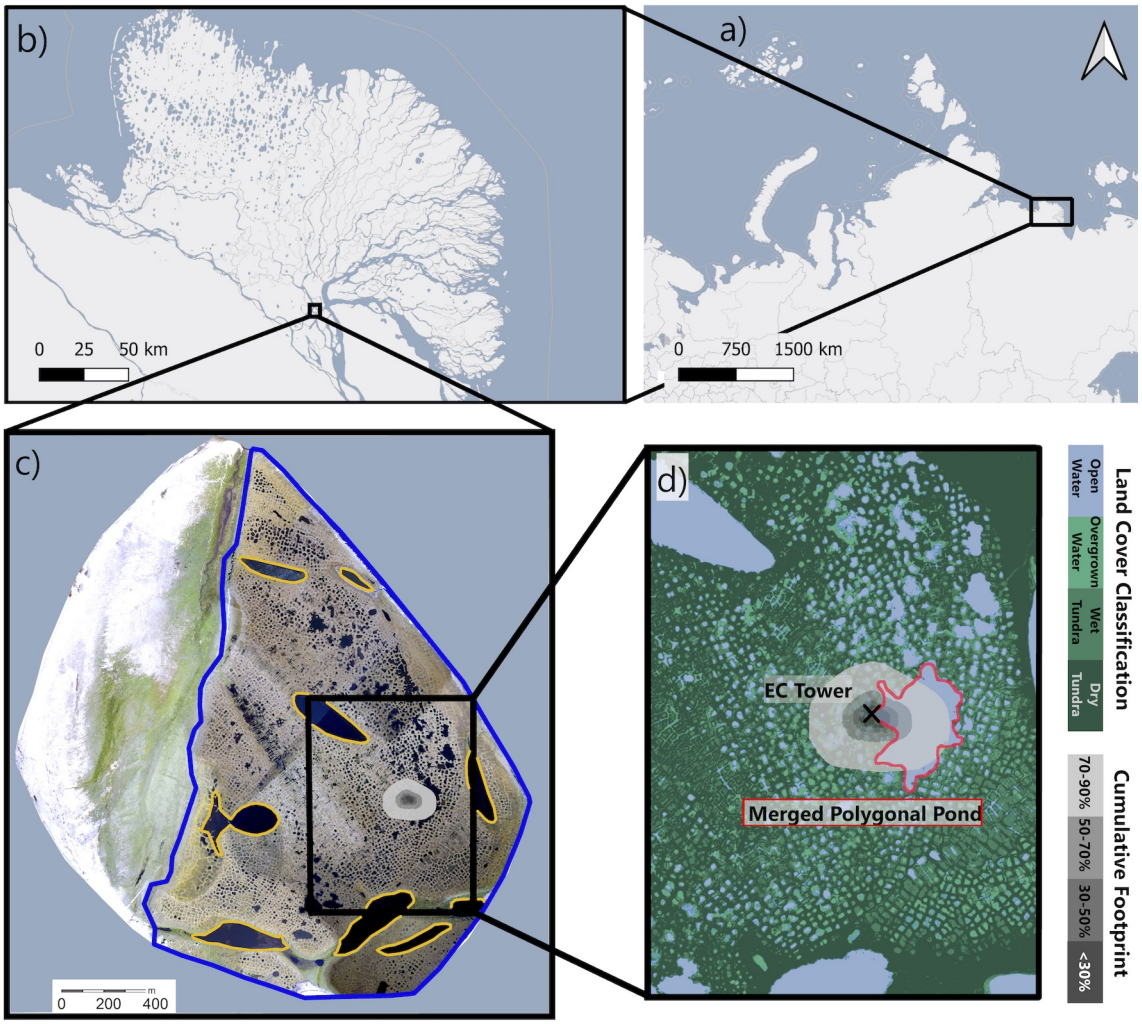

Figure B.1: The location of the study site in Russia is shown in (a) and the location of Samoylov Island within the Lena River Delta is shown in (b). Samoylov Island is shown in (c); the surrounding Lena River appears in light blue. The outline of the river-terrace land-cover classification (Sect. B.2.4.1) is indicated by the blue line. We focus on the polygonal tundra, however, large lakes are excluded (circled in yellow). In (d), the land-cover classification is drawn in blue (open water) and green shades (dark green: dry tundra; medium green: wet tundra; and light green: overgrown water). The merged polygonal pond studied here is outlined in red. The location of the EC tower is marked by a black cross. The cumulative footprint (see Sect. B.2.4.2) is shown in gray shades. 30 % of the flux likely originated from within the dark gray area, 50 % from within the medium-dark gray area, 70 % from within the medium-light gray area and 90 % from within the light gray area. Map data from © OpenStreetMap contributors 2020, distributed under the Open Data Commons Open Database License (ODbL) v1.0 (a & b) and modified based on Boike et al. (2012) (c & d).

tower approximately 500 meters to the west of the EC tower (SKP 215, Skye Instruments, UK). Additional meteorological data for Samoylov Island was provided by Boike et al. (2019).

B.2.3 *DATA PROCESSING*

We performed the raw data processing and computation of half-hourly fluxes for open-path and enclosed-path fluxes (CO_2, CH_4 and H_2O) using *EddyPro 7.0.6* (LI-COR, 2019). The convention of this software is that positive fluxes are fluxes from the surface to the atmosphere, while negative fluxes indicate a flux from the atmosphere downwards. Raw data screening included spike detection and removal according to Vickers and Mahrt (1997) (1 % maximum accepted spikes and a maximum of three consecutive outliners). Additionally, we applied statistical tests for raw data screening, including tests for amplitude resolution, skewness and kurtosis, discontinuities, angle of attack, and horizontal winds steadiness. All of these tests' parameters were set to *EddyPro* default values. We rotated the wind-speed axis to a zero-mean vertical wind speed using Kaimal and Finnigan's (1994) "double rotation" method. Further, we applied linear de-trending to the raw data following Gash and Culf (1996) before performing flux calculations. We compensated time lags via automatic time lag optimization using a time lag assessment file from a previous EddyPro run. In this previous time lag assessment, the time lags for all gases were detected using covariance maximization (Fan et al., 1990), resulting in time lags between 0–0.4 s for CO_2 and -0.5–+0.5 s for CH_4. For H_2O, the time lag was humidity-dependent and was calculated for 10 humidity classes. We compensated for air-density fluctuations due to thermal expansion and contraction and varying water-vapor concentrations, following Webb et al. (1980). This correction depends on accurate measurements of the latent and sensible heat flux and was applied to the open-path data of the LI-7700. For the LI-7700 in particular, the correction term can be larger than the flux itself, but the correction was derived from the underlying physical equations. Because we used well-calibrated instruments as well as *EddyPro*, which uses an up-to-date implementation of the correction, we were confident that the LI-7700 would provide accurate CH_4 flux estimates. For enclosed-path data, we performed a sample-by-sample conversion into mixing ratios to account for air density fluctuations (Ibrom et al., 2007b; Burba et al., 2011). Flux losses occurred in the low- and high frequency spectral range due to different filtering effects. We compensated flux losses in the low-frequeny range in accordance with Moncrieff et al. (2004) and in the high-frequency range in accordance with Fratini et al. (2012). For the high-frequency range compensation method, a spectral assessment file was created using Ibrom et al.'s (2007) method. The spectral assessment resulted in cut-off frequencies

of 3.05 Hz and 1.67 Hz for CO_2 and CH_4, respectively. For H_2O, we found a humidity-dependent cut-off frequency between 1.25 Hz (RH 5–45 %) and 0.21 Hz (RH 75–95%). We performed a quality check on each half-hourly flux following the 0-1-2 system proposed by Mauder and Foken (2004). In this quality check, flux intervals with the lowest quality received the flag "2" and were excluded from further analysis.

B.2.4 *DATA ANALYSIS*

B.2.4.1 LAND-COVER CLASSIFICATION

The land-cover classification covers the late-Holocene river terrace of Samoylov Island (3.0 km^2, area within the blue line in Fig. B.1, c). It is based on high-resolution near-infrared (NIR) orthomosaic aerial imagery obtained in the summer of 2008 (Boike et al., 2015b). We used a subset of Muster et al.'s (2012) existing classification as a training dataset to perform a semi-supervised land-cover classification using the *maximum likelihood algorithm* in ArcMap Version 10.8 (ESRI Inc, USA). We then applied the ArcMap *majority filter* tool to the new classification. The land-cover classification has a resolution of 0.17 m x 0.17 m,. It is projected onto WGS 1984 UTM Zone 52N and the land-cover classes include *open water* (15.7 %), *overgrown water* (7.0 %), *dry tundra* (65.1 %), and *wet tundra* (12.1 %), as defined by Muster et al. (2012). We summarize the classes *overgrown water*, *dry tundra*, and *wet tundra* in the land-cover type, semi-terrestrial tundra. The river terrace consists of this semi-terrestrial tundra, large lakes, and thermokarst ponds. Since small ponds are an integral part of the polygonal tundra, we use the term "polygonal tundra" to refer to the area of the river terrace covered by semi-terrestrial tundra and by thermokarst ponds.

B.2.4.2 FOOTPRINT MODEL

In deploying an EC measurement tower, the tower's location and sensor height are crucial parameters. A lower measurement height results in a smaller footprint. The tower's footprint describes the source area of the flux within the surrounding landscape. As we installed sensors at a height of 2.25 m next to the merged polygonal pond, we expected to observe substantial flux signals from the adjacent water body as well as from the surrounding semi-terrestrial tundra. Each land-cover type's contribution to the flux signal depended on the wind direction and turbulence characteristics. We implemented the analytical footprint model proposed by Kormann and Meixner (2001) in Matlab 2019b (MATLAB, 2019). We combined the footprint model with land-cover classification data described in Sect. B.2.4.1 to estimate the contribution of each land-cover type to each half-hourly flux (from now on referred to as the weighted footprint fraction). The model accounted for the stratification of the atmospheric boundary layer and

required a height-independent crosswind distribution and horizontal homogeneity of the surface. The input data required stationarity of atmospheric conditions during the flux intervals of 30 minutes.

We derived the vertical power-law profiles for the eddy diffusivity and the wind speed for each 30-minute flux depending on the atmospheric stratification (see Eq. 6 in Kormann and Meixner (2001)). We used an analytical approach to find the closest Monin-Obukhov (M-O) similarity profile (see Eq. 36 in Kormann and Meixner (2001)). Next, we calculated a two-dimensional probability density function of the source area for each flux (from Eq. 9 and 21 in Kormann and Meixner (2001)). We combined each probability density function with the land-cover classification of Samoylov Island's river terrace with its four land-cover types (see Sect. B.2.4.1). The resolution of the footprint model was set to the land-cover classification resolution of 0.17 m x 0.17 m. Hence, we were able to estimate how much a given grid cell contributed to each 30-min flux. We also knew each grid cell's dominant land-cover type from the land-cover classification. We combined both pieces of information for each grid cell and calculated the sum of the fraction fluxes within the source area for each of the four land-cover types (*dry tundra*, *wet tundra*, *overgrown water*, and *open water*) and determined the contribution of each land-cover type in respect of each 30-minute flux ($a_{dry\ tundra}$, $a_{wet\ tundra}$, $a_{overgrown\ water}$, and $a_{open\ water}$). We refer to this contribution of each land-cover type as the *weighted footprint fraction*.

We also summed all 30-min two-dimensional probability density functions over the entire deployment time. This sum is referred to as the cumulative footprint (gray shaded area in Fig. B.1, c–d).

B.2.4.3 GAP-FILLING THE CO_2 FLUX

To gap-fill the net-ecosystem exchange (NEE) fluxes of CO_2, we used the *bulk-NEE model* proposed by Runkle et al. (2013). The model is specifically designed to model NEE in arctic regions: It takes impacts of the polar day into account by allowing both respiration and photosynthesis to occur simultaneously throughout the day. The *bulk-NEE model* uses the sum of total ecosystem respiration (TER) and gross primary production (GPP) to describe NEE, our target variable:

$$NEE = TER + GPP \tag{B.1}$$

where TER and GPP have the unit µmol m^{-2} s^{-1}. TER is approximated as an exponential function of air temperature T_{air}:

$$TER = R_{base} \cdot Q_{10}^{\frac{T_{air} - T_{ref}}{\gamma}} \tag{B.2}$$

where $T_{ref} = 15$ °C and $\gamma = 10$ °C are constant, independent parameters. R_{base} (µmol m^{-2} s^{-1}) describes the basal respiration at the reference temperature T_{ref} and Q_{10} (dimensionless) describes the

sensitivity of ecosystem respiration to air temperature changes.
GPP is described as a rectangular hyperbolic function of PAR (µmol m^{-2} s^{-1}):

$$GPP = -\frac{P_{max} \cdot \alpha \cdot PAR}{P_{max} + \alpha \cdot PAR} \tag{B.3}$$

where α (µmol µmol^{-1}) is the initial canopy quantum use efficiency (slope of the fitted curve at PAR= 0) and P_{max} (µmol m^{-2} s^{-1}) is the maximum canopy photosynthetic potential for PAR $\rightarrow \infty$.
The parameters R_{base}, Q_{10}, P_{max}, and α were fitted simultaneously. To account for seasonal changes in plant physiology, we fitted the parameters for running five-day windows as proposed in Holl et al. (2019a).
We split the datasets into training (70 %) and validation (30 %) data sets to test model performance. We implemented the *bulk-NEE model* in Matlab 2019b (MATLAB, 2019) using the *fit* function with the *NonLinearLeastSquares* fitting method. We used the *coeffvalues*-function to estimate the four parameters (R_{base}, Q_{10}, P_{max}, and α) and the *confint*-function to estimate their 95 % confidence bounds. All partitioned fluxes were converted into CO_2-C fluxes in the unit g m^{-2} d^{-1} before data analysis.

B.2.4.4 SEPARATING CO_2 FLUXES FROM SEMI-TERRESTRIAL TUNDRA AND WATER BODIES

We wanted to extract fluxes from thermokarst ponds and semi-terrestrial tundra to analyze the influence of thermokarst ponds on the carbon balance of a polygonal tundra landscape. However, due to the strong heterogeneity of the landscape and the relatively small size of the merged polygonal pond compared to the EC footprint, we measured a mixed signal from all wind directions. In other words, each flux that was measured with the EC method contained information from different land-cover types. We divided the footprint into two classes – semi-terrestrial tundra and thermokarst ponds – to assess the impact of thermokarst ponds on the carbon balance.

Similar approaches of analyzing heterogeneous eddy covariance fluxes in arctic environments have been conducted for CO_2 and CH_4 (e.g. Rößger et al., 2019a,b; Tuovinen et al., 2019). Rößger et al. (2019a,b) extracted CO_2 and CH_4 fluxes from two different land-cover classes on a floodplain, while Tuovinen et al. (2019) separated CH_4 fluxes from nine individual land-cover classes, including water, and combined them into four source classes (with no separate class for water). All three studies differentiate between fluxes from different vegetation types. Our method is dedicated to distinguishing between fluxes from semi-terrestrial tundra and water bodies.

To estimate CO_2 fluxes from the merged polygonal pond (F_{pond}), we first fitted the *bulk-NEE model* to training data, excluding fluxes

from the direction of the merged polygonal pond (30° < WD < 150°). We obtained a dataset consisting of information about as much semi-terrestrial tundra as possible. We performed this step since we expected little to no photosynthetic activity in the open-water part of the merged polygonal pond. This gap-filled CO_2 flux (hereinafter $F_{modeled,mix}$) represents the polygonal tundra surrounding the EC tower, meaning the flux is dominated by semi-terrestrial tundra, but also includes polygonal ponds from wind directions of north, west, and south. In the model input, we excluded 30-minute CO_2 fluxes with an absolute value of more than 4 g m^{-2} d^{-1}. In 38 five-day windows, we found an R^2 above 0.9 between the model output and the validation set. In 18 cases, we obtained an R^2 between 0.8–0.9; in six instances, we obtained an R^2 below 0.7. The final RMSE between the model input and the gap-filled NEE had a value of 0.29 g m^{-2} d^{-1}.

We assumed that the total observed flux was a linear combination of the fluxes from the land-cover types weighted by their respective contribution to the footprint. Thus, we postulated that the observed CO_2 flux ($F_{obs,mix}$, not gap-filled) was the sum of the individual land-cover type fluxes ($F_{modeled,mix}$ and the merged polygonal pond F_{pond}) each multiplied with their weighted footprint fraction (a_{mix} and a_{pond}), with $a_{open\ water} = a_{pond}$, $a_{mix} = a_{sum} - a_{pond}$, and a_{sum} being the sum over all land-cover classes:

$$\begin{aligned} F_{obs,mix} &= a_{pond} \cdot F_{pond} + a_{mix} \cdot F_{modeled,mix} \\ \Leftrightarrow\ F_{pond} &= \frac{F_{obs,mix} - a_{mix} \cdot F_{modeled,mix}}{a_{pond}} \end{aligned} \tag{B.4}$$

To improve data quality, we excluded 30-min fluxes of F_{pond} when $a_{pond} < 50$ %. Then, we used the median of F_{pond} for further calculations, and we assumed that all thermokarst ponds in the EC footprint emitted the same amount of CO_2.

As mentioned above, the observed CO_2 flux from the wind direction of north, west, and south ($F_{obs,mix}$) was influenced by polygonal ponds to a small degree. Since our aim was to assess the impact of thermokarst ponds (both polygonal ponds and merged polygonal ponds) on NEE, we needed to eliminate the influence of polygonal ponds from our NEE estimate. To extract uncontaminated CO_2 flux data from the semi-terrestrial tundra ($F_{modeled,tundra}$), we subtracted the previously estimated pond CO_2 flux F_{pond} from the observed CO_2 flux $F_{obs,mix}$:

$$F_{modeled,tundra} = \frac{F_{obs,mix} - a_{pond} \cdot F_{pond}}{a_{mix}} \tag{B.5}$$

We then used this estimated CO_2 flux from the semi-terrestrial tundra $F_{modeled,tundra}$ as the regressand variable for the *bulk-NEE model* to obtain a gap-filled dataset regarding CO_2 flux from the semi-terrestrial tundra. This gap-filling modeling of CO_2-C flux had an RSME of 0.31 g m^{-2} d^{-1}.

To evaluate the impact of thermokarst ponds on landscape CO_2 flux, we estimated a polygonal tundra landscape-CO_2 flux from the late-Holocene river terrace of Samoylov Island ($F_{landscape}$) by combining thermokarst ponds and semi-terrestrial tundra linearly:

$$F_{landscape} = A_{pond} \cdot F_{pond} + A_{tundra} \cdot F_{modeled,tundra}$$

where F_{pond} describes the CO_2 emissions from the open-water areas of thermokarst ponds (Eq. B.4), $F_{modeled,tundra}$ describes the modeled CO_2 flux from the semi-terrestrial tundra (Eq. B.5), $A_{pond} = 0.07$ is the fraction of the river terrace area of Samoylov Island that is covered by thermokarst ponds (from the land-cover classification, see Sect. B.2.4.1) and $A_{tundra} = 1 - 0.07$ is the fraction of other land-cover to the entire river terrace area. We did not account for larger or deeper lakes in this up-scaling approach, as we expected different greenhouse gas emission dynamics from these lakes and there were no lakes in our footprint, and therefore not within our observation range. Thus, we scaled the above numbers to $A_{tundra} + A_{pond} = 1$, which results in $A_{pond} = 0.076$ and $A_{tundra} = 0.924$.

B.2.4.5 CH_4 FLUX PARTITIONING

The data show that the CH_4 emissions from the heterogeneous landscape around the tower were less spatially uniform than the CO_2 emissions. Therefore, we could not use a gap-filling model for CH_4 that was similar to the bulk model we used for CO_2, so we investigated CH_4 emissions in a different way. Based on preliminary results from our analysis and the aerial image of the study site, we focused on four wind sectors instead of extracting the fluxes from the land-cover types:

- *tundra*: At least half of the footprint consisted of dry tundra, and the wind direction was larger than 170°.
- *shore*$_{50°}$: Less than 40% of the footprint consisted of dry tundra and water comprised least 30% of the footprint. The wind direction was between 30° < WD < 65°.
- *pond*: At least half of the footprint consisted of open water, and the wind direction was between 65° < WD < 110°.
- *shore*$_{120°}$: Less than 40% of the footprint consisted of dry tundra and water comprised at least 30% of the footprint. The wind direction was between 110° < WD < 130°.

B.2.4.6 CH_4 PERMUTATION TEST

To evaluate whether the differences in flux medians between the four wind sectors were significant, we applied a permutation test (Edgington and Onghena, 2007). In this test, we randomly assigned each

30-min flux to one of two groups and calculated both groups' median and the differences between the group's medians. We conducted six tests in total, using all possible combinations of pairs with the four wind sectors. After repeating this step 10000 times, we plotted the resulting differences in medians in a histogram and performed a one-sample t-test to evaluate whether the observed difference in medians differed significantly ($p < 0.01$) from the randomly generated differences.

B.3 RESULTS

B.3.1 *METEOROLOGICAL CONDITIONS*

During the measurement period between July 11 and September 10, 2019, half-hourly air temperatures range from -0.5 °C to 27.6 °C with a mean temperature of 8.7 °C (Fig. B.8, a). The maximum wind speed measured at the EC tower at a height of 2.25 m is 8.9 m s^{-1} (Fig. B.8, b). PAR reaches values of up to 1419 µmol m^{-2} s^{-1} with decreasing maximum values during the measurement period (Fig. B.8, c). Throughout the measurement period, there are 28 cloudy days, determined by identifying days with low PAR-values (maximum values below ~500 µmol m^{-2} s^{-1}).

B.3.2 *CO_2 FLUXES*

When inspecting the relation between observed CO_2 fluxes and wind direction (Fig. B.2), we find that CO_2 fluxes exhibit high temporal variability between positive and negative CO_2 fluxes from most wind directions. In the wind sector between 60°–120°, the flux source area is dominated by the merged polygonal pond. The CO_2-C fluxes from this pond sector show smaller absolute variability (0.09 $^{0.38}_{-0.33}$ g m^{-2} d^{-1}, Median $^{95\,\%\text{ Percentile}}_{5\,\%\text{ Percentile}}$) than the fluxes from all other wind directions (−0.08 $^{0.87}_{-1.56}$ g m^{-2} d^{-1}, Median $^{95\,\%\text{ Percentile}}_{5\,\%\text{ Percentile}}$). Additionally, we observe a lower respiration rate from the merged polygonal pond than from the semi-terrestrial tundra. Fig. B.3 shows the observed nighttime CO_2 fluxes plotted against the respective weighted footprint fraction of open water. We define nighttime as PAR<20 µmol m^{-2} s^{-1}; we expect that there would only be respiration, no photosynthesis, during the night-times. We find that the fluxes decrease as the pond area contribution increases. Thus, the strength of CO_2 respiration shows a dependence on the contribution of open-water. We also find that low air temperatures are mostly associated with low respiration rates.

Another aspect of CO_2 flux variability stems from the diurnal cycle. We compare the diurnal cycle of the CO_2 fluxes from the merged

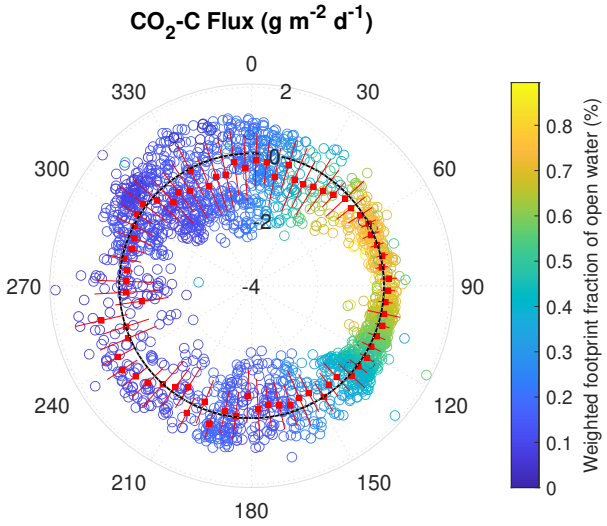

Figure B.2: Polar plot of observed 30-minute CO_2-C fluxes with respect to the wind direction. Negative values (inside of the solid black line) represent CO_2 uptake, while positive values (outside of the dotted black line) represent CO_2 emissions. The values -4, -2, 0, and 2 indicate the magnitude of the CO_2-C flux in g m^{-2} d^{-1}. The color of each point on the plot represents the percentage the point comprises of the total open water weighted footprint fraction in each 30-minute flux. The red boxes indicate the mean CO_2 flux of 5° wind direction intervals during the two-month observation period (red lines indicate the first standard deviation).

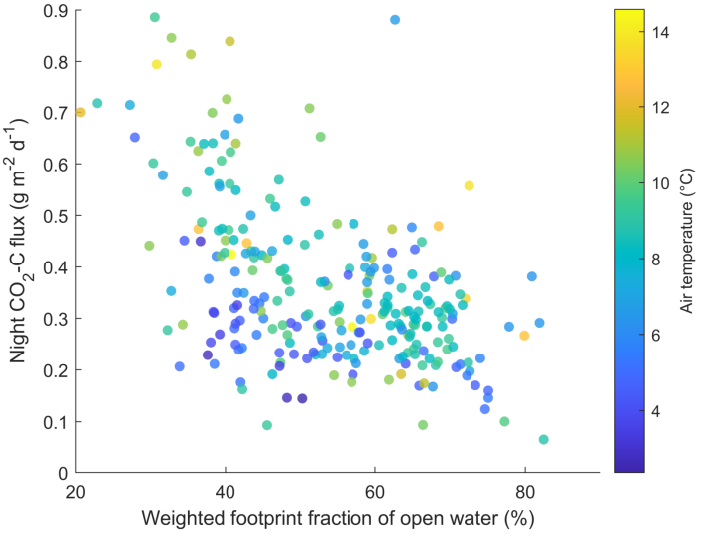

Figure B.3: Scatter plot of observed CO_2 fluxes against the weighted footprint fraction of open water during each 30-minute flux. The air temperature is represented through color. Only fluxes observed at nighttime (PAR<20 µmol m^{-2} s^{-1}) are shown.

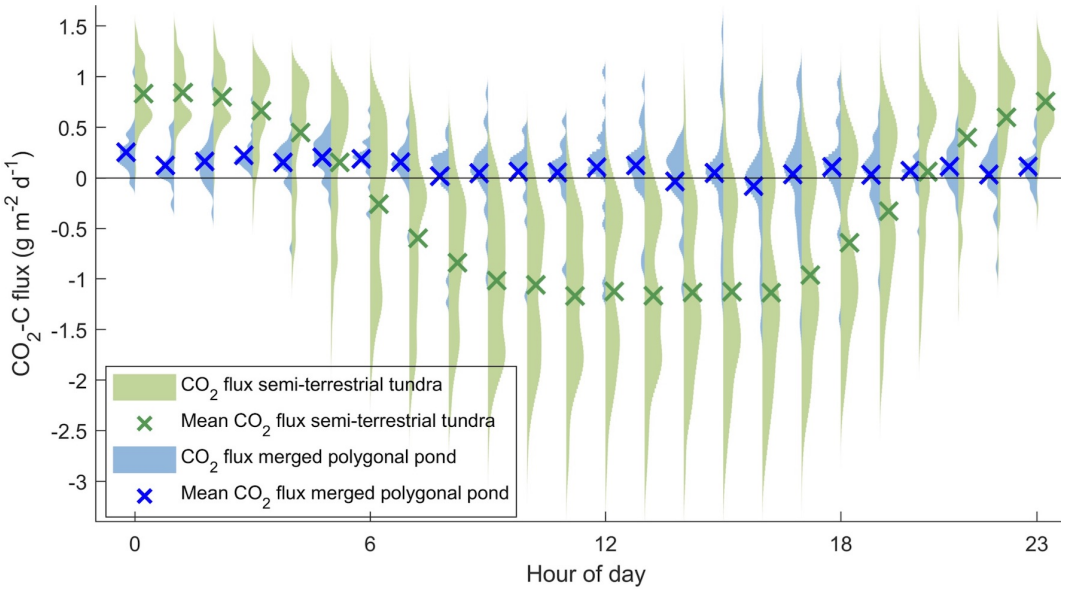

Figure B.4: Diurnal cycle of modeled CO_2-C based on observations flux from the merged polygonal pond (blue, eq. B.4) and the semi-terrestrial tundra (green, eq. B.5) as violin plots for each half-hour flux. Blue and green crosses mark the mean CO_2-C flux during each half-hour flux. A violin plot shows the distribution of measurements along the y-axis – the width of the curves indicates how frequently a certain y-value occurred.

polygonal pond (estimated in accordance with Eq. B.4) and the semi-terrestrial tundra (Eq. B.5, Fig. B.4). The results show a less pronounced diurnal CO_2 cycle from the direction of the merged polygonal pond (blue) compared to the diurnal CO_2 cycle from the semi-terrestrial tundra (green). We combine all data from the merged polygonal pond (F_{pond} in Eq. B.4), which results in a CO_2-C flux of $0.13\ ^{0.24}_{0.00}$ g m^{-2} d^{-1} (Median $^{75\ \%\ \text{Percentile}}_{25\ \%\ \text{Percentile}}$).

B.3.3 CH_4 FLUXES

We plot the observed CH_4 fluxes against wind direction (Fig. B.5). The results show that the CH_4 emissions peak at ~ 120°, where fluxes from one shoreline of the merged polygonal pond contribute to the observed flux (Fig. B.1 d, from now on $shore_{120°}$). We do not observe a similar peak of CH_4 emissions in the direction of the second shoreline towards ~ 50° ($shore_{50°}$). These peaks did not correlate with a specifically large contribution of one of the land-cover classes to the footprint.

To further investigate the peak at $shore_{120°}$, we compare the CH_4 emissions from the different wind sectors ($shore_{120°}$, $shore_{50°}$, *pond* and *tundra*, Sect. B.2.4.5). We find the following fluxes from the wind sectors: $19.18\ ^{24.47}_{14.26}$ mg m^{-2} d^{-1} ($shore_{120°}$), $12.96\ ^{15.11}_{10.34}$ mg m^{-2} d^{-1} ($shore_{50°}$), $13.90\ ^{18.46}_{11.02}$ mg m^{-2} d^{-1} (*pond*), and $12.55\ ^{16.07}_{9.65}$ mg m^{-2}

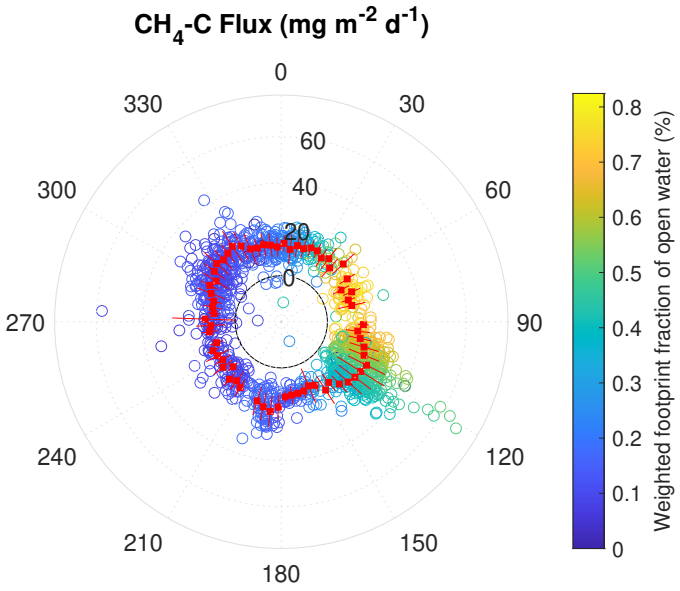

Figure B.5: Polar plot of 30-minute observed CH_4-C flux with respect to the wind direction at the EC tower. Positive values outside the solid black line represent CH_4 emissions, while values and inside the line represent CH_4 uptake during one half-hour period. The values 0, 20, 40, and 60 indicate the magnitude of the CH_4-C flux in mg m^{-2} d^{-1}. The color of each point on the plot represents the percentage the point comprises of the total open water weighted footprint fraction in each 30-minute flux. The red boxes indicate the mean CH_4 flux of 5° wind direction intervals during the two-months observation period (red lines indicate the first standard deviation).

d^{-1} (*tundra*, Median $^{75\ \%\ \text{Percentile}}_{25\ \%\ \text{Percentile}}$). Fluxes from $shore_{120°}$ have a higher median than fluxes from the other three wind sectors (Fig. B.6).

We investigated the impact of wind speed and air temperature on the CH_4 fluxes by excluding flux intervals with high wind speed (greater than 5 m s^{-1}) and high air temperature (warmer than 12 °C). The randomization test (Sect. B.2.4.6) provided evidence of a significant difference between CH_4 emissions from $shore_{120°}$ and the other three wind sector classes at low wind speeds (top row in Fig. B.10) and no significant difference between the CH_4 emission from the classes *pond* - *tundra* and $shore_{50°}$ - *tundra*. The difference between the classes *pond* and $shore_{50°}$ is significant; however, it is much smaller than the previously described differences (see center graph in Fig. B.10). Note that the CH_4 emissions from *pond* and *tundra* have a similar magnitude under moderate wind speed conditions. The results are very similar for moderate temperatures: We find evidence of a significant difference between the CH_4 emissions from $shore_{120°}$ and the CH_4 emissions from the other three wind sector classes (top row in Fig. B.11). The differences in medians between the *pond* and $shore_{50°}$ and between the *pond* and *tundra* are significant. However, this difference

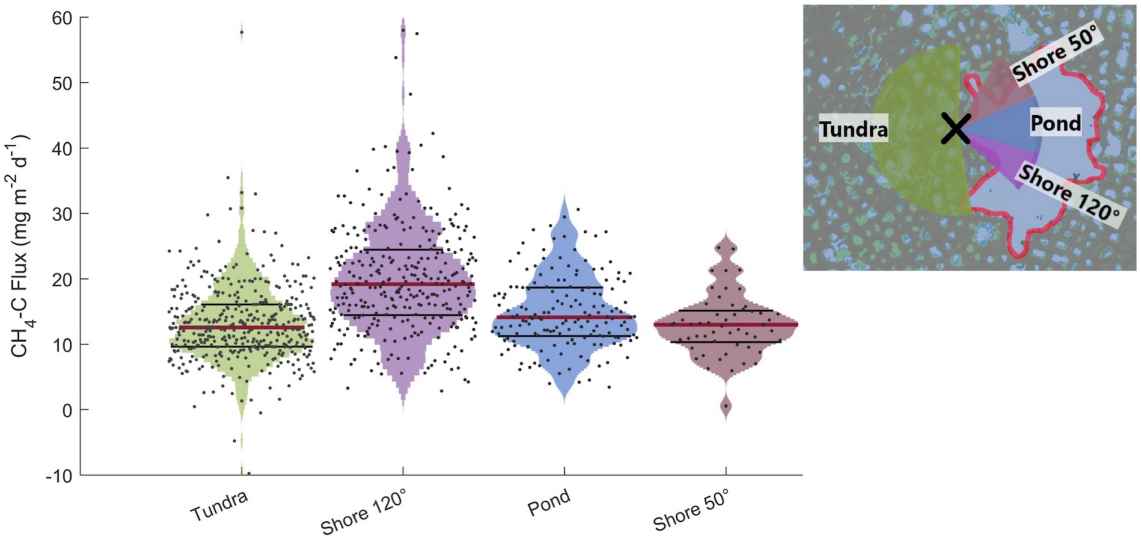

Figure B.6: Violin plots of observed CH_4 emissions at the EC tower separated into four different wind sector classes. A violin plot shows the distribution of measurements along the y-axis - the width of the curves indicates how frequently a certain y-value occurred. Medians of CH_4 emission distributions are shown as red lines, and 75^{th} and 25^{th} percentile are shown as black lines. On the right, the wind sectors with the eddy covariance tower in the center (black cross) are shown.

is much smaller (second row in Fig. B.11). In summary, neither high wind speed nor high temperatures act as a driver for the high CH_4 emission from $shore_{120°}$. In contrast, the peak at 180 °–190 ° can be explained reasonably well using air temperature and friction velocity in a multiple linear regression ($R^2 = 0.44$). Using the same predictors results in an R^2 of 0.20 for the peak at $shore_{120°}$.

The ratio of CO_2-C to CH_4-C emissions at night (PAR<20 µmol m^{-2} s^{-1}) has a value of $CH_4/CO_2 = 0.060^{0.076}_{0.049}$ for fluxes with an open-water weighted footprint fraction of more than 60 %, whereas the ratio amounts to $CH_4/CO_2 = 0.020^{0.024}_{0.015}$ (Median $^{75\ \%\ \text{Percentile}}_{25\ \%\ \text{Percentile}}$) for fluxes with an open-water weighted footprint fraction of less than 20 %.

B.3.4 *UPSCALED CO_2 FLUX*

We use the estimated open-water CO_2 flux from the merged polygonal pond and the modeled CO_2 flux from the semi-terrestrial tundra to linearly up-scale the CO_2 flux for the polygonal tundra of Samoylov Island (excluding larger lakes, the method described in Sect. B.2.4.4). As we have not obtained estimates for the CH_4 fluxes from *tundra* and *pond* land-cover types, we only upscale CO_2.

We estimate that when one includes the CO_2 flux from thermokarst ponds, the river terrace landscape's CO_2 uptake is ~ 11% lower than

the uptake of semi-terrestrial tundra without ponds. The modeled CO_2-C flux from the semi-terrestrial tundra (without consideration of thermokarst pond fluxes) accumulated to -16.29 ± 0.43 g m^{-2} during the observation period (60.5 days). If separated into months, the modeled CO_2-C flux from the semi-terrestrial tundra amounts to -15.01 ± 0.26, -3.56 ± 0.33 and +2.35 ± 0.11 g m^{-2} in July (19.8 days), August (31 days), and September (9.7 days), respectively. When one includes the CO_2 flux from the merged polygonal pond to represent all thermokarst ponds on Samoylov Island, the resulting estimate of the landscape CO_2 flux amounts to -14.47 ± 0.40 g m^{-2} (60.5 days), with monthly fluxes of -13.75 ± 0.24, -2.99 ± 0.31, and +2.27 ± 0.10 g m^{-2} in July (19.8 days), August (31 days), and September (9.7 days), respectively. Thus, the results show that thermokarst ponds have the largest impact on the landscape's CO_2 flux in August. In September, accounting for thermokarst ponds leads to a 3.5 % lower estimate of landscape CO_2 emissions.

B.4 DISCUSSION

B.4.1 *CO_2 FLUX*

Only a limited number of EC CO_2-flux studies from permafrost-affected ponds and lakes are available (studies with "EC" in Tab. B.1). Estimates of open-water EC CO_2-C flux range from 0.059 g m^{-2} d^{-1} (Jammet et al., 2017), to 0.11 g m^{-2} d^{-1} (Eugster et al., 2003), to 0.22 g m^{-2} d^{-1} (Jonsson et al., 2008). Our estimate of 0.12 $^{0.24}_{0.0014}$ g m^{-2} d^{-1} is, therefore, well within the range of open-water CO_2-C fluxes observed with the EC method. Other studies using different methods report a wider range of open-water CO_2 fluxes in arctic regions. These fluxes range from a minor CO_2-C uptake (-0.14 g m^{-2} d^{-1}, Bouchard et al. (2015)) to substantial emissions of CO_2-C (up to 2.2 g m^{-2} d^{-1}, Abnizova et al. (2012)). A modeling study involving multiple lakes in Northeast European Russia found that they produce almost zero emissions (0.028 g m^{-2} d^{-1}, Treat et al. (2018)).

Strikingly, our estimates of open-water CO_2 emissions are approximately 12–18 times smaller than those that have been previously reported for open-water CO_2 emissions at the same study site (Abnizova et al., 2012). One reason for the divergent results might be the different methods used. In Abnizova et al. (2012), the thin boundary layer model (TBL), following Liss and Slater (1974), was applied to estimate CO_2 emissions from CO_2 concentrations. However, one other study found good agreement between the EC method and the TBL (Eugster et al., 2003). In addition, in contrast to the larger merged polygonal pond we focus on, Abnizova et al. (2012) measured two polygonal ponds (they took 46 water samples in August and September 2008). These two ponds might have had exceptionally high CO_2

Table B.1: Daily mean water-atmosphere CO_2 & CH_4 fluxes from different study sites. TBL is the abbreviation for thin boundary layer model, EC for eddy covariance, CH for chamber measurement, MOD for modelled fluxes, STO for storage fluxes, and NEW for the method used in this study. All fluxes are given ± standard deviation, except of fluxes from this study are given as Median $^{75\%\ \text{Percentile}}_{25\%\ \text{Percentile}}$.

STUDY	LOCATION	PERIOD/TIME	STUDY SITE	METHOD	CO_2-C FLUX $\left[g\ m^{-2}d^{-1}\right]$	CH_4-C FLUX $\left[mg\ m^{-2}d^{-1}\right]$
This study	Lena Delta, Northern Siberia	11.07.– 10.09.2019	merged polygonal pond	EC/NEW	$0.13\ ^{0.24}_{0.00}$	$14.10\ ^{18.67}_{11.23}$
			merged polygonal pond shore	EC	–	$12.96\ ^{15.11}_{10.34}$ – $19.18\ ^{24.47}_{14.26}$
Abnizova et al. (2012)	Lena Delta, Northern Siberia	01.08. – 21.09.2008	Samoylov Pond	TBL	1.50 – 2.20	–
			Samoylov Lake	TBL	1.40 – 2.10	–
Jammet et al. (2017)	Northern Sweden	2012 – 2013	Lake Villasjön	EC	0.059	13.42 ± 1.64
Jonsson et al. (2008)	Northern Sweden	17.06. – 15.10.2005	Lake Merasjärvi	EC	0.22 ± 0.002	–
				TBL	0.30 ± 0.01	
Eugster et al. (2003)	Alaska	27.07 – 31.07.1995	Toolik Lake	EC	0.11 ± 0.033	–
				TBL	0.13 ± 0.003	
				CH	0.37 ± 0.060	
Jansen et al. (2019)	Northern Sweden	Year round, 2010 – 2017	Villasjön	CH	0.22 ± 0.047	14.04 ± 2.25
			Inre Harrsjön		0.25 ± 0.05	10.39 ± 1.40
			Mellersta Harrsjön		0.73 ± 0.067	13.76 ± 2.81

Table B.1.: Continued from previous page.

STUDY	LOCATION	PERIOD/TIME	STUDY SITE	METHOD	CO_2-C FLUX $\left[g\ m^{-2}d^{-1}\right]$	CH_4-C FLUX $\left[mg\ m^{-2}d^{-1}\right]$
Bouchard et al. (2015)	NE Canada	July 2013 & 2014	Bylot Island, Polygon ponds Lakes	TBL	-0.14 – 0.74 -0.085 – 0.062	0.50 – 6432 0.70 – 74.5
Sepulveda-Jauregui et al. (2015)	Alaska	June – July 2011 & 2012	8 Lakes, Yedoma 32 Lakes, Non-Yedoma	TBL & STO	0.60 ± 0.58 0.10 ± 0.10	92.86 ± 35.72 16.80 ± 8.61
Treat et al. (2018)	Northeast European Russia	2006 – 2015	Multiple Lakes	MOD	0.028 ± 0.00011	0.84 ± 0.0
Sieczko et al. (2020)	Northern Sweden	July – August 2017	Lake Ljusvatterntjärn	CH	–	2.95 ± 0.75
Ducharme-Riel et al. (2015)	North-East Canada	Summer 2008	15 lakes	TBL	0.20 ± 0.093	–
Repo et al. (2007)	Western Siberia	03.07. – 06.09.2005	MTlake FTlake MTpond	TBL TBL TBL	0.14 ± 0.11 0.41 ± 0.25 0.44 ± 0.25	–
Lundin et al. (2013)	Northern Sweden	2009 (only ice-free season)	27 lakes	TBL	0.18 ± 0.11	–
Kling et al. (1992)	Alaska	1975 – 1989	25 lakes	TBL	0.25 ± 0.040	5.16 ± 0.96

concentrations and might not be representative of polygonal ponds in our study area. If the polygonal ponds in the footprint of our EC measurements emitted CO_2 in the quantities suggested by Abnizova et al. (2012), we would expect to see their signal more clearly in our measurements.

Our approach of combining a footprint model with a land-cover classification to extract fluxes from different land-cover classes allows us to determine the thermokarst pond CO_2 flux. We report an uncertainty range in respect of the thermokarst pond CO_2 flux; however, identifying the full uncertainty of this flux is not possible using this approach due to the footprint analysis' unknown degree of uncertainty. Still, the results in respect of the thermokarst pond CO_2 flux are plausible and in the expected order of magnitude for two reasons. First, a reduced diurnal variability is observed when the merged polygonal pond influences the flux signal (Fig. B.4). This reduction indicates that the respiration rate from the merged polygonal pond is lower than the respiration rate from the semi-terrestrial tundra, where ample oxygen is available in the upper soil layer. Additionally, since the thermokarst ponds have a lower vegetation density than the tundra, there is less photosynthesis. Second, when focusing on night-time fluxes, when only respiration occurs (i.e. no carbon is taken up), there is a decrease in CO_2 emissions with an increasing weighted footprint fraction of open water (Fig. B.3); this also indicates that there was reduced decomposition in the merged polygonal pond. Overall, based on the data, the findings that thermokarst ponds have lower CO_2 emissions than the semi-terrestrial tundra are reasonable.

B.4.2 CH_4 FLUX

We observe large differences in CH_4 emissions from the four wind sectors. CH_4 emissions from $shore_{120°}$ are significantly higher than from $shore_{50°}$, *pond*, and *tundra* (Sect. B.3.3). Notably, we tested the dependence of these higher fluxes on wind speed and air temperature. We expect high wind speeds to enhance turbulent mixing of the water column and diffusive CH_4 outgassing at the water-atmosphere interface. High wind speeds are also associated with pressure pumping, which potentially fosters the ebullition of CH_4. On the other hand, peak temperatures can lead to peak CH_4 production and emissions due to enhanced biological activity. However, the high emissions from $shore_{120°}$ do not coincide with either of two key meteorological conditions, high wind speeds and high temperatures, which would especially favor high emissions. Thus, the difference in methane flux dynamics between $shore_{120°}$ and $shore_{50°}$ is astounding since the shorelines share many other characteristics.

Both shorelines extend radially (in a fairly straight line) from the EC tower (Fig. B.1), thus contributing similarly to the EC flux. The

underwater topography does not vary significantly between the two shorelines. Meters away from the shore, both shorelines have a water depth of a few centimeters and a few decimeters (see data from Boike et al. (2015a)). As previously described in section B.2.1, both shorelines are dominated by *Carex aquatilis*, and from visual inspection, we could not identify differences in shoot density. We, therefore, assume that the characteristics of the emergent vegetation do not play a major role in explaining the differences between the CH_4 emissions from $shore_{120^\circ}$ and $shore_{50^\circ}$. We also examine the evolution of the shorelines at the merged polygonal pond to check whether erosion along the shoreline could cause the high CH_4 emissions. We compare an image from 1965 (U.S. Geological Survey, EROS Center, 1965) with the current (2019) shoreline, yet we cannot identify signs of recent erosion. Furthermore, high-resolution aerial images of this pond from 2008 (Boike et al. (2015b), resolution $>$ 0.33 m) and 2015 (Boike et al. (2015c), resolution $>$ 0.33 m) show no signs of erosion. We therefore assume that past erosion is unlikely is unlikely to have been a factor that caused the high levels of CH_4 emissions we observed in 2019.

Local ebullition of the merged polygonal pond could lead to high CH_4 emissions from $shore_{120^\circ}$. We applied the method proposed by Iwata et al. (2018) to check for signs of ebullition events. This method uses the 20 Hz raw CH_4 concentration data to detect short-term peaks in CH_4 that originate from ebullition events. However, we cannot detect ebullition events in the 20 Hz raw data.

In summary, meteorological conditions (wind speed and temperature), characteristics of emergent vegetation, coastal erosion, and intense ebullition events, are unlikely to be the main driving factors of the increased CH_4 emissions we observed. Another possible driver of higher CH_4 emissions from $shore_{120^\circ}$ is a small but steady seep ebullition hot spot close to this shoreline (such as ebullition class *Kotenok* in Walter et al. (2006)). Seep ebullition hot spots have been reported to occur heterogeneously in clusters in Alaskan lakes (Walter Anthony and Anthony, 2013). Unfortunately, seep ebullition has not previously been reported in water bodies in our study area, so we did not include measurements targeting this process in our measurement campaign. In future studies, visual inspection of trapped CH_4 bubbles in the ice column during wintertime, as proposed by Vonk et al. (2015), could reveal more information about the cause of the higher CH_4 emissions from $shore_{120^\circ}$, as could funnel or chamber measurements with high spatial coverage.

The results show that the merged polygonal pond emits a similar magnitude of CH_4 as the polygonal tundra surface under similar meteorological conditions and when excluding the high emissions from $shore_{120^\circ}$. However, substrate availability and temperature dynamics differ substantially. Additionally, in dense soils, methane diffuses slowly enough through soil layers containing oxygen that the methane

can be oxidized before reaching the surface. In contrast, methane emitted in ponds can reach the surface quickly through ebullition or plant-mediated transport in addition to diffusion. Therefore, we expect to see larger differences between the CH_4 emissions from the merged polygonal pond and the polygonal tundra, more akin to the differences that have been detected in a subarctic lake and fen by Jammet et al. (2017). However, we see no significant difference in the CH_4 emissions from the open-water areas of the merged polygonal pond and the polygonal tundra surface (Fig. B.6 & B.10).

Since many other thermokarst ponds in our study area are smaller than the merged polygonal pond (making them unsuitable to study using the EC method), and since smaller ponds tend to be greater emitters of methane (Holgerson and Raymond, 2016; Wik et al., 2016), our measurements might provide a lower limit of overall thermokarst pond CH_4 emissions.

We estimate a CH_4-C flux of 13.38 $^{15.92}_{10.55}$ (Median$^{75\ \%\ \text{Percentile}}_{25\ \%\ \text{Percentile}}$) mg m^{-2} d^{-1} from the merged polygonal pond and 12.96 $^{15.11}_{10.34}$–19.18 $^{24.47}_{14.26}$ mg m^{-2} d^{-1} from the shores of this pond. This is higher than the fluxes measured by Jammet et al. (2017) from a sub-arctic lake (Tab. B.1). The authors report a mean annual CH_4-C flux of 13.42 $\pm$ 1.64 mg m^{-2} d^{-1} and a mean ice-free season CH_4-C flux of 7.58 $\pm$ 0.69 mg m^{-2} d^{-1}. A study focusing on 32 non-Yedoma thermokarst lakes in Alaska found CH_4-C emissions similar to our results (16.80 $\pm$ 8.61 mg m^{-2} d^{-1}, Sepulveda-Jauregui et al. (2015)). Also, a synthesis of 149 thermokarst water bodies north of $\sim$ 50° reports CH_4-C emissions in the same order of magnitude (27.57 $\pm$ 14.77 mg m^{-2} d^{-1}, Wik et al. (2016)). However, other recent studies have reported considerably lower CH_4-C emissions of 2.95 $\pm$ 0.75 mg m^{-2} d^{-1} in Northern Sweden (Sieczko et al., 2020) and, in contrast, a study finding CH_4-C emissions of up to 6,432 mg m^{-2} d^{-1} in Northeast Canada (Bouchard et al., 2015). The wide range of water-body methane emissions militates in favor of caution when generalizing our results, even for Samoylov Island, especially since the emissions within the merged polygonal pond have been shown to be heterogeneous. Instead, after finding a hotspot in CH_4 emission at the pond shore, we would like to highlight that the gathering of additional measurements – for example employing funnel traps or counting bubbles in ice – will help to better constrain thermokarst pond CH_4 dynamics in their full complexity. Nevertheless, our measurements provide a robust lower limit of thermokarst pond CH_4 emissions.

B.4.3 *UPSCALING THE CO_2 FLUX*

We upscale the CO_2 emissions for the river terrace on Samoylov, an area for which we have access to a high-resolution land-cover classification. We find that we overestimate the carbon-dioxide uptake of the

polygonal tundra by 11 % when we do not account for the thermokarst ponds' CO_2 emissions. A similar approach by Abnizova et al. (2012) found a potential increase of 35–62 % in the estimate of CO_2 emission from the Lena River Delta when including small ponds and lakes in the landscape CO_2 emission calculation. If we follow the upscaling approach by Abnizova et al. (2012) and consider overgrown water as part of the thermokarst ponds, the estimate of the landscape CO_2 uptake would decrease by 19 %. Kuhn et al. (2018) also found water bodies in arctic regions to be an important source of carbon, which could outbalance the carbon dioxide uptake of the semi-terrestrial tundra in a future climate. In summary, our results demonstrate that open-water CO_2 emissions can substantially influence the summer carbon balance of the polygonal tundra. With respect to the night time emissions, we find that per gram CO_2-C thermokarst ponds emit 0.06 g CH_4-C whereas the semi-terrestrial tundra only emits 0.02 g CH_4-C. This finding underlines again that, especially when considering thermokarst ponds, CH_4 emissions are of significant interest. Even though mean CH_4 emissions from the semi-terrestrial tundra and open water are of similar magnitude, we expect that the impact of thermokarst ponds on the carbon balance would be even greater when accounting for CH_4 due to locally high emissions.

Our results suggest that future studies that aim to capture a representative landscape flux should pay extra attention to the water bodies in their footprint. The CO_2 flux from thermokarst ponds has the opposite sign (CO_2 emission) as the semi-terrestrial tundra (CO_2 uptake) during the observation period. Consequently, thermokarst ponds should cover about as much area in the measurement as they do in the landscape area of interest. In this way, the chances of capturing CH_4 hotspots, which can be investigated more closely, are also greater.

B.5 CONCLUSIONS

We find that thermokarst ponds are a carbon source. At the same time, the surrounding semi-terrestrial tundra in our study area acts as a carbon sink during the summer period (July–September), which is in agreement with prior studies (Abnizova et al., 2012; Jammet et al., 2017), despite that we observe much lower open-water CO_2 fluxes compared to previous work at the same study site (Abnizova et al., 2012). Using our approach to disentangle the EC fluxes from different land-cover classes, we posit that during the measurement period, we would overestimate the carbon-dioxide uptake of the polygonal tundra by 11 % if thermokarst ponds were not accounted for. We expect lakes to have a similar effect on the carbon budget, though a smaller one, since lakes (a) cover a similar amount of surface area as the thermokarst ponds in our study site (Abnizova et al., 2012; Muster

et al., 2012) and (b) are weaker emitters of greenhouse gases than ponds (Holgerson and Raymond, 2016; Wik et al., 2016).

In contrast to CO_2 emissions, which are spatially more homogeneous, small-scale heterogeneity in CH_4 emissions makes it difficult to find drivers of CH_4 emissions. We cannot pinpoint the drivers behind the high emissions along parts of the coastline, which we surmise were potentially caused by seep ebullition. Thus, we cannot estimate the impact of this heterogeneity on the landscape scale and, therefore, refrain from upscaling CH_4 emissions. Additionally, the open-water fluxes presented in this paper originate from a single merged polygonal pond since the other polygonal ponds surrounding the EC tower are too small to extract their fluxes using the footprint method applied here. Thus, we do not account for the spatial variability of CH_4 emissions between thermokarst ponds, which can be substantial (Rehder et al., 2021; Wik et al., 2016). However, we note that open-water fluxes were of a similar magnitude as the polygonal tundra fluxes. Consequently, the main impact that thermokarst ponds have on the landscape CH_4 budget might occur through plant-mediated transport and local ebullition.

While being ill-suited for the study of smaller ponds, we underline that the EC method is appropriate for observing greenhouse-gas fluxes from thermokarst ponds as small as 0.024 km^2. The EC method has a higher temporal resolution than the TBL method. It does not disturb exchange processes like the chamber flux method, which eliminates the wind at the water surface. Especially when combining an EC footprint with a land-cover classification, one can distinguish between the contribution of different land-cover classes effectively and also study the fluxes from thermokarst ponds.

We conclude that thermokarst ponds contribute significantly to the landscape carbon budget. Changes in arctic hydrology and the concomitant changes in the water-body distribution in permafrost landscapes may cause these landscapes to change from being overall carbon sinks to overall carbon sources.

B.6 ADDITIONAL FIGURES

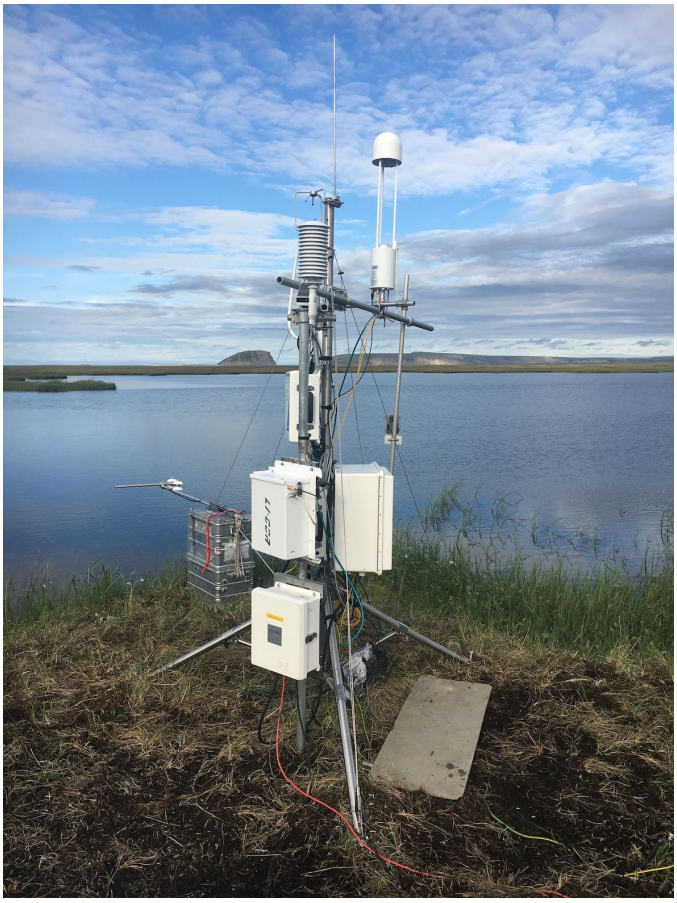

Figure B.7: Picture of the eddy covariance tower with the merged polygonal pond in the background. Picture taken on 11 July 2019 by Zoé Rehder.

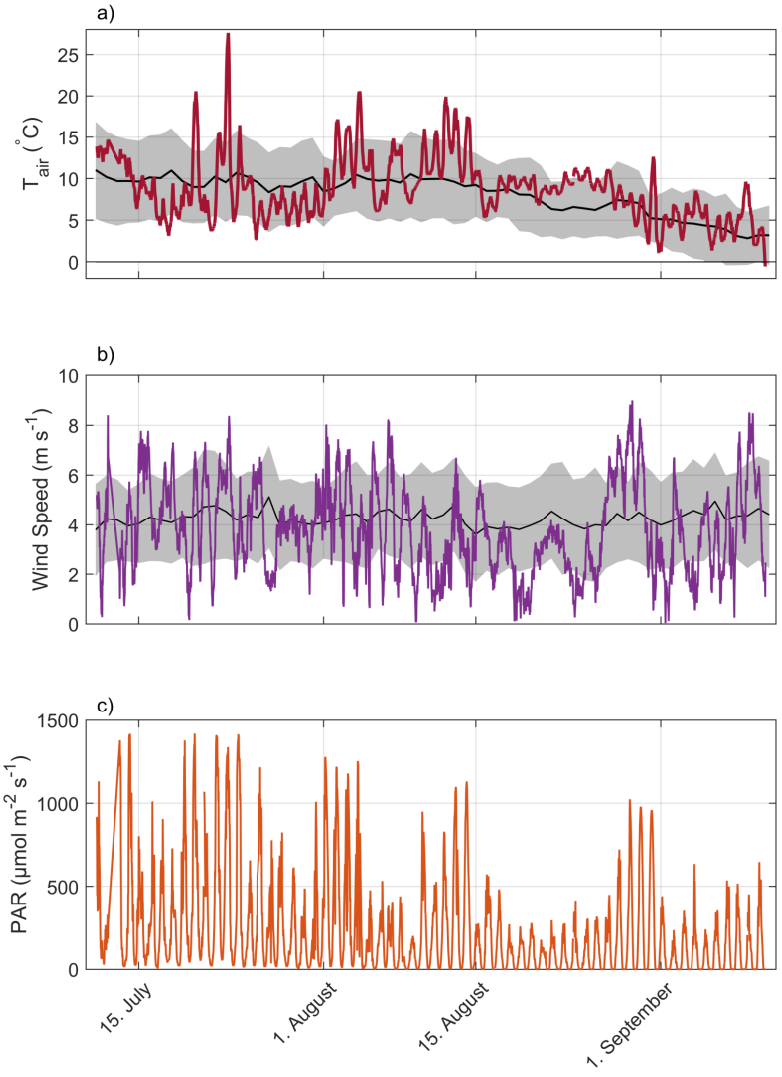

Figure B.8: Timeline of observed meteorological conditions during the observation period with air temperature in 2 meters height (a), wind speed in 3 meters height (b) and photosynthetically active radiation (PAR) (c). Mean values and standard deviation of observations during the past 16 years are plotted as black lines and gray areas.

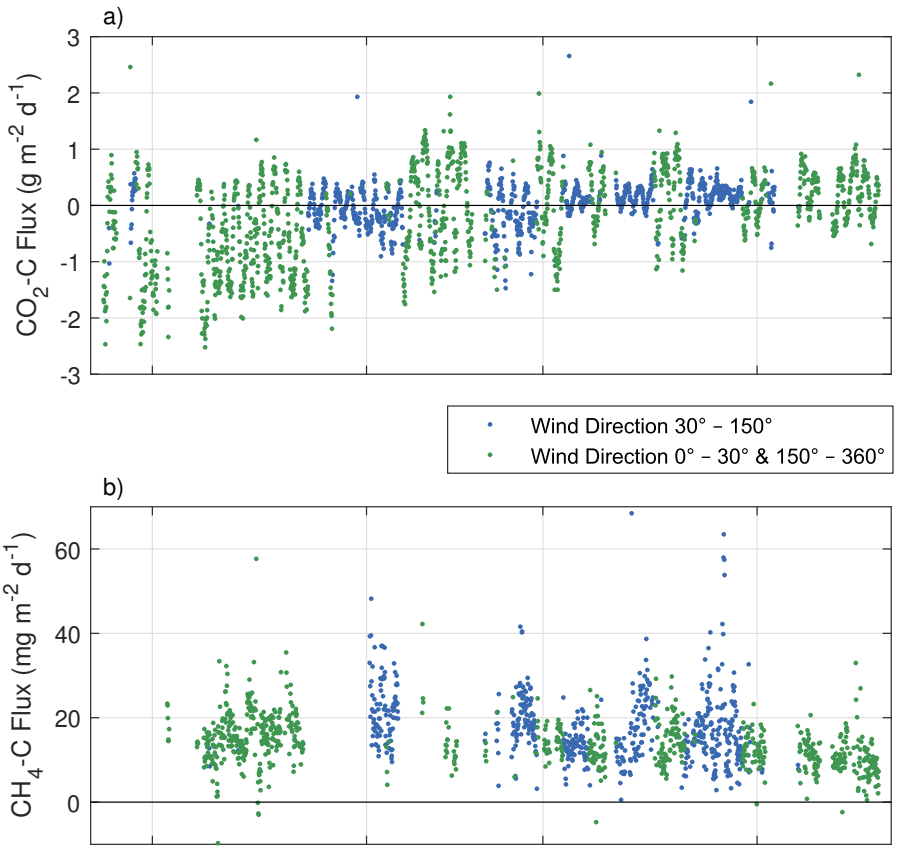

Figure B.9: Time series of 30-minute observed CO_2-C flux intervals (a) and CH_4-C flux with a quality flag of 0 or 1. The blue color represents fluxes originating from the wind direction of the lake (30° – 150° wind direction, mostly mixed signals from semi-terrestrial tundra and the lake surface) and the green color represents fluxes originating from all other wind directions.

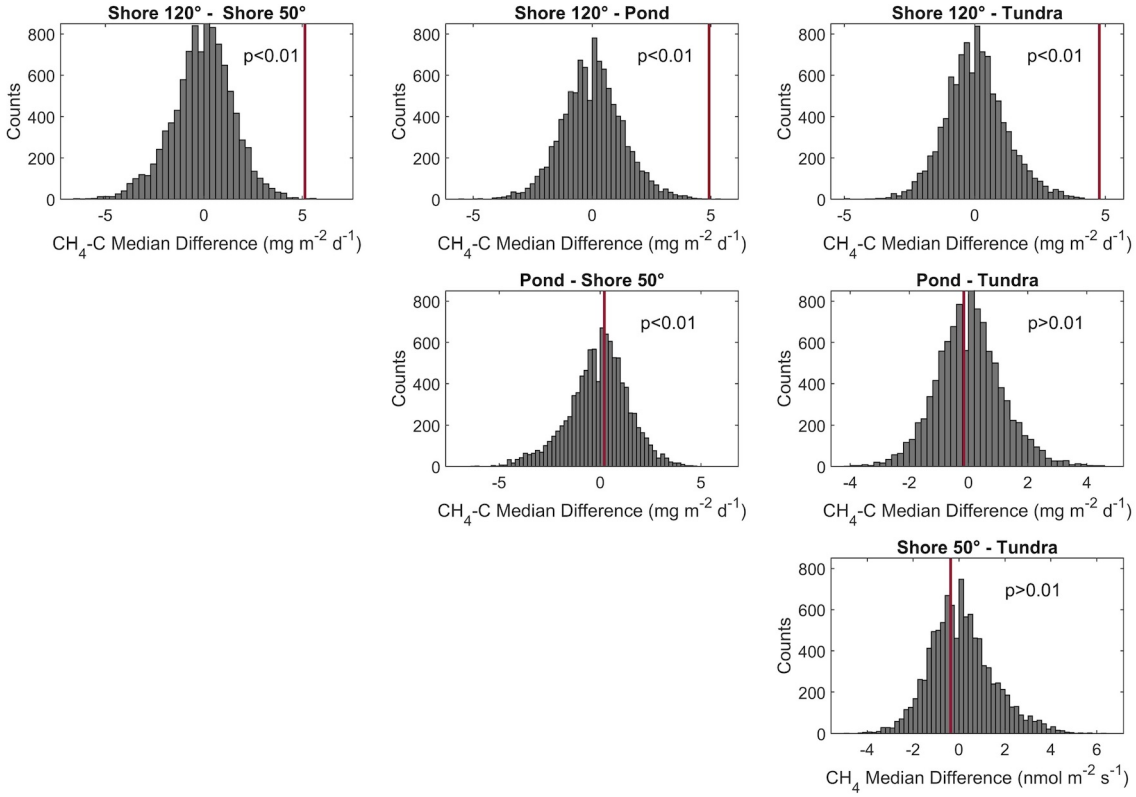

Figure B.10: Histogram of permutation tests between the medians of CH_4 emissions from different wind direction classes in figure B.6. All medians from flux observations during moderate wind-speed conditions. The observed differences in medians between the different wind direction classes are shown in red vertical bars in each plot.

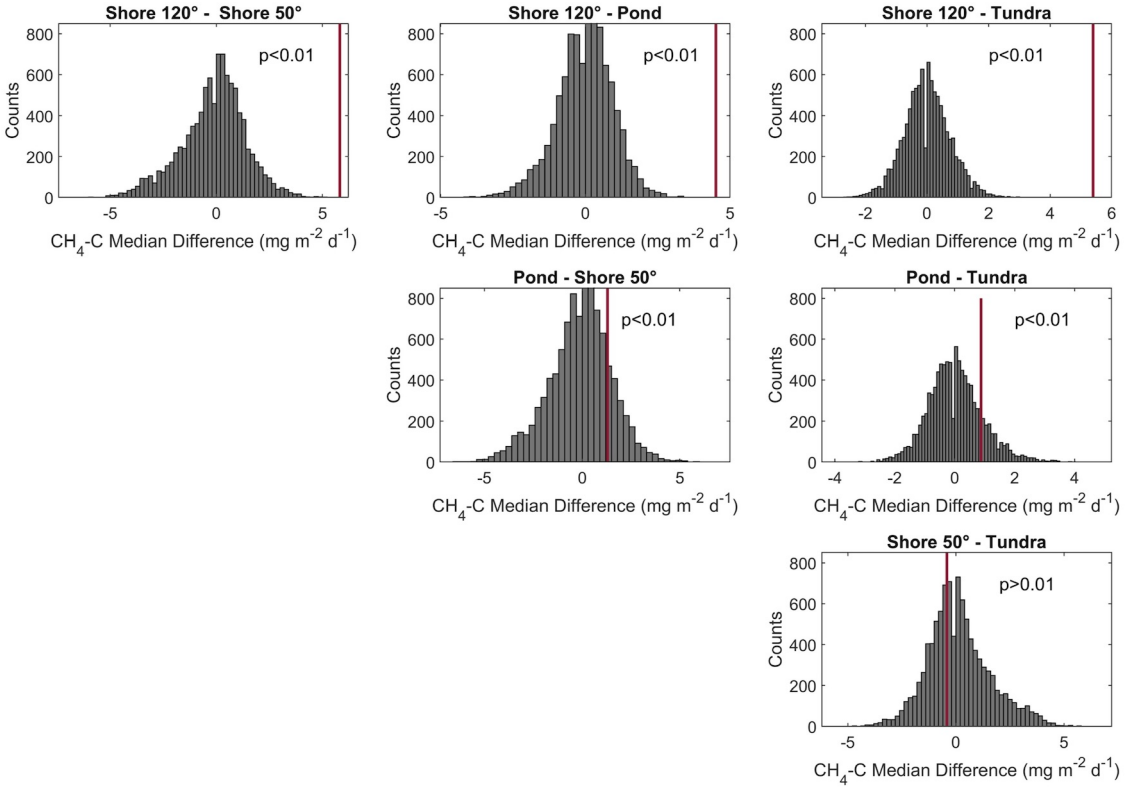

Figure B.11: Histogram of permutation tests between the medians of CH_4 emissions from different wind direction classes in figure B.6. All medians from flux observations during moderate air-temperature conditions. The observed differences in medians between the different wind direction classes are shown in red vertical bars in each plot.

C

NEW MODEL FOR METHANE EMISSIONS FROM PONDS (MEEP) INDICATES HIGH SENSITIVITY OF ARCTIC PONDS TO WARMING

The work in this appendix is a manuscript in preparation to be published:

Rehder, Z., Kleinen, T., Kutzbach, L., Stepanenko, V., Langer, M., and Brovkin, V. (2022). "New model for Methane Emissions from Ponds (MeEP) indicates high sensitivity of Arctic ponds to warming". Manuscript in preparation.

AUTHOR CONTRIBUTIONS

ZR: conceptualization, methodology, software, formal analysis, investigation, writing - original draft, visualisation TK: conceptualization, formal analysis, writing - review & editing, supervision LK: formal analysis, writing - review & editing, supervision VS: conceptualization, methodology ML: methodology, software, writing - original draft VB: conceptualization, formal analysis, writing - review & editing, supervision

New model for Methane Emissions from Ponds (MeEP) indicates high sensitivity of Arctic ponds to warming

Zoé Rehder [1,2], **Thomas Kleinen** [2], **Lars Kutzbach** [3,4], **Victor Stepanenko** [5,6,7], **Moritz Langer** [8,9], **and Victor Brovkin** [2,4]

[1] International Max Planck Research School on Earth System Modelling, Hamburg, Germany

[2] Department of the Ocean in the Earth System, Max Planck Institute for Meteorology, Hamburg, Germany

[3] Institute of Soil Science, Universität Hamburg, Hamburg, Germany

[4] Center for Earth System Research and Sustainability (CEN), Universität Hamburg, Hamburg, Germany

[5] Research Computing Center, Moscow State University, Moscow, Russia

[6] Faculty of Geography, Moscow State University, Moscow, Russia

[7] Moscow Center of Fundamental and Applied Mathematics, Moscow, Russia

[8] Alfred Wegener Institute, Helmholtz Centre for Polar and Marine Research, Telegrafenberg A45, 14473 Potsdam, Germany

[9] Humboldt-Universität zu Berlin, Geography Department, Unter den Linden 6, 10099 Berlin, Germany

ABSTRACT

The Arctic is warming at an above-average rate. Ponds are vulnerable to this warming due to their small thermal inertia compared to lakes, and they are a relevant landscape-scale source of methane under the current climate. Here, we employ a new, process-based model for methane emissions from ponds, MeEP, to investigate the methane-emission response of polygonal-tundra ponds in Northeast Siberia to warming. MeEP differentiates between the three main pond types of the polygonal tundra, ice-wedge, polygonal-center, and merged polygonal ponds. The model resolves the three main pathways of methane emissions – diffusion, ebullition, and plant-mediated transport – at the temporal resolution of one hour, thus capturing daily and seasonal variability of the methane emissions. We perform idealized warming experiments, with increases in the mean annual temperature of 2.5, 5, and 7.5 ° C on top of a historical simulation. The simulations reveal an overall increase of 1.08 g CH_4 $year^{-1}$ $°C^{-1}$ per square meter of pond area. Compared to emissions under present conditions, this corresponds to emission increases of more than 40 % $year^{-1}$ ° m^{-2} C^{-1}. Most of this emission increase is due to the additional substrate provided by the increased net productivity of the vascular plants. Furthermore, plant-mediated transport is the dominating pathway of methane emissions in all simulations. We conclude that vascular plants as a substrate source and efficient methane pathway should be included in future pan-Arctic assessments of pond methane emissions.

C.1 INTRODUCTION

We present first results of a new model for Methane Emissions from Ponds (MeEP). This model has been developed to simulate methane dynamics in arctic ponds since arctic landscapes have a high areal coverage of water bodies (Muster et al., 2017) and ponds are the most numerous among those water bodies (Downing et al., 2006; Polishchuk et al., 2018; Muster et al., 2019). We define ponds using the Ramsar classification, which uses a size limit of $8 \cdot 10^4$ m^2 (Ramsar Convention Secretariat, 2016). We impose the additional condition that the average depth of a pond is below 2 meters (Lim et al., 2001). In our study region, water bodies that are shallow freeze through in winter. Thus, they do not have an unfrozen sediment layer throughout the year (talik) (Pienitz et al., 2008; Arp et al., 2012; Surdu et al., 2014).

Ponds are an important part of the arctic carbon cycle, as they emit carbon dioxide and, notably, methane (Wik et al., 2016; Holgerson and Raymond, 2016; Beckebanze et al., 2021a), which is the greenhouse gas with the higher warming potential. However, the Arctic is warming rapidly (Chapman and Walsh, 1993; Bekryaev et al., 2010; Serreze and Barry, 2011), which induces a multitude of changes to the landscape, and ponds specifically. Ponds are especially vulnerable to climate change due to their small size and low thermal inertia compared to lakes. During longer ice-free seasons, more water is lost to evaporation and subsurface runoff (Anderson et al., 2013; Riordan et al., 2006). So far, arctic ponds have been sustained by the frozen ground, which has a low hydraulic permeability. Loss of permafrost, in turn, promotes drainage (Jepsen et al., 2013). While ponds are already disappearing in some regions, such as landscapes with discontinuous permafrost in Alaska (Riordan et al., 2006; Andresen and Lougheed, 2015), other regions might become richer in ponds with warming (Christensen et al., 2004; Bring et al., 2016).

One landscape type, which is prone to pond formation, at least transitionally, is the polygonal tundra. Ponds are abundant in the polygonal tundra (Muster et al., 2012) and when the ice wedges, which are one the defining features of the polygonal tundra, melt, more ponds are likely to form (Jorgenson et al., 2006; Liljedahl et al., 2016). Though permafrost stores large amounts of carbon (Hugelius et al., 2014), most arctic ponds emit predominantly contemporary, recently fixed, carbon (Negandhi et al., 2013; Bouchard et al., 2015; Dean et al., 2020). However, these newly-formed ponds might emit older carbon than the average global pond. When the permafrost adjacent to the thawing ice wedge degrades, old carbon can leech into the pond fueling methanogenesis (Langer et al., 2015; Prėskienis et al., 2021) and exerting a positive climatic feedback.

Furthermore, the pond's methanogenic communities might shift in response to the warming Arctic. Zhu et al. (2020) predicted that this

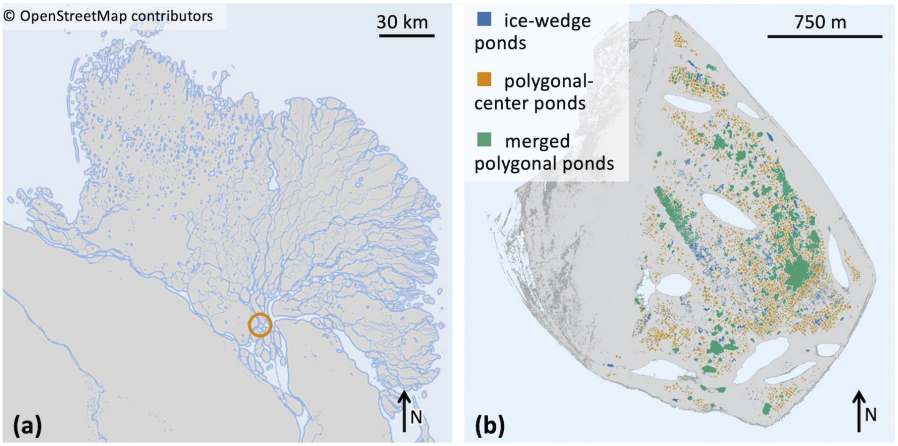

Figure C.1: (a) Map of the Lena River Delta, which is situated in Northeast Siberia. Location of Samoylov Island marked by a circle. (c) Map of Samoylov Island including a classification of all ponds on the river terrace (eastern part of the island) based on the landscape-scale pond classification.

will lead to an additional, strong increase in pond methane emissions. Besides temperature, methanogenesis in water bodies depends on substrate quality (Jong et al., 2018). Vascular plants are known to improve substrate quality (Joabsson and Christensen, 2002; Rehder et al., 2021), and vegetation and its composition in the Arctic are already changing (Villarreal et al., 2012; Bhatt et al., 2013). Thus, we expect methane emissions to change as well.

To analyze as many of these interlinked effects on methane cycling in a single study as possible, we employ the dedicated model MeEP (Methane Emissions from Ponds). We focus on the landscape scale for the polygonal tundra, for which we tuned the model and compared the output of historical simulations to pond measurements. With MeEP, we then explore how pond methane emissions might change in a warmer Arctic.

C.2 MATERIALS AND METHODS

C.2.1 *STUDY SITE IN THE LENA RIVER DELTA*

In this study we focus on the extensively researched Samoylov Island (Kutzbach et al., 2004; Abnizova et al., 2012; Helbig et al., 2013; Zubrzycki et al., 2013; Knoblauch et al., 2015; Boike et al., 2019; Rehder et al., 2021; Beckebanze et al., 2021a, among others). Samoylov Island lies in the Lena River Delta of Northeast Siberia at 72°22′ N and 126°30′ E (Fig. C.1). The island is composed of Holocene sediments and can be divided into two geomorphologically different parts. The western part consists of a floodplain, while the eastern part is a river terrace featuring polygonal tundra (Zubrzycki et al., 2013; Kartoziia, 2019).

This part of the island contains more than 1300 ponds (Muster et al., 2012) in an area of ~ 3 km^2 (Beckebanze et al., 2021a), and thus is an excellent site to study ponds.

Ponds in the polygonal tundra can be classified into three distinct types depending on the geomorphology (Rehder et al., 2021). Ponds can form on top of ice wedges. These ponds tend to be elongated with steep slopes and directly overlie the remnant of the degraded ice wedge. We label them ice-wedge ponds. Ponds can form in the center of polygons: these ponds are often nearly circular and have a flat bottom. We call them polygonal-center ponds. Since the ice wedges are at the rims, the sediment at the pond bottom is not frozen. Lastly, several connected inundated polygons are classified as merged polygonal ponds. The polygonal structure is still visible along the shoreline, and with regards to their area, these large merged polygonal ponds are very shallow.

C.2.2 *LANDSCAPE-SCALE POND CLASSIFICATION*

To classify the ponds on the landscape scale, we used a dataset presented by Beckebanze et al. (2021a) which provides a new, gap-filled land-cover classification of Samoylov Island's river terrace based on prior work by Muster et al. (2012). The dataset includes information on each water body, such as area, overgrown fraction, and a measure of inverse compactness; the more a pond resembles a circle, the lower is our measure of its inverse compactness. We compute inverse compactness C as the ratio between the area of the smallest circle enclosing a pond A_{circ} and the area of the pond A_{pond} ($C = A_{circ}/A_{pond}$). Since ice-wedge ponds have a distinct elongated shape, while polygonal center ponds are more circular, we used the inverse compactness, in addition to the area, to discriminate the pond types.

- Ponds with an area $5 < A_{pc} < 250$ m^2 and a inverse compactness $C_{pc} < 3$ are classified as polygonal-center ponds.
- Ponds with an area $5 < A_{iw} < 250$ m^2 and a inverse compactness $C_{iw} > 3$ are classified as ice-wedge ponds. In addition, ponds with an area $250 < A_{iw} < 1200$ m^2 and a inverse compactness $C_{iw} > 3.4$ are classified as ice-wedge ponds.
- Ponds with an area $A_{mp} > 250$ m^2 and a inverse compactness $C_{mp} < 3.4$ are classified as merged polygonal ponds.

The results of this classification are summarized in Tab. C.1 and shown in Fig. C.1(b). To evaluate the classification, we compared the pond types of thirty ponds categorized in the field (Rehder et al., 2021) to the algorithm and found a perfect match.

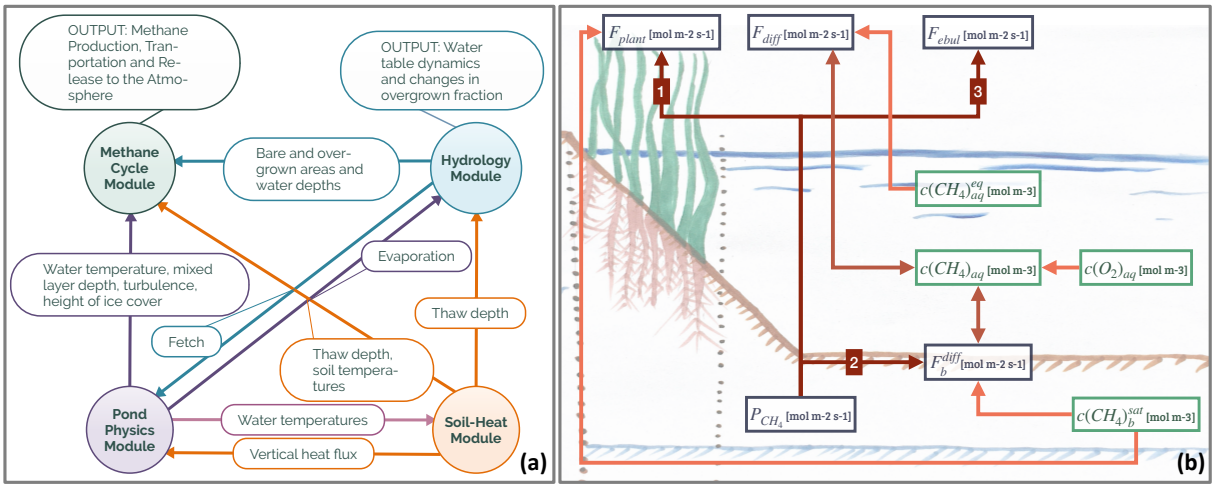

Figure C.2: (a) Overview of the modules constituting MeEP. The variables which are used to couple the modules are labelling the arrows in between the modules. The output of the methane and hydrological modules, which we use in this work, is listed as well. (b) Overview of the methane module with the main variables. F_{plant} denotes the plant-mediated transport, F_{diff} stands for the diffusive flux to the atmosphere and F_{ebul} for ebullition. P_{CH_4} is the rate of methanogenesis, F^{diff}_b the diffusion from the sediment to atmosphere. Finally, c indicates concentration, the subscript aq labels dissolved gases, b the sediment, and the superscript eq concentration in equilibrium with the atmosphere. The exact equation can be found in the supplement.

C.2.3 *SHORT DESCRIPTION AND SET-UP OF MEEP*

MeEP consists of four coupled modules: A pond physics module, a soil-heat module, a hydrological module, and the main focus of this work, a methane module. With time steps of one hour, all modules operate on the same temporal resolution (Fig. C.2(a)). The pond physics, hydrological, and methane modules are all one-dimensional, while the soil-heat module laterally couples pond sediments with the surrounding tundra. We set up the model for Samoylov Island and use one instance of the three modules for each pond type. Each instance of the methane module is split into two parts: One for the overgrown and one for the open-water fraction of the pond. The soil heat module uses a tiling approach, and we employ one tile for each pond type and one tile for the surrounding tundra. A detailed description of the methane and hydrological module is included as a supplement to this paper. The supplement also contains an overview of the constants.

C.2.3.1 POND PHYSICS

We use the lake module FLake (Mironov, 2005) to simulate the physical properties of the pond. FLake is a bulk model predicting the mixing

conditions and the temperature profile of a waterbody. To that end, FLake divides the water column into a mixed layer and a stratified thermocline. FLake also incorporates a description of heat transport in the sediment. We switched off this part of the model in favor of the soil-heat module described below, including freeze and thaw processes. Instead, we compute the heat flux from the sediment into the pond based on the equation in FLake but using the temperature profile of our soil-heat module.

C.2.3.2 SOIL HEAT

We used a simplified version of the CryoGrid permafrost model coupled to the FLake model to represent the transient temperature field in the sediments beneath the ponds, similar to Langer et al. (2016). Unlike the standard CryoGrid model, this version employs an implicit finite difference scheme to solve the heat equation with phase change, originally established by Swaminathan and Voller (1992). This allows the representation of a freezing curve for free water with a discrete phase change at 0 °C. We emphasize that this is a good first-order approximation for sandy and organic-rich sediments such as those present at the study site. The uncoupled soil-heat model was successfully applied to determine the thickness and shape of taliks beneath serpentine river channels in the Lena-Delta (Juhls et al., 2021). The coupling between FLake and CryoGrid at the top of the sediment domain was achieved by applying the bottom water temperature provided by FLake as the upper boundary condition to the sediment domain. The lower boundary (at 20m depth) was defined by a constant geothermal heat flux (0.05 Wm^{-2}). The model framework allows lateral heat exchange with the surrounding permafrost based on laterally coupled tiles (Langer et al., 2016; Nitzbon et al., 2019). We set sediment properties with depth (stratigraphy) individually for the tundra tile and for the pond types. We used local porosity and organic content data from Zubrzycki et al. (2013). Both porosity and organic contents decrease with depths. Under ice-wedge ponds, soil layers starting at 1 m depths consist of 90 % ice.

C.2.3.3 HYDROLOGY

The hydrological model is responsible for water-table dynamics fed into FLake and the partitioning of the pond in an overgrown and open-water part for the methane module. Water-table dynamics are computed as the balance between precipitation, evaporation provided by FLake, and above- and below-ground runoff. Below-ground runoff follows Darcy's law, and the soil properties were set according to local hydraulic conductivity measurements by Helbig et al. (2013).

Changes in the water table height lead to changes in the areas of the overgrown and open-water parts of the pond. To compute

Table C.1: Properties of thermokarst ponds on the river terrace of Samoylov Island. Ponds in MeEP are classified as either polygonal-center (PC), ice-wedge (IW) or merged polygonal (MP) ponds. Each of these types is represented by their typical geometry: The average area of an individual pond (mean A), the total area covered by all ponds of a specific type (total A), as well as the overgrown fraction of a pond type (veg. fr.) were provided by the land-cover classification (Beckebanze et al., 2021a). The mean depths (mean D) is an estimate by Rehder et al. (2021). α is the angle between the slope of the pond and the horizontal plane. Since macrophytes only grow in shallow water, α was set to match the overgrown fraction of each pond type. The holocene river terrace of Samoylov Island has an area of 2984057 m^2 with ponds covering roughly 11.5 %.

POND TYPE	MEAN A [m^2]	MEAN D [m]	α [RAD]	VEG. FR. [%]	TOTAL A [m^2]
PC	56	0.6	0.36	53.6	136677
IW	58	0.8	0.30	61.0	41172
MP	1305	1.2	0.20	22.8	165819

these changes, we assume the pond's cross-section to be an isosceles trapezoid, with an angle α between the slope and the horizontal plane. Plants are assumed to grow in all parts shallow enough (water depths < 0.5 m), and α was set so that the allocation to overgrown and open water matches observations (Tab. C.1). The methane module is executed for each part of the pond and uses the respective mean water depths.

C.2.3.4 METHANE

The methane module is separated into two parts: One for the open-water (see Fig. C.2(b)) and one for the ice-covered season. In summer, the model is built on three main assumptions:

- We assume equilibrium between production and emission in each time step. Under this assumption, all variables become stationary and time-dependent terms are zero. Therefore, we can find an analytical solution to our equations.
- We assume that there is no lateral mixing between the overgrown and the open-water parts of a pond. Thus, we can solve the methane module individually for each part of the pond.
- We assume that the whole water column is well mixed in summer and that the methane concentration throughout the water column is constant.

In MeEP, methane is produced exclusively in the sediment with the production being dependent on the sediment temperature T_b and thaw depth h_s (Stepanenko et al., 2011) as follows:

$$P_{CH_4} = \frac{P_0}{a} \cdot q_{10}^{(T_b - 273.15)/T_{10}} \cdot (1 - e^{-a h_s}) \cdot f_{prod} \qquad [\text{mol m}^{-2}\ \text{s}^{-1}]. \tag{C.1}$$

Moreover, the methane production depends linearly on the net-primary productivity through f_{prod}, which is based on Walter et al. (2001) and additionally takes the overgrown versus open-water fraction into account using the ratio of the two areas, as vascular plants increase substrate quality. q_{10} and T_{10} [C] are constants describing the temperature dependence, while a [m^{-1}] determines how quickly the methane production decreases with sediment depth.

All the methane produced in a time step is emitted in the same time step through one of three pathways. First, in the overgrown part of the pond, evading through emergent macrophytes is the most efficient pathway for methane (plant-mediated transport, based on Walter et al. (1996)). The amount of methane transmitted through vascular plants depends on the variables thaw depths and leaf-area index as a measure for the seasonality and density of the vegetation. We assume a fixed fraction of the plant-mediated methane to be oxidized (f_{ox}) and compute the plant-mediated transport as

$$F_{plant} = (1 - f_{ox}) \cdot \min\{\beta \cdot f_{growth} \cdot h_s \cdot c(CH_4)_b^{sat}, P_{CH_4}\}\ [\text{mol m}^{-2}\ \text{s}^{-1}]. \tag{C.2}$$

β [s^{-1}] is a dimensionless factor describing plant density and their ability to conduct methane combined with a rate factor Walter et al. (2001). f_{growth} is a dimensionless measure of the plant-growth which depends on the leaf-area index. $c(CH_4)_b^{sat}$ is the saturation concentration of methane in the soil, which we compute using temperature-dependent Henry's constants ($H_b^{CH_4}$ and $H_b^{N_2}$). The concentration is controlled by the hydrostatic pressure at the pond bottom p_h and the partial pressure of nitrogen (N_2), which we assume to be in equilibrium with the atmosphere in the water column and decay exponentially in the sediment (Stepanenko et al., 2011; Bazhin, 2001). The saturation concentration then reads

$$c(CH_4)_b^{sat} = \phi \cdot H_b^{CH_4} \cdot \gamma \cdot \left(p_h - \frac{c(N_2)_{eq}}{H_b^{N_2}} \cdot e^{\frac{-\lambda_{N_2} \cdot h_s}{2}} \right) \qquad [\text{mol m}^{-3}]. \tag{C.3}$$

Further, the saturation pressure depends on the porosity of the sediment ϕ [$m^3\ m^{-3}$], which is set based on measurement data (Helbig et al., 2013) and a dimensionless threshold γ, which was tuned.

Next, methane is diffused through the water column and into the atmosphere. We compute diffusion based on the balance

$$F_b^{diff} - F_{diff} - F_{ox} = 0, \tag{C.4}$$

where F_b^{diff} and F_{diff} stand for the methane flux between sediment and water column and between water column and atmosphere, respectively. Diffusion is the slowest pathway; thus, we dynamically account for oxidation (F_{ox}) using the Michaelis-Menthen relation with constant determined by Martinez-Cruz et al. (2015). We compute F_b^{diff} based on the gradient between the concentration in water and sediment multiplied with the diffusivity based on Sabrekov et al. (2017). For diffusion we utilize

$$F_{diff} = k_p(c(CH_4)_{aq} - c(CH_4)_{aq}^{eq}) \qquad [\text{mol m}^{-2}\ \text{s}^{-1}] \tag{C.5}$$

and compute the piston velocity k_p following Heiskanen et al. (2014). $c(CH_4)_{aq}$ is the water methane concentration and $c(CH_4)_{aq}^{eq}$ is the methane concentration if the water column were in equilibrium with the atmosphere. We solve eq. C.4 for $c(CH_4)_{aq}$ to compute the fluxes.

Lastly, if more methane is produced than what can leave the sediment through plant-mediated transport or diffusion, this methane escapes the ponds in the form of gas bubbles (ebullition).

Unfortunately, we had no comparable measurements for an emission peak in spring. Nevertheless, methane dynamics in winter are also included in MeEP. We assume there is no exchange between the water column and the atmosphere while the pond is ice-capped; however, methane is still produced in the sediment until the sediment freezes again. This methane accumulates in the water column, where part of it oxidizes until the oxygen in the water column is depleted. Furthermore, if methane concentrations exceed a temperature-dependent threshold, the methane gasses out. This methane is encapsulated in the ice. The methane accumulated in the water column and the methane caught in the ice are emitted at once when the ice cover comes off.

C.2.4 *FORCING AND SET UP OF SCENARIO SIMULATIONS*

To force MeEP, we use a mixture of reanalysis (ERA5, Hersbach et al. (2020)) and remote-sensing (MODIS, Myneni et al. (2015)) data: We use the ERA5 variables for specific humidity, surface downwards solar radiation, surface downwards thermal radiation, surface pressure, temperature at two-meter height, total precipitation and the wind speed at ten-meter height. Wind speed has been computed as the euclidean norm of two orthogonal wind vectors. From MODIS, we extract the leaf area index for low vegetation and estimate net primary production. Net primary production is calculated as half of the gross primary production. We always extract the grid box closest to our study site for 2002 - 2019. To spin up MeEP, we compute the average

Table C.2: Overview of warming simulations. The simulations (sim.) we conduct are listed in this table. We use historical forcing for the hist_all simulations, and for the experiments forcing adapted to a mean increase in annual temperature ΔT.

SIM.	hist_all	exp2.5_all	exp5.0_all	exp7.5_all
ΔT [°C]	0	2.5	5.0	7.5

Table C.3: Additional simulations to extract the signal from individual components. We force the methane module with mixed forcing from the hist_all and exp5.0_all simulations, separating three components based on (a) temperature and season length-related variables (*exp5.0_Temp*), (b) variables connected to hydrology (*exp5.0_Hyd*), (c) and variables representing vegetation (*exp5.0_Veg*).

COMPONENT	EXP5.0_TEMP	EXP5.0_HYD	EXP5.0_VEG
temp.-related	**exp5.0_all**	hist_all	hist_all
hydrology	hist_all	**exp5.0_all**	hist_all
vegetation	hist_all	hist_all	**exp5.0_all**

Temperature-related variables: Thaw depth, Deardoff velocity, pond mixed-layer and bottom temperature, ice thickness and it's changes since the last time step.
Hydrology: Areas and mean depths of the overgrown and open-water parts of the ponds.
Vegetation: Leaf area index and net primary productivity.

year from this period and force MeEP for ten years with this average forcing. For analysis, we use the years 2004-2019. At the beginning of 2004, the vegetation cover is reset once.

In addition to a historical simulation *hist_all*, we simulate warming scenario simulations. To that end, we scale each forcing variable to fit a ΔT warmer Arctic, with $\Delta T[°C] \in \{2.5, 5, 7.5\}$ (*exp2.5_all*, *exp5.0_all*, and *exp7.5_all*). We determine expressions to scale the forcing variables using MPI-ESM simulations (Wieners et al., 2019; Mauritsen et al., 2019) from the 1pctCO2-Scenarios of CMIP6 (Eyring et al., 2016). We fit each variable to the local annual mean temperature for each month, if possible linearly. Otherwise, we use a quadratic fit. Then, for a given temperature increase ΔT, we can compute a corresponding monthly increase in the forcing. We interpolate linearly between two values to apply this monthly increase to hourly time steps.

Lastly, to extract the impact of specific components on the pond methane emissions, we simulate the methane module with mixed forcing from the hist_all and exp5.0_all (Tab. C.3). The components we extract are (a) temperature and season-length related variables (*exp5.0_Temp*), (b) variables connected to hydrology (*exp5.0_Hyd*), (c)

Table C.4: Tuning parameters. The parameters listed below were set using data by Knoblauch et al. (2015).

SYMBOL	VALUE	UNIT	LONG NAME
P_0^v	$1.2 \cdot 10^{-6}$	mol m^{-3} s^{-1}	Base productivity in vegetated pond fraction
P_0^o	$4 \cdot 10^{-7}$	mol m^{-3} s^{-1}	Base productivity in open-water pond fraction
γ	0.5	-	deviation from ebullition threshold
ϵ_a	0.06	m^3 m^{-3}	gas-filled porosity in the sediment
c_1	$1 \cdot 10^{-5}$	-	factor for piston velocity
c_2	0.005	-	factor for piston velocity

and variables representing vegetation (*exp5.0_Veg*). Since mixing the forcing of the historical simulation and the warming scenario simulations leads to artifacts in spring and fall when ice is about to melt or has just formed, we do not account for the spring flush in these simulations. Thus, we only focus on open-water season emissions.

C.3 MODEL TUNING AND VALIDATION

The base productivity in the sediment and the distribution of methane among the three pathways were tuned using measurements by Knoblauch et al. (2015). Their dataset provides time series of the individual methane pathways for five ponds on Samoylov Island during two seasons. In total, six variables were tuned (Tab. C.4). We tuned the general magnitude of the fluxes using the base productivity P_0 (Eq. C.1) and tuned it separately for the overgrown and the open-water part of the pond. γ is a factor used to determine the saturation concentration in the sediment, which uses Henry's law (Eq. C.3). It is introduced as a correction factor to account for the shape of the bubbles; Henry's law was measured over flat surfaces, but bubbles are spherical (Stepanenko et al., 2011). We also tuned the gas-filled porosity in the sediment, for which no measurements were available. This parameter influences the diffusion from the sediment into the water column (Sabrekov et al., 2017). Lastly, we tuned two factors which are used to determine the piston velocity following Heiskanen et al. (2014) (c_1 and c_2). The original study empirically determined these two values for a much larger water body than the ones we represent in MeEP. When comparing the individual flux measurements against modeled values (Fig. C.3), we achieved an R^2 value of 0.65.

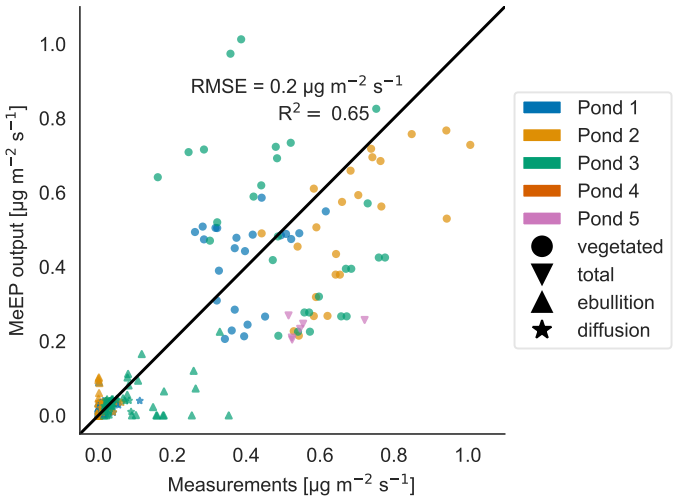

Figure C.3: Measured versus tuned modeled methane emissions. Comparison of measured (x-axis) and modeled (y-axis) methane fluxes for the five ponds measured by Knoblauch et al. (2015) (color code). The fluxes are broken down into different pathways (ebullition and diffusion) where possible. Vegetated fluxes are fluxes measured over the overgrown part of the pond.

To gauge how well the model performs compared to measurements it was not tuned to, we use eddy covariance measurements of a merged polygonal pond on Samoylov Island (Beckebanze et al., 2021a). Eddy covariance fluxes are almost always a compound of fluxes from different landcover classes. In this case, the footprint, the area measured by the eddy covariance instruments, includes both the tundra and the open and overgrown water of the merged polygonal pond. The relative contribution of these three surface classes to the eddy covariance flux varies with time, and we never have a pure signal from the water body. To compare MeEP to measurements, we reverse-engineer the eddy covariance signal using the contribution of each of the three classes to the footprint. The overgrown and open-water fluxes predicted by MeEP are multiplied with their respective cover fraction. To this, we add the mean tundra flux determined with the eddy covariance method and then compare this simulated eddy covariance flux to the real eddy covariance fluxes (Fig. C.4).

We find that the magnitude of the original measured and the simulated flux match well. MeEP-based fluxes are slightly lower, so MeEP output might be a conservative estimate of landscape pond methane emissions. However, there are some differences in temporal development. The spatial heterogeneity likely causes these differences in the measured fluxes, which MeEP can not reproduce. Seep-ebullition (constant ebullition from one spot) likely generated especially high emissions from one point in the measurements. In the simulated fluxes, ebullition is assumed to be constant over the area. Thus, differences in

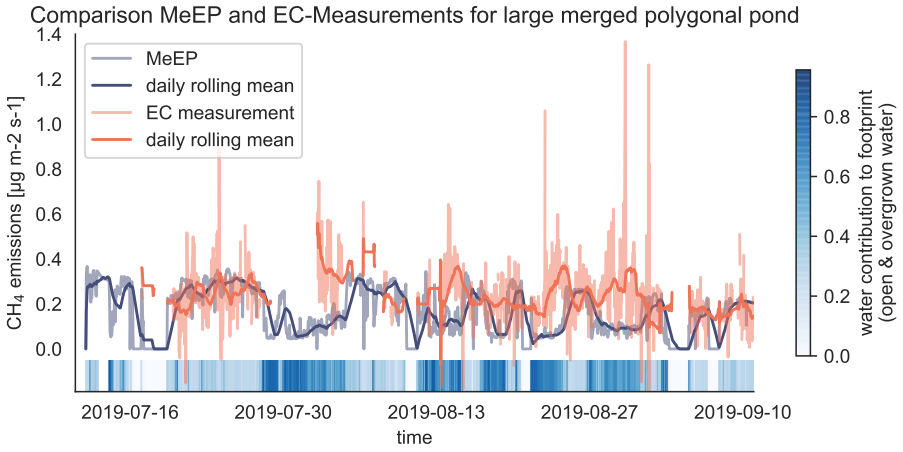

Figure C.4: Validation of MeEP with eddy covariance (EC) measurements. We compare the EC flux measurements (Beckebanze et al., 2021a) to simulated EC flux using the overgrown and open-water fluxes modeled with MeEP and the measured mean tundra fluxes multiplied with their respective contribution to the footprint. The eddy covariance measurements were taken next to a large merged polygonal pond. To visualize how much the pond contributed to the flux in a time step, we added colored strips at the bottom of the plot.

the temporal evolution are expected, and we conclude that the tuning of MeEP was successful.

We want to note that MeEP was designed for an average pond, not for individual ponds. Methane emissions from individual water bodies can be highly variable (Sepulveda-Jauregui et al., 2015; Jansen et al., 2020; Beckebanze et al., 2021a). However, MeEP provides emission estimates for an average pond rather than resolving spatial heterogeneity within a pond.

C.4 RESULTS

C.4.1 *METHANE EMISSION RESPONSE TO WARMING*

MeEP projects an increase of methane emissions with warming (Fig. C.5), from total Samoylov Island pond methane emissions of (321 ± 70) kg CH_4 $year^{-1}$ (mean and standard deviation) per square kilometer river terrace in the hist_all simulation, to (585 ± 99), (899 ± 112) and (1252 ± 126) kg CH_4 $year^{-1}$ km^{-1} in the exp2.5_all, exp5.0_all and exp7.5_all simulations, respectively. Emissions in the exp5.0_all simulation are 180 % higher than in the hist_all simulation. The emission strength under current climatic conditions heavily influences this proportionally strong increase since the emission increase is nearly linear. Using a linear regression between the mean increase in annual air temperature and the total pond emissions (Fig. C.5(B)), we determine an increase of emissions of 0.37 Mg CH_4 $year^{-1}$ $°C^{-1}$ for the whole

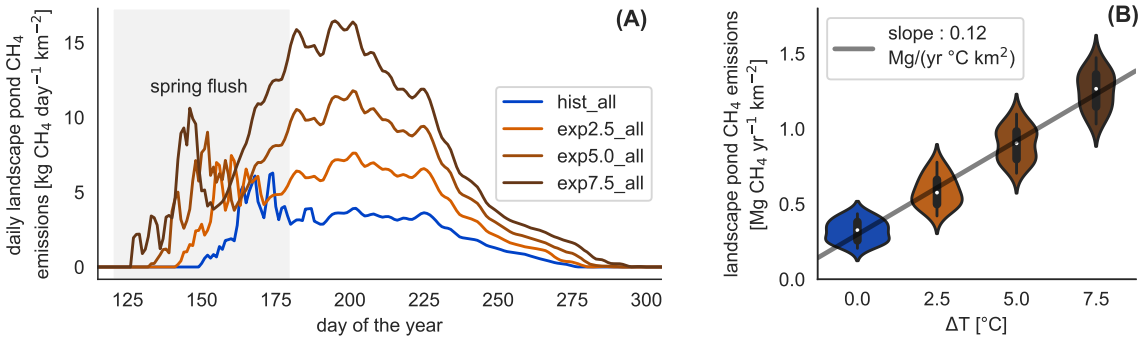

Figure C.5: Daily and annual methane emission changes in the different simulations. (A) Seasonal dynamics of methane emissions from ponds per square kilometer of river terrace on Samoylov Island in scenario simulations. The seasonal cycle exhibits a peak at the beginning of the open water season caused by the spring flush. (B) Linear regression of annual landscape-scale pond methane emissions per square kilometer river terrace versus annual mean temperature increase. The distribution of annual emissions per year in each simulation is depicted as violin plots: The more often a certain y-value occurs, the wider the shape is.

island. Divided by the initial pond area, this equals an increase of 1.08 g CH_4 $year^{-1}$ $°C^{-1}$ per square meter of pond area. The increase in annual emissions is caused by an increase in mean emissions over the open-water season and by a longer open-water season (Fig. C.5(A)). The open-water season lengthens from 109 days on average in hist_all, to 124 days in exp2.5_all, 138 days in exp5.0_all, and 152 days in the exp7.5_all simulation. On average, the growing season lengthens by 5.7 days per degree of warming. We further investigate the interaction of increased season length and elevated temperatures using growing degree days. The accumulated growing-degree days above 5 ° C (GDD5) integrate temperatures and season length in one metric. The annual methane emissions exhibit a clear linear dependence on GDD5 (Fig. C.6). This linear dependence, however, does not hold over all simulations. The differences between the applied forcings cause offsets between the different experiments. While the forcing itself uses ERA5 and MODIS, we used ESM scenarios simulations to determine the forcing variable's sensitivity to warming. We find a strong dependence, especially of net-primary productivity on warming in the ESM simulations, leading to pronounced changes in this variable across MeEP simulations. Suppose two years, one from the hist_all simulation and one from exp2.5_all, have a similar mean annual air temperature. In that case, net-primary productivity will be more than 60% higher in the exp2.5_all simulation than in the hist_all simulation. Thus, air temperature can only be used as a proxy for other forcing variables within one simulation, not across simulations with different forcing. However, air temperature or GDD5 can predict total pond methane emissions within one simulation. Note that, in contrast to Fig. C.5, the

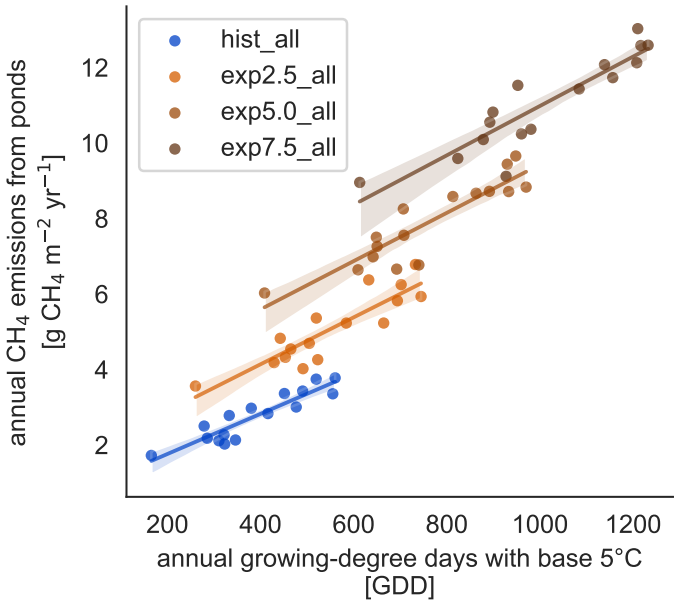

Figure C.6: Growing-degree days as a control on annual methane emissions. For each simulation, the dependence of the cumulative annual methane emissions (y-axis) on the cumulative annual GDD5 (x-axis) can be approximated by a linear regression (solid lines, confidence intervals shown as shaded area).

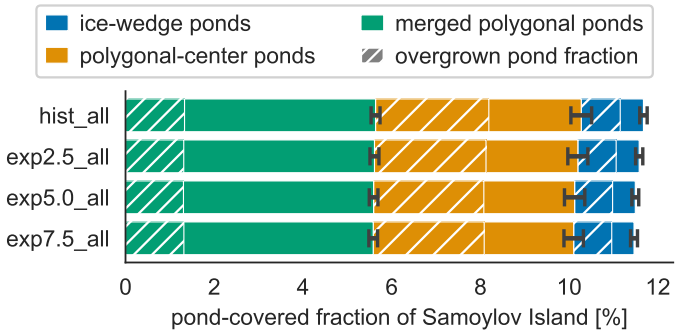

Figure C.7: Pond area changes between simulations. The average landscape fraction covered by each pond type (y-axis) changes slightly between scenarios (x-axis). The overgrown fraction of each pond type is hatched.

emissions displayed in Fig. C.6 are not integrated over the total pond area on the Samoylov Island but are given in relative units per pond area. Thus, we do not account for changes in the pond area.

C.4.2 *HYDROLOGICAL RESPONSE TO WARMING*

The total pond area and its allocation to open and overgrown water change with time between simulations. In MeEP, ponds are initialized at the beginning of the simulation. Though no new ponds can form during a simulation, MeEP computes the water table based on the

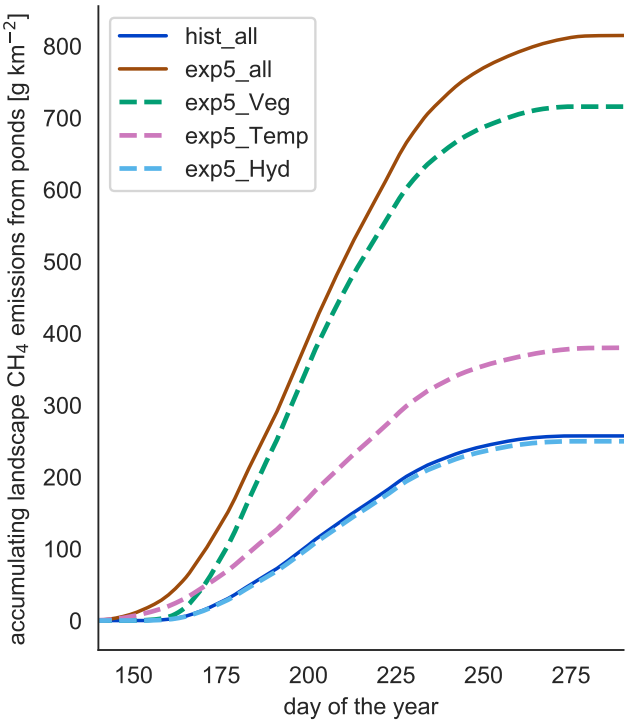

Figure C.8: Components driving changes in methane emissions. To isolate the impact of different component on the increasing methane emissions, we simulate the methane part of MeEP mixing input from hist_all and exp5.0_all (see Tab. C.3). In this figure, we compare the accumulated emissions over the course of the average year between different simulations.

hydrological budget of precipitation, evaporation, and both below- and above-ground runoff. However, MeEP projects only a small reduction in the total pond area in response to elevated temperatures (Fig. C.7). Even the area reduction of the most extreme warming simulation we conducted (exp7.5_all) is still within the standard deviation of the base simulation hist_all. Total pond areas decrease from a landscape fraction of 11.7 ± 0.4 (mean $\pm$ standard deviation) % in the hist_all scenario to 11.5 ± 0.4 % in exp7.5_all. Consequently, the changes in the areas of open and overgrown water are negligible, and on average, 4.7 ± 0.4 % of the landscape is covered by the overgrown water fraction of ponds. However, the hydrological module of MeEP is rather simple, and we will examine its limitations in the discussion section C.5.3.

C.4.3 *DRIVERS OF METHANE EMISSIONS*

Since the changes in waterbody areas are small, the impact of the hydrology on the total methane emissions is small too. However, the decrease in area is the only response of the system, which leads to a reduction of the emissions under warming (Fig. C.8). Rising temperatures, including a longer open-water season, on the other hand,

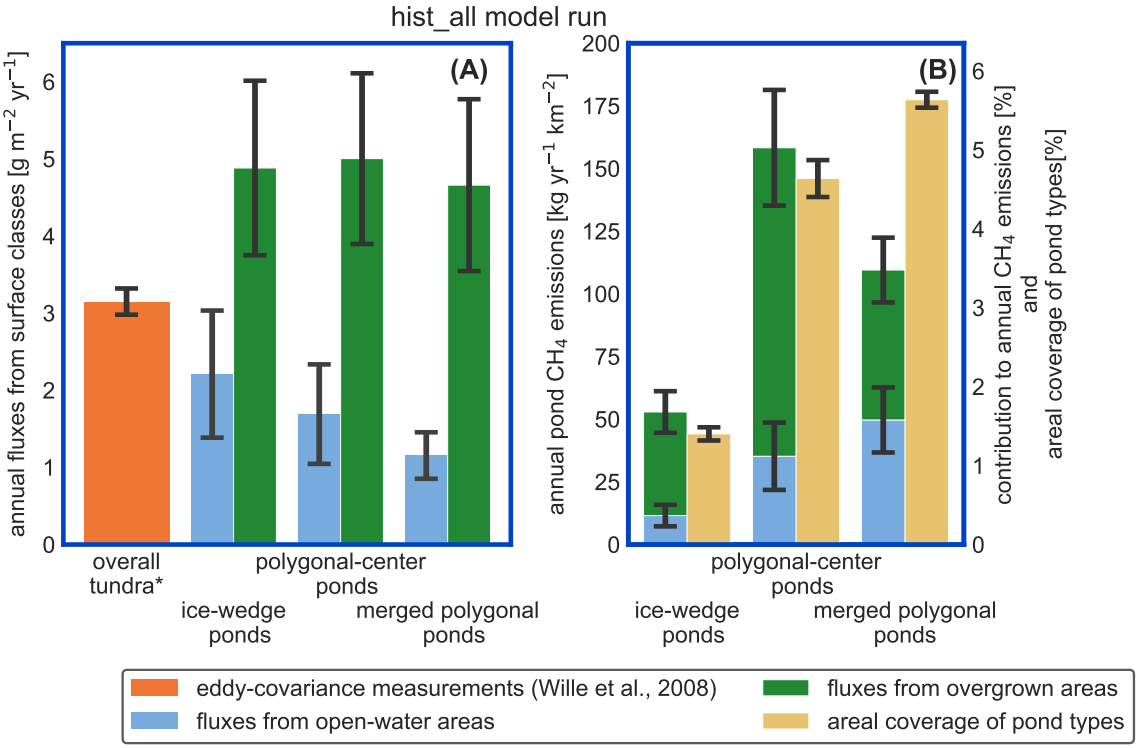

Figure C.9: Impact of pond emissions on landscape methane emissions. (A) For the hist_all simulation, we compare fluxes per area from different landscape elements. The estimate for the overall tundra emissions were acquired with eddy-covariance measurements over the growing season of 2003 (Wille et al., 2008). The influence of ponds on these measurements is low. The methane emissions per square meter of open and overgrown water are broken down per pond type. (B) Methane emissions per square kilometer of river terrace of each pond type are displayed as stacked bars. We compare these emissions per pond type to the area this pond type covers on the river terrace of Samoylov Island (sand-colored bar). This comparison relies on the assumption that the emissions measured by Wille et al. (2008) are representative for river-terrace emissions.

lead to an increase in emissions. Vegetation, however, has the strongest impact. Though emissions start later in the year in the exp5.0_Veg simulation, the slope is much steeper than the simulations which exclude the increased plant productivity. A steeper slope indicates higher mean emissions over the open-water season driven by changes in the vegetation.

C.4.4 *IMPACT OF POND METHANE EMISSIONS ON THE LANDSCAPE SCALE*

The impact of vegetation can also be observed when investigating the impact of overgrown- and open-water fluxes on the landscape scale.

Table C.5: Methane emissions from each pond type. The open-water season fluxes differ between open and overgrown water for the three pond types. Shown here are values from the hist_all simulation. The total pond fluxes are computed using an area-weighted mean.

	CH_4 FLUXES [MG DAY^{-1} M^{-2}]								
	TOTAL POND			OVERGROWN FR.			OPEN-WATER FR.		
	MIN	MED	MAX	MIN	MED	MAX	MIN	MED	MAX
IW	5.44	19.85	84.69	8.33	29.09	101.33	0.0005	4.67	58.19
PC	4.92	18.09	85.57	8.32	29.41	108.83	0.0007	4.42	58.97
MP	2.18	7.92	37.63	9.03	30.49	95.99	0.0001	0.98	20.40

IW, ice-wedge pond; PC, polygonal-center pond; MP, merged polygonal pond.
min, minimum; med, median; max, maximum; fr, fraction.

While the modeled fluxes from overgrown water exceed the measured average tundra fluxes (Wille et al., 2008), fluxes from open water are lower (Fig. C.9 (A)). When comparing the emissions from ponds per square kilometer river terrace to the overall emissions (Fig. C.9 (B)), we find that ice-wedge and polygonal-center ponds emit slightly more methane per unit area of pond than the average tundra. In contrast, merged polygonal ponds emit slightly less. The latter are the pond type with the highest open-water fraction. Open-water fluxes also have a stronger dependence on the pond type. Ice-wedge ponds emit the highest open-water fluxes. The largest ponds, merged polygonal ponds, emit the least methane per area from open water (Tab. C.5). To summarize, though small ponds contribute slightly out-of-proportion to the landscape methane emissions, we do not find that ponds are hot spots of methane emissions in the landscape scale - at least not under the current climate.

Albeit lower than the fluxes from overgrown water in all scenarios, open-water fluxes become more important in the warming simulations (Fig. C.10), mostly due to increased ebullition. The relative importance of diffusion and ebullition differs not only between simulations but also between pond types. In the hist_all simulation, ebullition is four times stronger than diffusion in ice-wedge ponds, three times stronger in polygonal center ponds, and only half as strong as diffusion in merged polygonal ponds. The general trend between pond types is the same in the exp7.5_all simulation, where ebullition is 28, 19, and 8 times stronger than diffusion in ice-wedge, polygonal-center, and merged polygonal ponds, respectively. The relative importance of the plant-mediated fluxes, on the other hand, stays constant over the scenarios, while the impact of the spring flush decreases substantially. In hist_all, the spring flush contributes between 14 - 31 % (minimum and maximum) with a mean contribution of 21 %. In the exp7.5_all

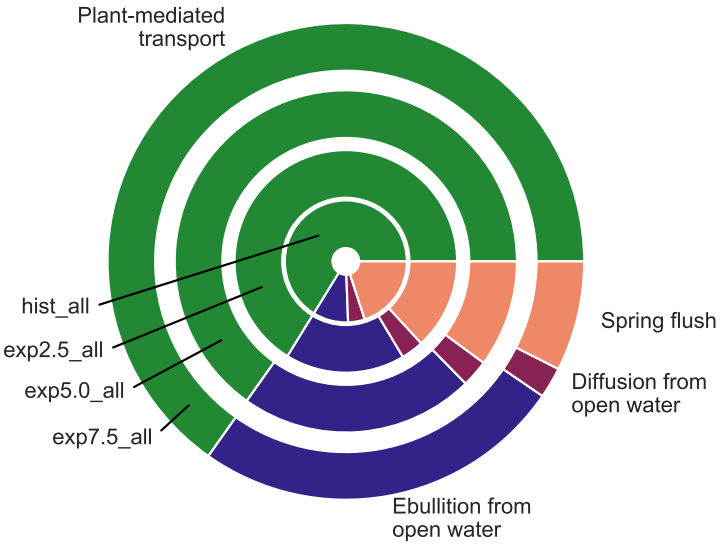

Figure C.10: The contribution of each flux type to the overall emissions in the average year. The size of a segment represents the contribution of the respective flux type. The area of each circle is proportional to the absolute methane emissions of the average year in each simulation.

simulation, the maximal contribution of the spring flush of 12 % is lower than the minimum contribution in the hist_all simulation. Overall, we find that ponds might become hot spots of methane emissions on the landscape scale in a warmer climate. However, this finding strongly depends on how methane fluxes from non-inundated tundra change.

C.5 DISCUSSION

C.5.1 *MEEP MODEL OUTPUT IS CONSERVATIVE COMPARED TO PAN-ARCTIC METHANE FLUX MEASUREMENTS*

Ponds in our study region exhibit comparably low methane emissions (Liebner et al., 2011). Emissions from ponds are of a similar magnitude as the the overall tundra emissions (Fig. C.9, Beckebanze et al. (2021a)). In a circumpolar synthesis, Wik et al. (2016) determined methane emissions from thermokarst ponds and lakes of various sizes. They estimated mean diffusive fluxes of 33 mg day^{-1} m^{-2} and a mean ebullition of 87 mg day^{-1} m^{-2}, leading to open-water methane emissions of as much as 121 mg day^{-1} m^{-2}. The ponds and lakes synthesized in this study are underlain by a wide range of soils, including yedoma; in yedoma-dominated landscapes, lake methane emissions are exceptionally high (Walter et al., 2006; Hughes-Allen et al., 2020). However, Zabelina et al. (2020) derived even higher methane emissions from ponds and small lakes for non-yedoma permafrost in northeastern

Europe (a median of 218 mg day^{-1} m^{-2} for water bodies with an area of $10 - 100$ m^2). They estimate the emissions based on concentration measurements. Thus, they only account for diffusion.

Let us compare the emissions from our study site to other measurements of polygonal tundra ponds. We observe the same trend – emissions in our study site are lower than the measurements – but the general trend between pond types is well represented in MeEP. Bouchard et al. (2015) found open-water emissions with a median of 56.6 mg day^{-1} m^{-2} from ice-wedge ponds, 27.9 mg day^{-1} m^{-2} from polygonal-center ponds and 3 mg day^{-1} m^{-2} from lakes in a polygonal landscape in northeastern Canada in July. As in our model setup, ice-wedge ponds emit slightly more methane than polygonal-center ponds, and larger water bodies emit considerably less. Additionally, the ratio between ebullition and diffusion for ice-wedge, polygonal-center, and very small merged polygonal ponds in northeastern Canada lies between three and four (Prėskienis et al., 2021), comparable to the ebullition-diffusion ratios for ice-wedge and polygonal-center ponds in the hist_all simulation.

Prėskienis et al. (2021) also measured the spring flush. They estimate that up to 52 % of the annual methane is emitted when the ice melts. This is substantially higher than our maximum values of 31 %. Our results are closer to values published by Wik et al. (2016), who aggregated pan-Arctic fluxes. They report an average spring flush of 27 % for thermokarst water bodies, which is still larger than the mean amount in the hist_all simulation of 21 %. Notably, Wik et al. (2016) summarized water bodies of all sizes in the thermokarst category, and Prėskienis et al. (2021) reported lower spring flushes for larger water bodies. Thus, the spring flush modeled by MeEP (Fig. C.5) is in the right order of magnitude but might be a low estimate of the real spring flush.

To sum up, pond methane emissions from our study site are lower than emissions measured elsewhere. Also, the spring flush is a low estimate. Nevertheless, MeEP reproduces features of polygonal-tundra ponds, which have been observed in other parts of the world. Pond methane emissions in the hist_all simulation are comparable to measurements in, e.g., the Canadian Arctic.

C.5.2 *VEGETATION CHANGES INTENSIFY POND METHANE EMISSION INCREASES*

In the whole Arctic, vegetation has a strong impact on methane emissions (Joabsson et al., 1999; Andresen et al., 2016; Turner et al., 2020, e.g.). We can split this impact into two parts. First, vascular-plant productivity increases substrate availability, which increases methanogenesis (Joabsson and Christensen, 2002; Kim, 2015). Second, emergent

macrophytes are a highly efficient pathway for methane emissions (Knoblauch et al., 2015).

Plant-mediated transport means gases diffuse with low resistance through the aerenchyma of plants. Aerenchyma are air-filled pores in leaves, roots, and stems of macrophytes (Whiting and Chanton, 1992; Colmer, 2003). The methane flux through these plants increases with their above-ground biomass (Ström et al., 2012; Joabsson and Christensen, 2002), and the above-ground biomass correlates linearly with the leaf-area index (Andresen et al., 2016). In MeEP, we use the leaf-area index, a variable readily available from remote sensing (Myneni et al., 2015), to modulate the plant-mediated transport (Walter and Heimann, 2000). The leaf-area index increases with temperature in our forcing (Euskirchen et al., 2009). This trend is in line with findings that emergent macrophytes already have become more abundant in some regions, for example, *Arctophila fulva*, a very efficient transmitter of methane (Knoblauch et al., 2015; Andresen et al., 2016), which is also abundant in our study region (Knoblauch et al., 2015). This emergent macrophyte is already expanding, e.g., on Barrow peninsula in Alaska (Villarreal et al., 2012). We find that coverage of emergent macrophytes increases in such a way that plant-mediated transport is limited by methanogenesis rather than by the conductivity and abundance of aerenchyma. In overgrown parts of the ponds, plant-mediated transport is by far the dominating mode of transportation (Whiting and Chanton, 1992; Andresen et al., 2016). When comparing open-water and overgrown fluxes, the contribution of the overgrown part stays constant over all scenarios with increasing methane emissions (Fig. C.10). The plant-mediated transport scales with the increase in total emissions because the density of vascular plants increases with temperature. We represent the density of plants using the leaf-area index in the model. A higher density of vascular plants means a higher density of aerenchyma, which increases the capacity of the plant-mediated transport more efficiently. Thus, this capacity builds up at the same rate as methanogenesis.

Further, vegetation in permafrost regions adds a positive feedback loop to warming (Lara et al., 2019). Higher temperatures increase plant biomass in the Arctic (Euskirchen et al., 2009; Elmendorf et al., 2011; Andresen and Lougheed, 2015), and, with an increasing thaw depth, conditions for plants become more favorable: Nutrients, which are a limiting factor in tundra landscapes, leach out of the thawing permafrost and support vegetation growths (Andresen et al., 2016; Lara et al., 2019). A higher macrophyte cover adds more substrate to the sediment fueling methanogenesis (Joabsson et al., 1999; Joabsson and Christensen, 2002; Ström et al., 2012; Santos Fonseca et al., 2017), which already under present conditions consumes mostly contemporary carbon (Negandhi et al., 2013; Dean et al., 2020). This

increases methane emissions, closing the feedback loop (Lara et al., 2019).

In MeEP, this process is the main driver of elevated emissions under warming (Fig. C.8), leading to an increase in methane emissions that is twice as high as the increase due to higher temperatures alone. The strength of the methanogenesis response to warming is determined by the term f_{prod} (see Eq. C.1). This term prescribes a linear dependence of methane production on changes in net-primary productivity. A connection between plant productivity and methanogenesis has been observed in a subarctic fen (Whiting and Chanton, 1992). However, this connection is species-dependent (Vizza et al., 2017; Ström et al., 2005), and some species typical for European wetlands can also reduce methanogenesis (Grünfeld and Brix, 1999). Unfortunately, we know no study that focuses on the impact of emergent macrophytes on arctic pond or lake methanogenesis.

The linear dependence of methanogenesis on plant productivity is a reasonable first estimate given the evidence that in arctic landscapes, vascular plants enhance methanogenesis (Joabsson and Christensen, 2002; Ström et al., 2003; Lara et al., 2019). A parameterization based on new measurements that focus on macrophytes' impact in ponds on methanogenesis would be a step forward to constrain future pond methane emissions better. A dynamic model of macrophyte coverage and productivity could be included in a second step. Despite uncertainty in the strengths of the link between methanogenesis and vascular-plant productivity, our projections underpin the importance of future vegetation changes for pond methane emissions.

Vegetation changes occur slowly over the years (Villarreal et al., 2012), leading to higher emissions even in comparably cool years. This effect is especially apparent in Fig. C.6: The regressions do not collapse onto a single line. Rather years with the same growing-degree days emit more methane the higher the warming is. However, growing-degree days are a good predictor of annual methane emissions within a simulation. They combine the direct impact of temperature with a measure of how favorable temperatures are for plant growth for each year. In the Arctic, multi-year vegetation changes are already well underway (Bhatt et al., 2013; Wrona et al., 2016). However, vegetation changes in the Arctic do not solely depend on temperature (Wrona et al., 2016), and the Arctic does not become greener in all regions, but also browns in some (Bhatt et al., 2013; Winkler et al., 2021). This browning is strongly connected to changes in hydrology (Winkler et al., 2021).

C.5.3 *HYDROLOGICAL CHANGES SLIGHTLY DECREASE POND METHANE EMISSION*

Depending on local topography, a landscape is more likely to wet or dry under warming (Jones et al., 2022; Miner et al., 2022). The more slopes a landscape features, the more likely it will drain (Bring et al., 2016). However, in a very flat landscape such as our study area, it might get wetter with warming (Christensen et al., 2004). In the polygonal tundra, warming leads to permafrost degradation, which prompts loss of ground ice, subsidence, and pond formation leading to higher methane emissions (Kim, 2015), especially along the ice wedges (Yoshikawa and Hinzman, 2003; Liljedahl et al., 2016). Consequently, a degrading polygonal tundra features an increasing number of ice-wedge ponds (Bouchard et al., 2020; Wickland et al., 2020). As the degradation proceeds, the ponds are inclined to vanish again, either because of infilling or drainage (Stow et al., 2004; Cresto Aleina et al., 2015; Jorgenson et al., 2015; Wickland et al., 2020). Additionally, an increase in emergent macrophytes can promote pond drainage by intensifying transpiration (Andresen and Lougheed, 2015).

The landscapes drain as permafrost thaws because the disappearing ice has been acting as in barrier for the water. Without permafrost, water can better drain subsurface. However, drainage is impeded if the soils have low permeability, such as highly decomposed peat, and ponds and lakes can be sustained (Smith et al., 2005). Though we do not focus on pond formation in MeEP, existing ponds may drain. MeEP includes a simple surface and subsurface flow formulation, which depends on the local permeability (Helbig et al., 2013). In MeEP, pond areas decrease slightly with warming (Fig. C.7). Thus, even in our first-order approximation of pond hydrology, we find evidence of pond drainage reducing pond methane emissions (Fig. C.8), though to a lesser extent than for example Huissteden et al. (2011). They reported that drainage limits water body methane emissions on the landscape scale. The hydrological model implemented in MeEP is one-dimensional and can consequently only provide a first-order estimate of water-table dynamics. More complex dynamics on the landscape scale, such as the formation of a network of channels along the ice wedges promoting fast drainage through percolation (Cresto Aleina et al., 2013). Thus, our estimate of runoff might be too low.

C.5.4 *LANDSCAPE-SCALE IMPACT OF POND METHANE EMISSIONS*

When estimating the landscape-scale impact of methane emissions from ponds and lakes, many studies concentrate on diffusive emissions (Juutinen et al., 2009; Holgerson and Raymond, 2016; Polishchuk et al., 2018; Hughes-Allen et al., 2020; Zabelina et al., 2020), though some also include ebullition (Sepulveda-Jauregui et al., 2015; Wik et al.,

2016; Kuhn et al., 2021). We find that including ebullition is important because, in ponds, ebullition contributes more than diffusion to the total emissions (Kuhn et al., 2021; Praetzel et al., 2021) and becomes still more important with warming (Fig. C.10). In MeEP, ponds are very sensitive to rising temperatures. The model projects emissions to roughly double at a temperature increase of only 2.5 °C (Fig. C.5(B)).

Much of the intensification of methane emissions in MeEP is due to vegetation growth, which leads to a strong boost in mean emissions during the ice-free season and a higher peak of emissions in summer (Fig. C.5(A)). These emissions are already under current climatic conditions notably higher than mean tundra emissions (Fig. C.9) and should be included in future large-scale ponds methane emissions assessments.

We might even underestimate the response of ponds to warming because methane production is described by a q^{10}-equation. This description does not account for shifts in methanogen communities, which can enhance the rate of methanogenesis under warming (Zhu et al., 2020). Additionally, we only account for present-day substrate in the current setup: Methanogenesis is coupled to vegetation productivity of the same year. This assumption is valid for ponds at the moment (Negandhi et al., 2013; Bouchard et al., 2015; Dean et al., 2020), but might change as permafrost degrades and old carbon leeches into the ponds (Langer et al., 2015; Prėskienis et al., 2021). This additional carbon is not included in our projections.

C.6 CONCLUSIONS

While ponds are not hotspots of methane emissions in our study area under the current climate, our model simulations indicate that they will become stronger methane sources under warming. We project an increase of pond methane emissions of 1.08 g CH_4 m^{-2} $year^{-1}$ $°C^{-1}$. This increase corresponds to an emission increase of 180 % in the exp5.0_all simulation compared to the hist_all simulation. At the same time, the pond area decreases only slightly. However, the hydrological module of MeEP only gives a first-order approximation of water-table dynamics. To better gauge the future impact of ponds, we need better projections of pond inception and drainage.

Much of the methane-emission increase from ponds is mediated through macrophytes. The vascular plants become more productive and provide additional substrate for methanogenesis. In our simulations, the impact of the additional substrate on methanogenesis is substantially stronger than the impact of elevated temperatures or a prolonged open-water season. However, the relationship between emergent-macrophyte productivity and methanogenesis in ponds could only be approximated due to a lack of measurement data. We further find that plant-mediated transport is the methane pathway

contributing most to the overall landscape emissions in simulated temperature regimes. Unfortunately, plant-mediated transport is the methane pathway least often reported in measurement datasets of pond methane emissions. This makes it harder to generalize our findings to a larger scale, and more observations of this emissions pathway and its contribution to overall pond methane emissions are needed. Additionally, the current version of MeEP only uses one value for the conductivity of plants, even though we know that different plant species conduct methane with varying efficiency (Knoblauch et al., 2015). To upscale the plant-mediated fluxes realistically, vegetation maps of the dominant macrophytes would be a strong asset. However, we suppose that vegetation similarly impacts ponds in other regions. In that case, it is crucial to include macrophytes as a substrate source and as an efficient methane pathway for a pan-Arctic assessment of pond methane emissions under warming.

C.7 SUPPLEMENT 1: THE METHANE MODULE

C.7.1 SUMMER FLUXES

In ponds, methane (CH_4) is produced in the anoxic bottom sediments when temperatures permit. If the pond is ice-free, this methane evades through three pathways: Diffusion, plant-mediated transport, and ebullition. To model these pathways and the distribution of produced methane between these pathways, we make the following main assumptions:

1. Production and emissions are in equilibrium in each time step and, consequently, the methane concentrations in the water column are stationary. This means that the time-derivatives of the methane concentrations and fluxes are all zero in each time step.
2. There is no lateral mixing of methane between the vegetated part and the open-water part of the pond in summer. Thus, methane transport in both parts of the pond can be treated separately.
3. In summer, the whole water column is well mixed, and the methane concentration throughout the water column is constant.

Following assumption 2, we can model the overgrown and the open-water part of the pond separately. Only for the overgrown fraction plant-mediated transport is considered.

C.7.1.1 METHANE IN THE SEDIMENT

Methane is produced in the sediment, and the production is dependent on the sediment temperature T_b [K] and the base productivity P_0 [mol m^{-3} s^{-1}]. P_0 is a tuning parameter and separately tuned for the

overgrown and open-water parts of the ponds (Ström et al., 2003). We assume that most methane is produced at the top of the sediment ($z = 0$ m), and the productivity reduces exponentially further down the sediment ($z > 0$ m) (Stepanenko et al., 2011):

$$P_{CH_4}(z) = P_0 \cdot e^{-az} \cdot q_{10}^{(T_b - 273.15)/T_{10}} \cdot f_{prod} \qquad [\text{mol m}^{-3}\ \text{s}^{-1}]. \quad \text{(C.6)}$$

q_{10} and T_{10} [C] are constants describing the temperature dependence, while a [m^{-1}] determines how quickly the methane production decreases with sediment depth. Since methane production has been reported to reduce quickly with sediment depth (Knoblauch et al., 2015), we set a to 20 m^{-1} (see Tab.C.8). With f_{prod} we take substrate availability into account. This dimensionless factor is based on Walter et al. (2001) and represents both the productivity of the plants and an estimate for the litter fall: We assume that carbon availability is correlated with the net primary productivity (NPP), and that net primary productivity is roughly half of the gross primary productivity (GPP). Since the methanogens do not use all the substrate within the same time step, we apply a running average on NPP with a window length of one month split methane production into a part dependent on NPP (75%) and into a base productivity (25%) based on findings by Bouchard et al. (2015) and Dean et al. (2020). For the open-water part of the pond, we additionally assume that the carbon availability decreases with the open-water fraction and multiply the NPP-dependent term with $\tanh(A_v/A_o)$, where A_v is the overgrown area of the pond, and A_o is the area of the open-water fraction.

Since the fraction of the sediment where methane is produced is shallow, we can assume a constant temperature in the sediment layer and integrate Eq. C.6 from the top of the sediment ($z = 0$ m) to the bottom of the unfrozen sediment ($z = h_s$) resulting in

$$P_{CH_4} = \frac{P_0}{a} \cdot q_{10}^{(T_b - 273.15)/T_{10}} \cdot (1 - e^{-a h_s}) \cdot f_{prod} \qquad [\text{mol m}^{-2}\ \text{s}^{-1}]. \quad \text{(C.7)}$$

We use Eq. C.7 to simulate the production of methane in the sediment when the temperature in the topsoil exceeds the freezing point. As soon as the sediment freezes, we set the methane production to zero.

The methane fluxes out of the sediment reach their maximum when the methane concentration in the sediment is as high as physically possible. The methane gradient between the sediment and the water column is maximal at this concentration. The saturation concentration is reached when methane starts to gas out and form bubbles. Bubbles forming in the sediment can contain any gas present in the sediment. The most abundant gas in air is nitrogen, so it is also the most abundant gas in the sediment, and, apart from methane, the main constituents of bubbles in the sediment (Walter et al., 2008). Thus, we approximate that the bubbles contain only methane and

nitrogen to derive the saturation concentration. Under this assumption, the concentration of methane is limited by the hydro-static pressure p_h (Pa) and the partial pressure of nitrogen (N_2) (Stepanenko et al., 2011; Bazhin, 2001). To compute the saturation concentration of methane, we assume that N_2 decays exponentially in the sediment and is in equilibrium with the atmosphere in the water column ($c(N_2, z) = c(N_2)_{eq} \cdot e^{-\lambda_{N_2}(z-h_s)}$ [mol m^{-3}]). $c(N_2)_{eq}$ can be computed according to Henry's law, and we define $H_b^{N_2}$ as the temperature-dependent Henry constant for N_2 at sediment temperatures. $H_b^{CH_4}$ [mol m^{-1} Pa^{-1}] signifies the equivalent Henry constant for methane (Sander, 2015). We compute the temperature-dependent Henry constant as follows:

$$H^{\mathbf{gas}} = H_0^{\mathbf{gas}} e^{\tau(1/T - 1/T_0)} \qquad [\text{mol m}^{-3}\ \text{Pa}^{-1}]. \tag{C.8}$$

Another quantity driving the saturation concentration, the hydrostatic pressure is computed as the sum of the air pressure p_a and the pressure exerted by the water column,

$$p_h = p_a + (H \cdot \rho_{aq} \cdot g) \qquad [\text{Pa}]. \tag{C.9}$$

Further, the saturation pressure depends on the porosity of the sediment ϕ [m^3 m^{-3}], which is set based on measurement data (Helbig et al., 2013) and a dimensionless threshold γ. γ is introduced as a correction factor to account for the shape of the bubbles. Henry's law was measured over flat surfaces, but bubbles are spherical (Stepanenko et al., 2011). Due to large uncertainty regarding the true value of γ, γ is tuned. Combining Eq. C.8 and Eq. C.9 with γ and ϕ, we arrive at the following equation for the saturation concentration:

$$c(CH_4)_b^{sat} = \phi \cdot H_b^{CH_4} \cdot \gamma \cdot \left(p_h - \frac{c(N_2)_{eq}}{H_b^{N_2}} \cdot e^{\frac{-\lambda_{N_2} \cdot h_s}{2}} \right) \qquad [\text{mol m}^{-3}]. \tag{C.10}$$

Once this concentration is reached, all additional methane produced in the sediment will change from dissolved to gaseous. Consequently, the concentration in the sediment will not rise further no matter how much additional methane is produced.

C.7.1.2 PLANT-MEDIATED TRANSPORT

Plants can be very efficient in transmitting methane from the sediment to the atmosphere bypassing the water column. If plants are present, plant-mediated transport is often the dominating pathway (Andresen et al., 2016). Thus, out of the three possible pathways, we evaluate the plant-mediated transport first using the approach by Walter et al. (1996). Initially, we compute the rate Q_{plant} with which methane can leave the root zone through the plants as

$$Q_{plant} = d_{veg} \cdot t_{veg} \cdot r \cdot f_{growth} \cdot h_s \cdot c(CH_4)_b^{sat} \qquad [\text{mol m}^{-2}\ \text{s}^{-1}]. \tag{C.11}$$

d_{veg} is a dimensionless factor for the density of the plants, which we set to globally to 0.1 due to lack of data. t_{veg} is another dimensionless factor describing how well the plants conduct methane and is set to 10 based on Walter et al. (2001). r is a rate constant of 0.01 $h^{-1} = 2.7 \cdot 10^{-6}$ s^{-1}. f_{growth} is a dimensionless measure of the plant-growth, varies between zero and four and is based on the leaf-area index. Andresen et al. (2016) found a good agreement between leaf-area index and plant-biomass for the dominant species in Arcitc ponds (*Arctophila fulva* and *Carex aquatilis*). h_s [m] is the depth of the unfrozen sediment, with a maximum thickness of 0.2 m, because deeper sediments produce only very little methane (Knoblauch et al., 2015; Joabsson and Christensen, 2002). Since the plant stems also transport oxygen into the rooting zone, we assume a fixed fraction of the plant-mediated methane to be oxidized ($f_{ox} = 0.2$) reducing the methane flux from plants F_{plant}. The value 0.2 is an conservative estimate based on the work of Turner et al. (2020) and Ström et al. (2005), who measured the oxidation rates of the plant species dominating our study region. The plant-mediated flux then is defines as

$$F_{plant} = (1 - f_{ox}) \cdot \min\{Q_{plant}, P_{CH_4}\} \qquad [\text{mol m}^{-2}\ \text{s}^{-1}]. \quad \text{(C.12)}$$

Since plants, if present, are the most efficient pathway for methane removal from the sediment, we assume that all methane that can be emitted through plants, is emitted through plants. Thus, only excess methane which cannot be emitted through plants is available for the other pathways.

C.7.1.3 DIFFUSION

Since ponds are shallow and well mixed, we assume that the methane concentration in the pond $c(CH_4)_{aq}$ [mol m^{-3}] are constant throughout the water column. This allows us to formulate the following balance of the flux between sediment and water column F_b^{diff} [mol m^{-2} s^{-1}], the flux between water surface and atmosphere F_{diff} [mol m^{-2} s^{-1}], and the oxidation in the water column F_{ox} [mol m^{-2} s^{-1}]:

$$F_b^{diff} - F_{diff} - F_{ox} = 0. \quad \text{(C.13)}$$

Now, we take a look at each of these three fluxes before we subsitute formulations for each back into the balance above.

SEDIMENT-WATER INTERFACE We compute the diffusion from the sediment into the water column according to Fick's law and assuming that the methane concentration in the sediment equals the saturation concentration $c(CH_4)_b^{sat}$ (Eq. C.10),

$$F_b^{diff} = D_{soil} \frac{c(CH_4)_b^{sat} - c(CH_4)_{aq}}{0.5 \cdot h_s} \qquad [\text{mol m}^{-2}\ \text{s}^{-1}], \quad \text{(C.14)}$$

with the diffusion coefficient D_{soil}. This coefficient is computed following Sabrekov et al. (2017) as a combination of liquid and gaseous diffusion as

$$D_{soil} = (\phi - \epsilon_a) D_{aq} + \frac{\epsilon_a \cdot D_{gas}}{H_b^{CH_4} \cdot R \cdot T_b} \qquad [m^2\ s^{-1}]. \tag{C.15}$$

ϵ_a is the gas-filled porosity of the soil. Since this parameter is ill-constrained, it was used as a tuning parameter. R is the ideal gas constant, and the liquid and gaseous diffusion coefficients (D_{aq} and D_{gas}, respectively) are computed as

$$D_{aq} = \tau \cdot (\phi - \epsilon_a) \cdot D_{aq}^0 \cdot ((T_b - 0.15)/298)^{1.82} \qquad [m^2\ s^{-1}], \tag{C.16}$$

$$D_{gas} = D_{gas}^0 \cdot \epsilon_a^{3.3}/\phi^2 \cdot ((T_b - 0.15)/273)^{1.82} \qquad [m^2\ s^{-1}]. \tag{C.17}$$

τ is the dimensionless tortuosity coefficient, T_b [K] is the temperature of the upper sediment, D_{aq}^0 [$m^2\ s^{-1}$] and D_{gas}^0 [$m^2\ s^{-1}$] are reference values for the diffusivity of methane and set according to Arah and Stephen (1998).

WATER-AIR INTERFACE We infer the diffusion from the water column to the atmosphere using the gradient between water and air analogously to the sediment-water interface,

$$F_{diff} = k_p (c(CH_4)_{aq} - c(CH_4)_{aq}^{eq}) \qquad [mol\ m^{-2}\ s^{-1}]. \tag{C.18}$$

$c(CH_4)_{aq}^{eq}$ [mol m^{-3}] represents the methane concentration in equilibrium with the atmosphere, and k_p [m s^{-1}] is the piston velocity, or gas-exchange coefficient. $c(CH_4)_{aq}^{eq}$ is computed using the ideal gas law and Henry's law as

$$c(CH_4)_{aq}^{eq} = f_{CH_4}^{atm} \cdot p_a \cdot H_{aq}^{CH_4}. \tag{C.19}$$

$f_{CH_4}^{atm}$ denotes the fraction of methane in air, $H_{aq}^{CH_4}$ [mol m^{-1} Pa^{-1}] is the temperature-dependent Henry's constant for methane in the water column using the mixed-layer temperature (Sabrekov et al., 2017).

For k_p, we follow the parameterization by Heiskanen et al. (2014),

$$k_p = \frac{\sqrt{(c_1 \cdot u)^2 + (c_2 \cdot w_{dd})^2}}{\sqrt{S}} \qquad [m\ s^{-1}]. \tag{C.20}$$

c_1 and c_2 are dimensionless constants, which were tuned to data of larger lakes in the original paper. So we use them as tuning variables. u [m s^{-1}] is the wind speed, which is a forcing variable, and w_{dd} [m s^{-1}] is the Deardoff velocity computed using FLake. Lastly, S is the dimensionless Schmidt number, which we compute following Wanninkhof (2014, 1992),

$$S = c_1^S + c_2^S \cdot T_{ml} + c_3^S \cdot T_{ml}^2 + c_4^S \cdot T_{ml}^3 + c_5^S \cdot T_{ml}^4. \tag{C.21}$$

c_1^S to c_5^S are empirically determined constants, T_{ml} [K] is the mixed-layer temperature provided by FLake.

OXIDATION IN THE WATER COLUMN For F_{ox} we assume that the water oxygen concentration is in equilibrium with the atmosphere and compute $c(O_2)_{aq}$ in the same manner as $c(CH_4)^{eq}_{aq}$,

$$c(O_2)_{aq} = f^{atm}_{O_2} \cdot p_a \cdot H^{O_2}_{aq} \qquad [\text{mol m}^{-3}]. \tag{C.22}$$

Then we use the Michaelis-Menthen relation to compute the oxidation,

$$F_{ox} = V_{max} \cdot H \, \frac{c(O_2)_{aq}}{k_{O_2} + c(O_2)_{aq}} \, \frac{c(CH_4)_{aq}}{k_{CH_4} + c(CH_4)_{aq}} \qquad [\text{mol m}^{-2}\ \text{s}^{-1}]. \tag{C.23}$$

V_{max} [mol m^{-3} s^{-1}], k_{CH_4} [mol m^{-3}] and k_{O_2} [mol m^{-3}] are constants and set based on a study by Martinez-Cruz et al. (2015) focusing on Alaskan lakes.

METHANE CONCENTRATION IN THE MIXED LAYER We can now substitute the fluxes (eq. (C.14), (C.18), and (C.23)) into the balance (eq. C.13). This leads to an quadratic equation of $c(CH_4)_{aq}$ which we can solve analytically and arrive at the following expression for $c(CH_4)_{aq}$:

$$c(CH_4)_{aq} = \frac{c + \sqrt{c^2 + 4k_{CH_4} \cdot a \cdot b)}}{2b} \qquad [\text{mol m}^{-3}], \tag{C.24}$$

$$a = \frac{1}{H \cdot k_{ox}} \left(\frac{D_{soil} \cdot c(CH_4)^{eq}_{aq}}{0.5 h_s} + k_p \cdot c(CH_4)^{sat}_{b} \right) \qquad [\text{ - }], \tag{C.25}$$

$$b = \frac{1}{H \cdot k_{ox}} \left(\frac{D_{soil}}{0.5 h_s} + k_p \right) \qquad [\text{m}^3\text{mol}^{-1}], \tag{C.26}$$

$$c = a - k_{CH_4} \cdot b - 1 \qquad [\text{ - }]. \tag{C.27}$$

k_{ox} denote the part of the Michaelis-Menten relation which does not depend on CH_4,

$$k_{ox} = V_{max} \, \frac{c(O_2)_{aq}}{k_{O_2} + c(O_2)_{aq}} \qquad [\text{mol m}^{-3}\ \text{s}^{-1}]. \tag{C.28}$$

Once we obtained $c(CH_4)_{aq}$, we can compute the flux from the sediment and compare this potential diffusive flux with the methane production to compute the diffusive flux from the sediment into the waterbody (Eq. C.14) as

$$F^{diff}_{b} = \min\{P_{CH_4} - F_{plant}, F^{diff}_{b}\}. \tag{C.29}$$

In case the F^{diff}_{b} computed using Eq. C.14 is larger than the remaining methane in the atmosphere ($P_{CH_4} - F_{plant}$), we solve Eq. C.13 again

for $c(CH_4)_{aq}$ again, this time with the boundary condition $F_b^{diff} = P_{CH_4} - F_{plant}$. This, then, results in

$$c(CH_4)_{aq} = \frac{a + \sqrt{a^2 + b}}{2k_p} \qquad [\text{mol m}^{-3}], \tag{C.30}$$

$$a = k_p(c(CH_4)_{aq}^{eq} - k_{CH_4}) - H \cdot k_{ox} + F_b^{diff} \qquad [\text{mol m}^{-2}\ \text{s}^{-1}], \tag{C.31}$$

$$b = 4k_p \cdot k_{CH_4}(k_p \cdot c(CH_4)_{aq}^{eq} + F_b^{diff}) \qquad [\text{mol}^2\text{m}^{-4}\ \text{s}^{-2}]. \tag{C.32}$$

Finally, we can substitute either the result of eq. C.24 or eq. C.30 into eq. C.18 and obtain the diffusive flux from the pond to the atmosphere.

C.7.1.4 EBULLITION

The third and last pathway of methane from the sediment to the atmosphere is ebullition. We assumed that plant-mediated transport is the fastest pathway of methane and computed that flux first. With the methane left in the sediment ($P_{CH_4} - F_{plant}$), we computed the diffusive flux between water and atmosphere F_{diff} and the diffusive flux between sediment and water F_b^{diff}. Since we assume that production and emission are in equilibrium, all the methane that is still left in the sediment and not emitted through diffusion or plants is emitted through ebullition,

$$F_{ebul} = P_{CH_4} - F_{plant} - F_b^{diff} \qquad [\text{mol m}^{-2}\ \text{s}^{-1}]. \tag{C.33}$$

C.7.2 WINTER FLUXES

C.7.2.1 ICE-COVERED PONDS

Once ice has formed on the pond, we assume there is no gas exchange between water and atmosphere, so all fluxes to the atmosphere are set to zero. This means that there is also no plant-mediated transport, which was the mechanism setting the overgrown part of the pond apart from the open-water part. So instead of treating the overgrown and open-water fractions of the pond separately, we can simulate them together in winter. We merge the two parts weighted by their area fraction for the methane production in the sediment and methane concentration in the water column. We take the deeper water column height as the water column height for the merged computation. As the ice layer grows, we assume that all soluble gases that were dissolved in the freshly frozen water are expelled into the underlying water column. In the same manner methane and oxygen concentrations in water are diluted when ice melts,

$$c(\mathbf{gas})(t) = \frac{H_{aq} + \Delta_{ice}}{H_{aq}}\, c(\mathbf{gas})(t-1), \tag{C.34}$$

where **gas** stands for either oxygen or methane, and H_{aq} the height of the unfrozen water column. t is the time step and $\Delta_{ice} = h_{ice}(t) - h_{ice}(t-1)$ is the change in ice thickness, with a positive sign indicating ice growth.

Since the pond cools down from the top, sediment temperatures are still above freezing when ice forms in fall. Thus, methane is still produced in fall until sediment temperatures drop to zero, and there is still a methane flux from the sediment into the water column. Thus, all the methane produced in a time step (see eq. (C.7)) is added to the water column,

$$c(CH_4)_{aq}(t) = c(CH_4)_{aq}(t) + P_{CH_4} \frac{t_s}{H_{aq}} \qquad [\text{mol m}^{-3}], \quad \text{(C.35)}$$

with t_s being the time step length. Since the methane cannot be emitted to the atmosphere, it accumulates in the water column where a part of the methane is oxidized with the remaining dissolved oxygen. If the methane concentration exceeds a threshold $c(CH_4)^{sat}_{aq}$, it changes its state from dissolved to gaseous, equivalently to the processes in the sediment. The position where the bubbles are most likely to form is directly under the ice, because the hydrostatic pressure is lowest there. We compute the saturation pressure analogously to the equilibrium pressure in summer (eq. C.19), but instead of using the partial pressure of methane, we use the hydrostatic pressure

$$p_{hyd} = p_a + \rho_{ice}\, g\, h_{ice} \qquad [\text{Pa}]. \quad \text{(C.36)}$$

Using Henry's law, we compute the saturation pressure of methane under ice as

$$c(CH_4)^{sat}_{aq} = p_{hyd} \cdot H^{CH_4}_{aq} \qquad [\text{mol m}^{-3}]. \quad \text{(C.37)}$$

We assume that only the dissolved methane reacts with the oxygen in the water and introduce a storage term S_{CH_4} [mol m^{-2}] for gaseous methane under ice. If the methane concentration in the water column exceeds $c(CH_4)^{sat}_{aq}$, methane gasses out until $c(CH_4)_{aq} = c(CH_4)^{sat}_{aq}$.

After balancing S_{CH_4} and $c(CH_4)_{aq}$, we determine how much methane is oxidized in the current time step. To do so, we need to compute the concentration of oxygen under ice, which we prescribe (Huang et al., 2021) as

$$c(O_2)(t) = \max\{0.0, c(O_2)(t-1) - 1.447 \cdot 10^{-7} \cdot t_s\} \qquad [\text{mol m}^{-3}]. \quad \text{(C.38)}$$

We solve the full Michaelis-Menten equation in each time step to estimate how much methane oxidised,

$$\Delta_{ox} = V_{max} \frac{c(O_2)}{k_{O_2} + c(O_2)} \frac{c(CH_4)_{aq}}{k_{CH_4} + c(CH_4)_{aq}} \cdot t_s \qquad [\text{mol m}^{-3}], \quad \text{(C.39)}$$

and reduce methane and the oxygen concentrations in the water accordingly,

$$c(CH_4)_{aq} = c(CH_4)_{aq} - \min\{\Delta_{ox},\ c(CH_4)_{aq},\ c(O_2)/2\}, \quad \text{(C.40)}$$

$$c(O_2)_{aq} = c(O_2)_{aq} - 2 \cdot \min\{\Delta_{ox},\ c(CH_4)_{aq},\ c(O_2)/2\}. \quad \text{(C.41)}$$

Next, we balance S_{CH_4} and $c(CH_4)_{aq}$ again.

In case the whole water column is frozen, all produced methane is directly added to the storage term S_{CH_4}

C.7.2.2 SPRING FLUSH

Once the ice on the pond has melted, we emit the methane accumulated under the ice to the atmosphere. Since we assume an equilibrium between emission and production of methane in the open-water season, we emit all the accumulated methane in the first time step of open water. All the methane stored in gas-form S_{CH_4} is immediately released through ebullition. Furthermore, we emit the methane, which was dissolved in the water and led to elevated dissolved methane concentration, compared to the open-water case. This dissolved methane is added to the diffusive flux,

$$F_{diff} = F_{diff} + \frac{H_{aq}}{t_s}(c(CH_4)_{aq}(t-1) - c(CH_4)_{aq}(t)) \qquad [\text{mol m}^{-2}\ \text{s}^{-1}]. \quad \text{(C.42)}$$

C.8 SUPPLEMENT 2: THE HYDROLOGY MODULE

In the hydrology module, we compute water-table dynamics throughout the year. To cater to the separation of the open-water and overgrown parts of the pond in the methane module, we set a fraction of the pond to be overgrown and a fraction to be open water based on a maximum water depths for plants. In other words, we assume that vascular plants grow in the shallow parts of the ponds, up to a default depths of 0.5 m. The depths can be set at the beginning of each model run. Any deeper part of a pond consists of open water. The module computes the mean depths of each fraction as well as the area they cover on the premise that the ponds are circular and the cross-section of an isosceles trapezoid (Fig. C.11). After the pond has been divided into the open-water and vegetated parts during initialization, the diameter of the open-water fraction of the pond is kept constant throughout the whole simulation.

C.8.1 INITIALIZATION

To initialize a pond, the user has to set the angle of the rim α (see Fig. C.11), the initial depth H_{aq} [m] and the area of the pond. The

Table C.6: Input variables for the methane module of MeEP

NAME	UNIT	DESCRIPTION	SOURCE
H	m	Mean water depth of open-water and overgrown pond fraction	Hydrology module
A	m^2	Mean area of open-water and overgrown pond fraction	Hydrology module
h_s	m	Thickness of unfrozen bottom sediment layer	Soil module
w_{dd}	$m\ s^{-1}$	Convective Deardorff velocity scale in the mixed layer	Flake
u^*	$m\ s^{-1}$	Friction velocity scale in the mixed layer	Flake
p_a	Pa	Atmospheric pressure at the surface	ERA-5
T_{ml}	K	Mixed-layer temperature	Flake
T_b	K	Sediment temperature	Soil module
t	s	Time-step length	User choice
h_{ice}	m	Thickness of ice	Flake
Δ_{ice}	m	Change in hice since last time step	Flake
$c(CH_4)_{aq}$	$mol\ m^{-3}$	Methane concentration in the mixed layer of prior time step	Methane module
$c(O_2)_{aq}$	$mol\ m^{-3}$	Oxygen concentration in the mixed layer of prior time step	Methane module
S_{CH_4}	$mol\ m^{-2}$	Methane stored under ice in winter	Methane module
ρ	-	Porosity of the sediment	User choice
f_{growth}	-	Approximation of plant growth using the leaf-area index	MODIS
f_{prod}	$mol\ m^{-2}$	Net primary production and litter fall approximation	MODIS

Table C.7: Tuning parameters for the methane module of MeEP

NAME	VALUES	UNIT	DESCRIPTION
P_0^{veg}	0.72	$\mu mol\ m^{-3}\ s^{-1}$	base productivity in vegetated pond fraction
P_0^{ow}	0.42	$\mu mol\ m^{-3}\ s^{-1}$	base productivity in vegetated pond fraction
γ	0.42	-	bubble-shape correction factor
ϵ_a	0.059	$m^3\ m^{-3}$	gas-filled porosity of sediment
c_1	$8 \cdot 10^{-6}$	-	weight of wind speed in k_p computation
c_2	0.015	-	weight of Deardoff velocity in k_p computation

Table C.8: Constants used in the methane module of MeEP

NAME	VALUE	UNIT	DESCRIPTION	EQUATION
a	20	m^{-1}	depth dep. of CH_4 production	1,2
T_{10}	10	°C	reference temp.	1,2
q_{10}	2	-	temp. dep. of CH_4 production	1,2
λ_{N_2}	5	-	depth dep. of N_2 sediment conc.	5
$H_0^{CH_4}$	$1.4 \cdot 10^{-5}$	mol m^{-3} Pa^{-1}	Henry's const. for CH_4	3
$H_0^{O_2}$	$1.3 \cdot 10^{-5}$	mol m^{-3} Pa^{-1}	Henry's const. for O_2	3
$H_0^{N_2}$	$6.4 \cdot 10^{-6}$	mol m^{-3} Pa^{-1}	Henry's const. for N_2	3
$\tau_0^{CH_4}$	1600	K	temp. dep. of Henry's const. for CH_4	3
$\tau_0^{O_2}$	1500	K	temp. dep. of Henry's const. for O_2	3
$\tau_0^{N_2}$	1300	K	temp. dep. of Henry's const. for N_2	3
T_0	25	°C	reference temp.	3
ρ_{aq}	1000	kg m^{-3}	water density	4
g	9.91	m s^{-1}	gravitational acceleration	4, 30
d_{veg}	0.1	-	density of plants	6
t_{veg}	10	-	gas-conducting properties of plants	6
r	$2.7 \cdot 10^{-6}$	s^{-1}	rate const.	6
f_{ox}	0.2	-	oxidised fraction of Q_{plant}	7
R	8.3144598	m^3 Pa K^{-1} mol^{-1}	ideal gas const.	11
τ	0.66	-	tortuosity coeff.	11
D_{aq}^0	$1.5 \cdot 10^{-9}$	m^2 s^{-1}	CH_4 diff. coeff. in the water at 25 °C	11
D_{gas}^0	$1.889 \cdot 10^{-5}$	m^2 s^{-1}	CH_4 diff. coeff. in the air at 0 °C	12
$f_{CH_4}^{atm}$	$1.9499 \cdot 10^{-9}$	-	fraction of CH_4 in atmosphere	15
$f_{N_2}^{atm}$	0.496	-	fraction of N_2 in atmosphere	5
$f_{O_2}^{atm}$	0.19	-	fraction O_2 in atmosphere	18
c_1^S	1909.4	-	empirical const. for Schmidt num.	17
c_2^S	-120.78	$°C^{-1}$	empirical const. for Schmidt num.	17
c_3^S	4.1555	$°C^{-2}$	empirical const. for Schmidt num.	17
c_4^S	-0.080578	$°C^{-3}$	empirical const. for Schmidt num.	17
c_5^S	0.00065777	$°C^{-4}$	empirical const. for Schmidt num.	17
k_{CH_4}	0.006875	mol m^{-3}	half-saturation const. of CH_4	19,20,23, 35
k_{O_2}	0.0195	mol m^{-3}	half-saturation const. of O_2	19,24, 35
V_{max}	$1.412 \cdot 10^{-7}$	mol m^{-3} s^{-1}	maximum methane oxidation rate	19,24
ρ_{ice}	920	kg m^{-3}	ice density	30
t_s	3600	s	model time-step length	33,35, 38

coeff, coefficient; conc, concentration; const, constant; dep, dependence; diff, diffusion; num, number; temp, temperature.

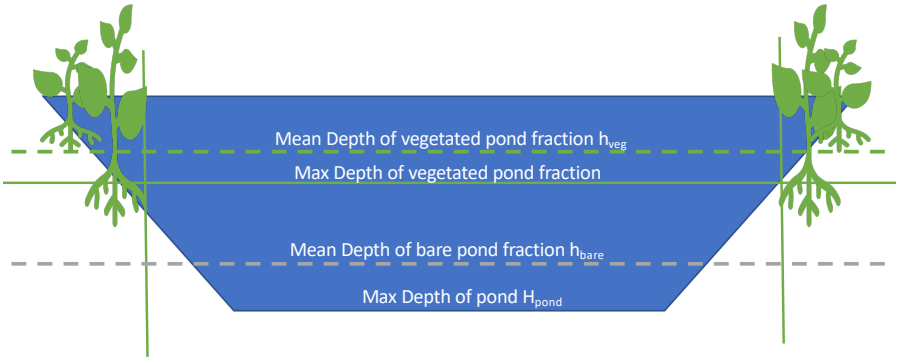

Figure C.11: The pond cross-section is assumed to have the shape of an isosceles trapezoid. Plants only grow up to a specific depth (maximum depth of the vegetated pond fraction). For the physical pond model FLake, the maximum depth of the pond is used H_{pond}, which the methane module distinguishes between the vegetated and the open-water part of the pond.

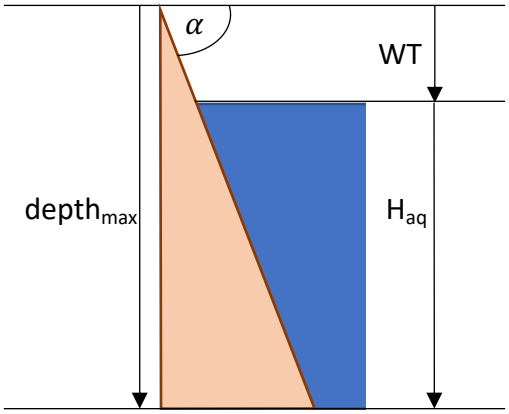

Figure C.12: The water table is measured from the highest point of the rim. If the water table is zero, the water depths reaches it's maximum.

maximum depth of the pond, before water would overflow, is set to $depth_{max} = H_{aq} + 0.1$ m. The maximum depth at which plants can grow h_{veg} can be adjusted and has a default of 0.5 m. With h_{veg} [m] the area A [m^2] of the pond is split between an open-water part A_o [m^2] and a vegetated part A_v [m^2]. If H_{aq} is smaller than 0.5 m, the whole pond is vegetated ($A_v = A$ and $A_o = 0$ m^2). Otherwise, we compute the area of the open-water part using the assumption that the ponds are circular. The width of the vegetated outer circle R_v [m] can be inferred from α and h_{veg},

$$R_v = \frac{h_{veg}}{\tan(\alpha)} \quad [m]. \tag{C.43}$$

Then, we subtract R_v from the radius of the whole pond which gives us the radius of the open-water area. With the radii we compute the areas as

$$R = \sqrt{\frac{A}{\pi}} \qquad [m], \tag{C.44}$$

$$A_o = \pi (R - R_v)^2 \qquad [m^2], \tag{C.45}$$

$$A_v = A - A_o \qquad [m^2], \tag{C.46}$$

where R is the radius of the whole pond. To compute the mean depth of the open-water and the vegetated part of the pond, we compute the volumes of the flat middle part of the pond, and the part of the pond where the water depth increases. The middle part has the shape of a cylinder and can be determined as

$$R_{mid} = R - \frac{H_{aq}}{\tan(\alpha)} \qquad [m], \tag{C.47}$$

$$V_{mid} = \pi \cdot R_{mid}^2 \cdot H_{aq} \qquad [m^3]. \tag{C.48}$$

$$\tag{C.49}$$

The outer part can be computed as the volume of a truncated cone minus V_{mid},

$$V_{edge} = \pi \frac{\tan(\alpha)}{3} (R^3 - 3R \cdot R_{mid}^2 + 2R_{mid}^3) \qquad [m^3]. \tag{C.50}$$

We can then compute the volume of the vegetated pond fraction, either as the whole volume of the pond, or as another hollow, truncated cone,

$$V_v[m^3] = \begin{cases} V_{edge} + V_{mid}, & h_{veg} \leqslant H_{aq} \\ \pi \frac{\tan(\alpha)}{3} (R^3 - 3RR_o^2 + 2R_o^3), & \text{else,} \end{cases} \tag{C.51}$$

with $V_o = R - R_v$ the radius of the open-water part of the pond. All the leftover volume of the pond is then attributed to the open-water part.

Finally, we can compute the mean depths of the pond fractions,

$$\overline{h_{o/v}} = \frac{V_{o/v}}{A_{o/v}} \qquad [m]. \tag{C.52}$$

C.8.1.1 POLYGONAL TUNDRA OF SAMOYLOV ISLAND

As an example study site, the ponds can be constructed to represent the three pond types of the polygonal tundra of Samoylov Island. We use a landcover classification to determine the average size of the respective pond type as well as their average vegetated fraction and use the ratio between the open-water and overgrown fraction of the ponds to infer α. For pond depths, we use the averages of measurements done by Rehder et al. (2021). The results are listed in table C.9.

POND TYPE	MEAN AREA $[m^2]$	DEPTH [m]	α [RAD]
polygonal-center pond	89	0.6	0.3
ice-wedge pond	276	0.8	0.2
merged polygonal pond	2682	1.2	0.055

Table C.9: Input values to initialize typical ponds of the polygonal tundra in the Lena River Delta.

C.8.2 WATER TABLE DYNAMICS

At the beginning of each time step, we add precipitation and evaporation to the water table,

$$WT(t+1) = WT(t) - P + E \qquad [m]. \tag{C.53}$$

If this leads to an overflow of the pond, we first compute the surface runoff, Q_s, following Gao et al. (2010),

$$Q_s = \min\{\Delta_z, 5.67\frac{1}{s}\Delta_z^{3/2}\frac{t_s}{\sqrt{A}}\} \qquad [m], \tag{C.54}$$

where $\Delta_z = -WT(t+1)$ represents the height of the water over the theoretical maximum height. If the water table closer to the surface than the thaw depths of the surrounding tundra ($WT(t+1) < TD$), water also runs off below ground. This below-ground runoff Q_b is computed based on Darcy's law as

$$Q_b = KA_c\frac{\Delta_z}{\Delta_x}t_s \qquad [m]. \tag{C.55}$$

K [m s^{-1}] indicates the hydraulic conductivity, A_c [m^2] is the area through which the water flows. Δ_x is the distance the water flows through in the porous medium, set to 2m as a characteristic width of a polygonal rim. Δ_z [m] is the height of the water flow and here refers to $TD - WT(t+1)$, where TD is the thaw depth.

K was computed based on measurements by Helbig et al. (2013). They measured the hydrological conductivity on Samoylov Island, Lena River Delta, at different sites. Using the mean of all their measurements, we parameterized an average depth profile of the hydraulic conductivity. With this profile, we compute the hydrological conduc-

tivity between TD and $WT(t+1)$ and use the mean K of this profile for further computations,

$$N = \left\lceil \frac{\Delta_z}{0.002\text{m}} \right\rceil, \tag{C.56}$$

$$z(n) = WT(t+1) + 0.002\text{m} \cdot n, \quad n = 0...N, \tag{C.57}$$

$$K = \frac{1}{N} \sum_{n=0}^{N} 2.5 \cdot 10^{-4} \frac{\text{m}}{\text{s}} \left(1 + \tanh\left(\frac{0.052\text{m} - z(n)}{0.023\text{m}}\right)\right). \tag{C.58}$$

Then, we compute A_c as the lateral surface of a cylinder,

$$A_c = 2\Delta_z \cdot \sqrt{\pi \cdot A} \qquad [\text{m}^2]. \tag{C.59}$$

Finally, the water table is adjusted for the total runoff,

$$WT(t+1) = WT(t+1) + Q_s + Q_b \qquad [\text{m}]. \tag{C.60}$$

C.8.3 RECALCULATING MEAN WATER DEPTHS

With water table changes, the mean water depth of the overgrown and open-water fraction of the pond change as well as the pond area. Since we account for the inclination of the shoreline, the mean water depth does not necessarily change proportionally to the water table. So we recalculate the mean water depth for both parts of the pond. The radius of the pond changes by

$$\Delta_R = \frac{WT(t) - WT(t+1)}{\tan(\alpha)} \qquad [\text{m}]. \tag{C.61}$$

This leads to an areal change of the pond area,

$$A(t+1) = \pi \left(\sqrt{\frac{A(t)}{\pi}} + \Delta_R\right)^2 \qquad [\text{m}^2] \tag{C.62}$$

Since the vegetated part of the pond surrounds the open-water part, the area of the open-water part only changes after the whole vegetated area is above the water table. Thus, we can compute the new areas of the two pond fractions in the following way:

$$A_v(t+1) = \max\{0, A_v(t) + A(t+1) - A(t)\}, \qquad [\text{m}^2], \tag{C.63}$$

$$A_o(t+1) = A(t+1) - A_v(t+1) \qquad [\text{m}^2]. \tag{C.64}$$

Now we compute the changes in the mean water depths for different cases.

CASE $\mathbf{A_o(t+1) = A_o(t) > 0}$

In this case, the water table change of the open-water part is proportional the the water table change of the whole pond,

$$\overline{h_o(t+1)} = \overline{h_o(t)} + WT(t) - WT(t+1) \qquad [m]. \tag{C.65}$$

If $A_v(t+1) > 0$ m, then we can recompute the volume of the vegetated pond fraction in time step $t+1$ as a hollow, truncated cone (see eq. C.51) and divide by the updated area $A_v(t+1)$ (eq. C.52).

CASE $\mathbf{A_o(t+1) \neq A_o(t)}$ AND $\mathbf{A_o(t+1) > 0}$

If the volume of the open-water part changes, we compute the total volume changes of the pond,

$$\Delta_V = \pi \frac{\tan(\alpha)}{3} \left(R(t+1)^3 - R(t)^3 \right) \qquad [m^3]. \tag{C.66}$$

If the water table fell below the vegetated part of the pond, then $\overline{h_v(t+1)} = 0$ and we can compute the new mean depths of the open-water part using the volume change,

$$\overline{h_o(t+1)} = \frac{A_o(t) \cdot \overline{h_o(t)} + \Delta_V}{A_o(t+1)} \qquad [m]. \tag{C.67}$$

If both the vegetated and open-water areas changed, we could compute the volume change over the vegetated part as a hollow, truncated cone. The cone spans from the largest extent of the pond in the two time steps to the largest extend of the open-water fraction of the pond, because this is where the vegetated part starts,

$$R_{min} = \sqrt{\frac{\max\{A_o(t), A_o(t+1)\}}{\pi}} \qquad [m], \tag{C.68}$$

$$R^{max} = \sqrt{\frac{\max\{A(t), A(t+1)\}}{\pi}} \qquad [m], \tag{C.69}$$

$$\Delta_{V_v} = \operatorname{sgn}(A(t+1) - A(t)) \cdot \pi \frac{\tan(\alpha)}{3}, \tag{C.70}$$

$$\cdot (R_{max}^3 - 3R_{max} \cdot R_{min}^2 + 2R_{min}^3) \qquad [m^3]. \tag{C.71}$$

The mean depth can then be computed as the volume of each part in the new time step divided by the area,

$$\overline{h_v(t+1)} = \frac{\overline{h_v(t)} \cdot A_v(t) + \Delta_{V_v}}{A_v(t+1)} \qquad [m], \tag{C.72}$$

$$\overline{h_o(t+1)} = \frac{\overline{h_o(t)} \cdot A_o(t) - \Delta_{V_v} + \Delta_V}{A_o(t+1)} \qquad [m]. \tag{C.73}$$

CASE $\mathbf{A_o(t) = 0}$

If the whole pond is vegetated, all changes in water depths translate to changes in the vegetated pond fraction. We again compute the volume change as in eq. (C.66) and compute the new mean depth analogously to Eq. (C.67).

Finally, we now have computed the new $\overline{h_{o/v}}(t+1)$, the area of the whole pond, and the area of the vegetated and overgrown part of the pond, as well as the new water table.

BIBLIOGRAPHY

Aben, R. C. H. et al. (2017). "Cross continental increase in methane ebullition under climate change." In: *Nature Communications* 8, 1682. ISSN: 2041-1723. DOI: 10.1038/s41467-017-01535-y.

Abnizova, A., J. Siemens, M. Langer, and J. Boike (2012). "Small ponds with major impact: The relevance of ponds and lakes in permafrost landscapes to carbon dioxide emissions." In: *Global Biogeochemical Cycles* 26.2, GB2041. ISSN: 0886-6236. DOI: 10.1029/2011GB004237.

Ahlenius, H. (2016). *Permafrost extent in the Northern Hemisphere*. Global Outlook for Ice and Snow. https://www.grida.no/resources/5234.

Anderson, L., J. Birks, J. Rover, and N. Guldager (2013). "Controls on recent Alaskan lake changes identified from water isotopes and remote sensing." In: *Geophysical Research Letters* 40.13, 3413–3418. ISSN: 0094-8276. DOI: 10.1002/grl.50672.

Anderson, N. J., R. Harriman, D. B. Ryves, and S. T. Patrick (2001). "Dominant factors controlling variability in the ionic composition of West Greenland Lakes." In: *Arctic Antarctic and Alpine Research* 33.4, 418–425. ISSN: 1523-0430. DOI: 10.2307/1552551.

Andresen, C. G. and V. L. Lougheed (2015). "Disappearing Arctic tundra ponds: Fine-scale analysis of surface hydrology in drained thaw lake basins over a 65 year period (1948-2013)." In: *Journal of Geophysical Research-Biogeosciences* 120.3, 466–479. ISSN: 2169-8953. DOI: 10.1002/2014jg002778.

Andresen, C. G., M. J. Lara, C. E. Tweedie, and V. L. Lougheed (2016). "Rising plant-mediated methane emissions from arctic wetlands." In: *Global Change Biology* 23.3, 1128–1139. ISSN: 1354-1013. DOI: 10.1111/gcb.13469.

Arah, J. R. M. and K. D. Stephen (1998). "A model of the processes leading to methane emission from peatland." In: *Atmospheric Environment* 32.19, 3257–3264. ISSN: 1352-2310. DOI: 10.1016/S1352-2310(98)00052-1.

Arp, C. D., B. M. Jones, Z. Lu, and M. S. Whitman (2012). "Shifting balance of thermokarst lake ice regimes across the Arctic Coastal Plain of northern Alaska." In: *Geophysical Research Letters* 39.16. ISSN: 0094-8276. DOI: 10.1029/2012GL052518.

Barton, N. P. and D. E. Veron (2012). "Response of clouds and surface energy fluxes to changes in sea-ice cover over the Laptev Sea (Arctic Ocean)." In: *Climate Research* 54.1, 69–84. ISSN: 0936-577X. DOI: 10.3354/cr01101.

Bastviken, D., J. Cole, M. Pace, and L. Tranvik (2004). "Methane emissions from lakes: Dependence of lake characteristics, two regional assessments, and a global estimate." In: *Global Biogeochemical Cycles* 18.4. ISSN: 0886-6236. DOI: 10.1029/2004gb002238.

Bazhin, N. M. (2001). "Gas transport in a residual layer of a water basin." In: *Chemosphere - Global Change Science* 3.1, 33–40. ISSN: 1465-9972. DOI: 10.1016/S1465-9972(00)00041-6.

Beckebanze, L., Z. Rehder, D. Holl, C. Mirbach, C. Wille, and L. Kutzbach (2021a). "Small waterbodies reduce the carbon sink of a polygonal tundra landscape." In: *Biogeosciences Discuss.* 2021, 1–25. ISSN: 1810-6285. DOI: 10.5194/bg-2021-212.

Beckebanze, L., Z. Rehder, R. Norman, D. Holl, C. Mirbach, C. Wille, and L. Kutzbach (2021b). "Eddy-covariance and meteorological measurements of large pond and polygonal tundra in Lena River Delta, Siberia (summer 2019)." In: PANGAEA. DOI: 10.1594/PANGAEA.937594.

Bekryaev, R. V., I. V. Polyakov, and V. A. Alexeev (2010). "Role of Polar Amplification in Long-Term Surface Air Temperature Variations and Modern Arctic Warming." In: *Journal of Climate* 23.14, 3888–3906. ISSN: 0894-8755. DOI: 10.1175/2010jcli3297.1.

Bhatt, U. S., D. A. Walker, M. K. Raynolds, P. A. Bieniek, H. E. Epstein, J. C. Comiso, J. E. Pinzon, C. J. Tucker, and I. V. Polyakov (2013). "Recent Declines in Warming and Vegetation Greening Trends over Pan-Arctic Tundra." In: *Remote Sensing* 5.9, 4229–4254. ISSN: 2072-4292. DOI: 10.3390/rs5094229.

Boehrer, B. and M. Schultze (2008). "Stratification of lakes." In: *Reviews of Geophysics* 46.2. ISSN: 8755-1209. DOI: 10.1029/2006RG000210.

Bogard, M. J., P. A. del Giorgio, L. Boutet, M. C. G. Chaves, Y. T. Prairie, A. Merante, and A. M. Derry (2014). "Oxic water column methanogenesis as a major component of aquatic CH_4 fluxes." In: *Nature Communications* 5, 5350. ISSN: 2041-1723. DOI: 10.1038/ncomms6350.

Boike, J. et al. (2013). "Baseline characteristics of climate, permafrost and land cover from a new permafrost observatory in the Lena River Delta, Siberia (1998-2011)." In: *Biogeosciences* 10.3, 2105–2128. ISSN: 1726-4170. DOI: 10.5194/bg-10-2105-2013.

Boike, J. et al. (2019). "A 16-year record (2002–2017) of permafrost, active-layer, and meteorological conditions at the Samoylov Island Arctic permafrost research site, Lena River delta, northern Siberia: an opportunity to validate remote-sensing data and land surface, snow, and permafrost models." In: *Earth Syst. Sci. Data* 11.1, 261–299. ISSN: 1866-3516. DOI: 10.5194/essd-11-261-2019.

Boike, J., C Georgi, G Kirilin, S. Muster, K. Abramova, I. Fedorova, A. Chetverova, M. N. Grigoriev, N. Bornemann, and M. Langer (2015a). "Temperature, water level and bathymetry of thermokarst lakes in the continuous permafrost zone of northern Siberia - Lena River Delta, Siberia." In: PANGAEA. DOI: 10.1594/PANGAEA.846525.

Boike, J., M. Grüber, M. Langer, K. Piel, and M. Scheritz (2012). "Orthomosaic of Samoylov Island, Lena Delta, Siberia." In: PANGAEA. DOI: 10.1594/PANGAEA.786073.

Boike, J., G. Veh, G. Stoof, M. Grüber, M. Langer, and S. Muster (2015b). "Visible and near-infrared orthomosaic and orthophotos of Samoylov Island, Siberia, summer 2008, with links to data files." In: PANGAEA. DOI: 10.1594/PANGAEA.847343.

Boike, J., G. Veh, L.-K. Viitanen, N. Bornemann, G. Stoof, and S. Muster (2015c). "Visible and near-infrared orthomosaic of Samoylov Island, Siberia, summer 2015 (5.3 GB)." In: PANGAEA. DOI: 10.1594/PANGAEA.845724.

Boike, J. et al. (2019). "Meteorologic data at station Samoylov (2002-2018, level 2, version 201908), link to archive." In: PANGAEA. DOI: 10.1594/PANGAEA.905232.

Borrel, G., D. Jezequel, C. Biderre-Petit, N. Morel-Desrosiers, J. P. Morel, P. Peyret, G. Fonty, and A. C. Lehours (2011). "Production and consumption of methane in freshwater lake ecosystems." In: *Research in Microbiology* 162.9, 832–847. ISSN: 0923-2508. DOI: 10.1016/j.resmic.2011.06.004.

Bouchard, F., D. Fortier, M. Paquette, V. Boucher, R. Pienitz, and I. Laurion (2020). "Thermokarst lake inception and development in syngenetic ice-wedge polygon terrain during a cooling climatic trend, Bylot Island (Nunavut), eastern Canadian Arctic." In: *The Cryosphere* 14.8, 2607–2627. ISSN: 1994-0424. DOI: 10.5194/tc-14-2607-2020.

Bouchard, F., I. Laurion, V. Prėskienis, D. Fortier, X. Xu, and M. J. Whiticar (2015). "Modern to millennium-old greenhouse gases emitted from ponds and lakes of the Eastern Canadian Arctic (Bylot Island, Nunavut)." In: *Biogeosciences* 12.23, 7279–7298. ISSN: 1726-4189. DOI: 10.5194/bg-12-7279-2015.

Bring, A., I. Fedorova, Y. Dibike, L. Hinzman, J. Mard, S. H. Mernild, T. Prowse, O. Semenova, S. L. Stuefer, and M.-K. Woo (2016). "Arctic terrestrial hydrology: A synthesis of processes, regional effects, and research challenges." In: *Journal of Geophysical Research-Biogeosciences* 121.3, 621–649. ISSN: 2169-8953. DOI: 10.1002/2015jg003131.

Burba, G. (2013). *Eddy covariance method for scientific, industrial, agricultural and regulatory applications: A field book on measuring ecosystem gas exchange and areal emission rates*. LI-Cor Biosciences. ISBN: 061576827X.

Burba, G. et al. (2011). "Calculating CO_2 and H_2O eddy covariance fluxes from an enclosed gas analyzer using an instantaneous mixing ratio." In: *Global Change Biology* 18.1, 385–399. ISSN: 13541013. DOI: 10.1111/j.1365-2486.2011.02536.x.

Burger, M., S. Berger, I. Spangenberg, and C. Blodau (2016). "Summer fluxes of methane and carbon dioxide from a pond and floating mat in a continental Canadian peatland." In: *Biogeosciences* 13.12, 3777–3791. ISSN: 1726-4170. DOI: 10.5194/bg-13-3777-2016.

Burpee, B., J. E. Saros, R. M. Northington, and K. S. Simon (2016). "Microbial nutrient limitation in Arctic lakes in a permafrost landscape of southwest Greenland." In: *Biogeosciences* 13.2, 365–374. ISSN: 1726-4170. DOI: 10.5194/bg-13-365-2016.

Chapman, W. L. and J. E. Walsh (1993). "Recent Variations of Sea Ice and Air Temperature in High Latitudes." In: *Bulletin of the American Meteorological Society* 74.1, 33–48. ISSN: 0003-0007. DOI: 10.1175/1520-0477(1993)074<0033:Rvosia>2.0.Co;2.

Chemke, R., L. M. Polvani, J. E. Kay, and C. Orbe (2021). "Quantifying the role of ocean coupling in Arctic amplification and sea-ice loss over the 21st century." In: *npj Climate and Atmospheric Science* 4.1, 46. ISSN: 2397-3722. DOI: 10.1038/s41612-021-00204-8.

Christensen, T. R., T. Johansson, H. J. Åkerman, M. Mastepanov, N. Malmer, T. Friborg, P. Crill, and B. H. Svensson (2004). "Thawing sub-arctic permafrost: Effects on vegetation and methane emissions." In: *Geophysical Research Letters* 31.4, L04501. ISSN: 0094-8276. DOI: 10.1029/2003GL018680.

Chylek, P., C. K. Folland, G. Lesins, M. K. Dubey, and M. Wang (2009). "Arctic air temperature change amplification and the Atlantic Multidecadal Oscillation."

In: *Geophysical Research Letters* 36.14, L14801. ISSN: 0094-8276. DOI: 10.1029/2009GL038777.

Cole, J. J., D. L. Bade, D. Bastviken, M. L. Pace, and M. Van de Bogert (2010). "Multiple approaches to estimating air-water gas exchange in small lakes." In: *Limnology and Oceanography-Methods* 8.6, 285–293. ISSN: 1541-5856. DOI: 10.4319/lom.2010.8.285.

Cole, J. J. and N. F. Caraco (1998). "Atmospheric exchange of carbon dioxide in a low-wind oligotrophic lake measured by the addition of SF6." In: *Limnology and Oceanography* 43.4, 647–656. ISSN: 00243590. DOI: 10.4319/lo.1998.43.4.0647.

Colmer, T. D. (2003). "Long-distance transport of gases in plants: a perspective on internal aeration and radial oxygen loss from roots." In: *Plant, Cell & Environment* 26.1, 17–36. ISSN: 0140-7791. DOI: 10.1046/j.1365-3040.2003.00846.x.

Conrad, R. (1999). "Contribution of hydrogen to methane production and control of hydrogen concentrations in methanogenic soils and sediments." In: *FEMS Microbiology Ecology* 28.3, 193–202. DOI: 10.1016/S0168-6496(98)00086-5.

Cresto Aleina, F., V. Brovkin, S. Muster, J. Boike, L. Kutzbach, T. Sachs, and S. Zuyev (2013). "A stochastic model for the polygonal tundra based on Poisson-Voronoi diagrams." In: *Earth System Dynamics* 4.2, 187–198. ISSN: 2190-4979. DOI: 10.5194/esd-4-187-2013.

Cresto Aleina, F., B. R. K. Runkle, T. Kleinen, L. Kutzbach, J. Schneider, and V. Brovkin (2015). "Modeling micro-topographic controls on boreal peatland hydrology and methane fluxes." In: *Biogeosciences* 12.19, 5689–5704. ISSN: 1726-4170. DOI: 10.5194/bg-12-5689-2015.

Dai, A., D. Luo, M. Song, and J. Liu (2019). "Arctic amplification is caused by sea-ice loss under increasing CO_2." In: *Nature Communications* 10.1, 121. ISSN: 2041-1723. DOI: 10.1038/s41467-018-07954-9.

Dean, J. F. et al. (2020). "East Siberian Arctic inland waters emit mostly contemporary carbon." In: *Nature Communications* 11.1, 1627. ISSN: 2041-1723. DOI: 10.1038/s41467-020-15511-6.

DelSontro, T., J. J. Beaulieu, and J. A. Downing (2018). "Greenhouse gas emissions from lakes and impoundments: Upscaling in the face of global change." In: *Limnology and Oceanography Letters* 3.3, 64–75. ISSN: 2378-2242. DOI: 10.1002/lol2.10073.

DelSontro, T., L. Boutet, A. St-Pierre, P. A. del Giorgio, and Y. T. Prairie (2016). "Methane ebullition and diffusion from northern ponds and lakes regulated by the interaction between temperature and system productivity." In: *Limnology and Oceanography* 61.S1, S62–S77. ISSN: 0024-3590. DOI: 10.1002/lno.10335.

Deser, C., R. Tomas, M. Alexander, and D. Lawrence (2010). "The Seasonal Atmospheric Response to Projected Arctic Sea Ice Loss in the Late Twenty-First Century." In: *Journal of Climate* 23.2, 333–351. ISSN: 0894-8755. DOI: 10.1175/2009jcli3053.1.

Donis, D., S. Flury, A. Stöckli, J. E. Spangenberg, D. Vachon, and D. F. McGinnis (2017). "Full-scale evaluation of methane production under oxic conditions in a mesotrophic lake." In: *Nature Communications* 8.1, 1661. ISSN: 2041-1723. DOI: 10.1038/s41467-017-01648-4.

Downing, J. A. et al. (2006). "The global abundance and size distribution of lakes, ponds, and impoundments." In: *Limnology and Oceanography* 51.5, 2388–2397. ISSN: 0024-3590. DOI: 10.4319/lo.2006.51.5.2388.

Downing, J. A. (2010). "Emerging global role of small lakes and ponds: little things mean a lot." In: *Limnetica* 29.1, 0009–24. ISSN: 0213-8409.

Duc, N., P. Crill, and D. Bastviken (2010). "Implications of temperature and sediment characteristics on methane formation and oxidation in lake sediments." In: *Biogeochemistry* 100.1-3, 185–196. ISSN: 0168-2563. DOI: 10.1007/s10533-010-9415-8.

Ducharme-Riel, V., D. Vachon, P. A. del Giorgio, and Y. T. Prairie (2015). "The relative contribution of winter under-ice and summer hypolimnetic CO_2 accumulation to the annual CO_2 emissions from northern lakes." In: *Ecosystems* 18.4, 547–559. ISSN: 14350629. DOI: 10.1007/s10021-015-9846-0.

Edgington, E. and P. Onghena (2007). *Randomization tests*. CRC Press. ISBN: 9780367577711.

Ellis, C. J., L. Rochefort, G. Gauthier, and R. Pienitz (2008). "Paleoecological evidence for transitions between contrasting landforms in a polygon-patterned high arctic wetland." In: *Arctic, Antarctic, and Alpine Research* 40.4, 624–637. DOI: 10.1657/1523-0430(07-059)[ELLIS]2.0.CO;2.

Elmendorf, S. C. et al. (2011). "Global assessment of experimental climate warming on tundra vegetation: heterogeneity over space and time." In: *Ecology Letters* 15.2, 164–175. ISSN: 1461-023X. DOI: 10.1111/j.1461-0248.2011.01716.x.

Encinas Fernández, J., F. Peeters, and H. Hofmann (2016). "On the methane paradox: Transport from shallow water zones rather than in situ methanogenesis is the major source of CH_4 in the open surface water of lakes." In: *Journal of Geophysical Research: Biogeosciences* 121.10, 2717–2726. ISSN: 2169-8953. DOI: 10.1002/2016JG003586.

Eugster, W., G. Kling, T. Jonas, J. P. McFadden, A. Wüest, S. MacIntyre, and F. S. Chapin III (2003). "CO_2 exchange between air and water in an Arctic Alaskan and midlatitude Swiss lake: Importance of convective mixing." In: *Journal of Geophysical Research Atmospheres* 108.D12, 4362. ISSN: 01480227. DOI: 10.1029/2002JD002653.

Euskirchen, E. S., A. D. McGuire, F. S. Chapin III, S. Yi, and C. C. Thompson (2009). "Changes in vegetation in northern Alaska under scenarios of climate change, 2003–2100: implications for climate feedbacks." In: *Ecological Applications* 19.4, 1022–1043. ISSN: 1051-0761. DOI: 10.1890/08-0806.1.

Eyring, V., S. Bony, G. A. Meehl, C. A. Senior, B. Stevens, R. J. Stouffer, and K. E. Taylor (2016). "Overview of the Coupled Model Intercomparison Project Phase 6 (CMIP6) experimental design and organization." In: *Geosci. Model Dev.* 9.5, 1937–1958. ISSN: 1991-9603. DOI: 10.5194/gmd-9-1937-2016.

Fan, S.-M., S. C. Wofsy, P. S. Bakwin, D. J. Jacob, and D. R. Fitzjarrald (1990). "Atmosphere-biosphere exchange of CO_2 and O_3 in the central Amazon Forest." In: *Journal of Geophysical Research: Atmospheres* 95.D10, 16851–16864. DOI: 10.1029/JD095iD10p16851.

Fick, A. (1855). "V. On liquid diffusion." In: *The London, Edinburgh, and Dublin Philosophical Magazine and Journal of Science* 10.63, 30–39. ISSN: 1941-5982. DOI: 10.1080/14786445508641925.

Fratini, G., A. Ibrom, N. Arriga, G. Burba, and D. Papale (2012). "Relative humidity effects on water vapour fluxes measured with closed-path eddy-covariance systems with short sampling lines." In: *Agricultural and forest meteorology* 165, 53–63. DOI: 10.1016/j.agrformet.2012.05.018.

French, H. M. (2007). *The Periglacial Environment, 3rd ed.* John Wiley & Sons, Ltd. ISBN: 9780470865880 (print). DOI: 10.1002/9781118684931.

Gao, H., Q. Tang, X. Shi, C. Zhu, T. Bohn, F. Su, M. Pan, J. Sheffield, D. Lettenmaier, and E. Wood (2010). "Water budget record from Variable Infiltration Capacity (VIC) model." In: *Algorithm Theoretical Basis Document for Terrestrial Water Cycle Data Records*, 120–173.

Gash, J. H. C. and A. D. Culf (1996). "Applying a linear detrend to eddy correlation data in realtime." In: *Boundary-Layer Meteorology* 79.3, 301–306. ISSN: 0006-8314. DOI: 10.1007/bf00119443.

Giorgetta, M. A. et al. (2013). "Climate and carbon cycle changes from 1850 to 2100 in MPI-ESM simulations for the Coupled Model Intercomparison Project phase 5." In: *Journal of Advances in Modeling Earth Systems* 5.3, 572–597. ISSN: 1942-2466. DOI: 10.1002/jame.20038.

Graversen, R. G., T. Mauritsen, M. Tjernström, E. Källén, and G. Svensson (2008). "Vertical structure of recent Arctic warming." In: *Nature* 451.7174, 53–56. ISSN: 1476-4687. DOI: 10.1038/nature06502.

Grünfeld, S. and H. Brix (1999). "Methanogenesis and methane emissions: effects of water table, substrate type and presence of Phragmites australis." In: *Aquatic Botany* 64.1, 63–75. ISSN: 0304-3770. DOI: 10.1016/S0304-3770(99)00010-8.

Günthel, M. et al. (2020). "Photosynthesis-driven methane production in oxic lake water as an important contributor to methane emission." In: *Limnology and Oceanography* 65.12, 2853–2865. ISSN: 0024-3590. DOI: 10.1002/lno.11557.

Hamilton, P. B., K. Gajewski, D. E. Atkinson, and D. R. S. Lean (2001). "Physical and chemical limnology of 204 lakes from the Canadian Arctic Archipelago." In: *Hydrobiologia* 457, 133–148. ISSN: 0018-8158. DOI: 10.1023/A:1012275316543.

Harris, C. R. et al. (2020). "Array programming with NumPy." In: *Nature* 585.7825, 357–362. ISSN: 1476-4687. DOI: 10.1038/s41586-020-2649-2.

Hedderich, R. and W. B. Whitman (2006). "Physiology and biochemistry of the methane-producing Archaea." In: *The Prokaryotes: Volume 2: Ecophysiology and Biochemistry*. Ed. by M. Dworkin, S. Falkow, E. Rosenberg, K.-H. Schleifer, and E. Stackebrandt. New York, NY: Springer New York, 1050–1079. ISBN: 978-0-387-30742-8. DOI: 10.1007/0-387-30742-7_34.

Heiskanen, J. J., I. Mammarella, S. Haapanala, J. Pumpanen, T. Vesala, S. Macintyre, and A. Ojala (2014). "Effects of cooling and internal wave motions on gas transfer coefficients in a boreal lake." In: *Tellus Series B-Chemical and Physical Meteorology* 66.1, 22827. ISSN: 1600-0889. DOI: 10.3402/tellusb.v66.22827.

Helbig, M., J. Boike, M. Langer, P. Schreiber, B. R. K. Runkle, and L. Kutzbach (2013). "Spatial and seasonal variability of polygonal tundra water balance: Lena River Delta, northern Siberia (Russia)." In: *Hydrogeology Journal* 21.1, 133–147. ISSN: 1435-0157. DOI: 10.1007/s10040-012-0933-4.

Hersbach, H. et al. (2020). "The ERA5 global reanalysis." In: *Quarterly Journal of the Royal Meteorological Society* 146.730. data was provided by ICDC, CEN, University of Hamburg in June 2020, 1999–2049. ISSN: 0035-9009. DOI: 10.1002/qj.3803.

Hodges, J. (1958). "The significance probability of the Smirnov two-sample test." In: *Arkiv för Matematik* 43.5, 469–486. ISSN: 0004-2080.

Hoegh-Guldberg, O., D. Jacob, M Bindi, S Brown, I Camilloni, A Diedhiou, R Djalante, K Ebi, F Engelbrecht, J Guiot, et al. (2018). "Impacts of 1.5 °C Global Warming on Natural and Human Systems Supplementary Material." In: *Global Warming of 1.5 °C. An IPCC Special Report on the impacts of global warming of 1.5 °C above pre-industrial levels and related global greenhouse gas emission pathways, in the context of strengthening the global response to the threat of climate change, sustainable development, and efforts to eradicate poverty*. Ed. by V. Masson-Delmotte, P. Zhai, H.-O. Pörtner, D. Roberts, J. Skea, P. R. Shukla, A. Pirani, W. Moufouma-Okia, C. Péan, R. Pidcock, et al. Available from https://www.ipcc.ch/sr15, 175–311.

Holgerson, M. A. and P. A. Raymond (2016). "Large contribution to inland water CO_2 and CH_4 emissions from very small ponds." In: *Nature Geoscience* 9.3, 222–226. ISSN: 1752-0894. DOI: 10.1038/ngeo2654.

Holl, D., V. Pancotto, A. Heger, S. J. Camargo, and L. Kutzbach (2019a). "Cushion bogs are stronger carbon dioxide net sinks than moss-dominated bogs as revealed by eddy covariance measurements on Tierra del Fuego, Argentina." In: *Biogeosciences* 16.17, 3397–3423. DOI: 10.5194/bg-16-3397-2019.

Holl, D. et al. (2019b). "A long-term (2002 to 2017) record of closed-path and open-path eddy covariance CO_2 net ecosystem exchange fluxes from the Siberian Arctic." In: *Earth System Science Data* 11.1, 221–240. ISSN: 18663516. DOI: 10.5194/essd-11-221-2019.

Huang, W., Z. Zhang, Z. Li, M. Leppäranta, L. Arvola, S. Song, J. Huotari, and Z. Lin (2021). "Under-Ice Dissolved Oxygen and Metabolism Dynamics in a Shallow Lake: The Critical Role of Ice and Snow." In: *Water Resources Research* 57.5, e2020WR027990. ISSN: 0043-1397. DOI: 10.1029/2020WR027990.

Hugelius, G. et al. (2014). "Estimated stocks of circumpolar permafrost carbon with quantified uncertainty ranges and identified data gaps." In: *Biogeosciences* 11.23, 6573–6593. ISSN: 1726-4170. DOI: 10.5194/bg-11-6573-2014.

Hughes-Allen, L., F. Bouchard, I. Laurion, A. Séjourné, C. Marlin, C. Hatté, F. Costard, A. Fedorov, and A. Desyatkin (2020). "Seasonal patterns in greenhouse gas emissions from thermokarst lakes in Central Yakutia (Eastern Siberia)." In: *Limnology and Oceanography* 66.S1, S98–S116. ISSN: 0024-3590. DOI: 10.1002/lno.11665.

Huissteden, J. van, C. Berrittella, F. J. W. Parmentier, Y. Mi, T. C. Maximov, and A. J. Dolman (2011). "Methane emissions from permafrost thaw lakes limited by lake drainage." In: *Nature Climate Change* 1.2, 119–123. ISSN: 1758-6798. DOI: 10.1038/nclimate1101.

Hunter, J. D. (2007). "Matplotlib: A 2D Graphics Environment." In: *Computing in Science & Engineering* 9.3, 90–95. ISSN: 1558-366X. DOI: 10.1109/MCSE.2007.55.

Ibrom, A., E. Dellwik, H. Flyvbjerg, N. O. Jensen, and K. Pilegaard (2007a). "Strong low-pass filtering effects on water vapour flux measurements with closed-path

eddy correlation systems." In: *Agricultural and Forest Meteorology* 147.3-4, 140 –156. ISSN: 0168-1923. DOI: 10.1016/j.agrformet.2007.07.007.

Ibrom, A., E. Dellwik, S. E. Larsen, and K. Pilegaard (2007b). "On the use of the Webb-Pearman-Leuning theory for closed-path eddy correlation measurements." In: *Tellus, Series B: Chemical and Physical Meteorology* 59.5, 937–946. ISSN: 02806509. DOI: 10.1111/j.1600-0889.2007.00311.x.

Intrieri, J. M., C. W. Fairall, M. D. Shupe, P. O. G. Persson, E. L. Andreas, P. S. Guest, and R. E. Moritz (2002). "An annual cycle of Arctic surface cloud forcing at SHEBA." In: *Journal of Geophysical Research: Oceans* 107.C10, SHE 13–1–SHE 13–14. ISSN: 0148-0227. DOI: 10.1029/2000JC000439.

Iwata, H., R. Hirata, Y. Takahashi, Y. Miyabara, M. Itoh, and K. Iizuka (2018). "Partitioning eddy-covariance methane fluxes from a shallow lake into diffusive and ebullitive fluxes." In: *Boundary-Layer Meteorology* 169.3, 413–428. ISSN: 15731472. DOI: 10.1007/s10546-018-0383-1.

Jammet, M., S. Dengel, E. Kettner, F.-J. W. Parmentier, M. Wik, P. Crill, and T. Friborg (2017). "Year-round CH_2 and CO_2 flux dynamics in two contrasting freshwater ecosystems of the subarctic." In: *Biogeosciences* 14.22, 5189–5216. ISSN: 1726-4189. DOI: 10.5194/bg-14-5189-2017.

Jansen, J., B. F. Thornton, A. Cortés, J. Snöälv, M. Wik, S. MacIntyre, and P. M. Crill (2020). "Drivers of diffusive CH_4 emissions from shallow subarctic lakes on daily to multi-year timescales." In: *Biogeosciences* 17.7, 1911–1932. ISSN: 1726-4189. DOI: 10.5194/bg-17-1911-2020.

Jansen, J., B. F. Thornton, M. M. Jammet, M. Wik, A. Cortés, T. Friborg, S. MacIntyre, and P. M. Crill (2019). "Climate-sensitive controls on large spring emissions of CH_4 and CO_2 from northern lakes." In: *Journal of Geophysical Research: Biogeosciences* 124.7, 2379–2399. ISSN: 21698961. DOI: 10.1029/2019JG005094.

Jepsen, S. M., C. I. Voss, M. A. Walvoord, J. R. Rose, B. J. Minsley, and B. D. Smith (2013). "Sensitivity analysis of lake mass balance in discontinuous permafrost: the example of disappearing Twelvemile Lake, Yukon Flats, Alaska (USA)." In: *Hydrogeology Journal* 21.1, 185–200. ISSN: 1435-0157. DOI: 10.1007/s10040-012-0896-5.

Joabsson, A. and T. R. Christensen (2002). "Methane emissions from wetlands and their relationship with vascular plants: an Arctic example." In: *Global Change Biology* 7.8, 919–932. ISSN: 1354-1013. DOI: 10.1046/j.1354-1013.2001.00044.x.

Joabsson, A., T. R. Christensen, and B. Wallén (1999). "Vascular plant controls on methane emissions from northern peatforming wetlands." In: *Trends in Ecology & Evolution* 14.10, 385–388. ISSN: 0169-5347. DOI: 10.1016/S0169-5347(99)01649-3.

Jones, B. M. et al. (2022). "Lake and drained lake basin systems in lowland permafrost regions." In: *Nature Reviews Earth & Environment* 3.1, 85–98. ISSN: 2662-138X. DOI: 10.1038/s43017-021-00238-9.

Jong, A. E. E. de, M. H. in 't Zandt, O. H. Meisel, M. S. M. Jetten, J. F. Dean, O. Rasigraf, and C. U. Welte (2018). "Increases in temperature and nutrient availability positively affect methane-cycling microorganisms in Arctic thermokarst lake sediments." In: *Environmental Microbiology* 20.12, 4314–4327. ISSN: 1462-2912. DOI: 10.1111/1462-2920.14345.

Jonsson, A., J. Åberg, A. Lindroth, and M. Jansson (2008). "Gas transfer rate and CO_2 flux between an unproductive lake and the atmosphere in northern Sweden." In: *Journal of Geophysical Research: Biogeosciences* 113.4, G04006. ISSN: 01480227. DOI: 10.1029/2008JG000688.

Jorgenson, M. T., M. Kanevskiy, Y. Shur, N. Moskalenko, D. R. N. Brown, K. Wickland, R. Striegl, and J. Koch (2015). "Role of ground ice dynamics and ecological feedbacks in recent ice wedge degradation and stabilization." In: *Journal of Geophysical Research: Earth Surface* 120.11, 2280–2297. ISSN: 2169-9003. DOI: 10.1002/2015JF003602.

Jorgenson, M. T., Y. L. Shur, and E. R. Pullman (2006). "Abrupt increase in permafrost degradation in Arctic Alaska." In: *Geophysical Research Letters* 33.2, L02503. ISSN: 0094-8276. DOI: 10.1029/2005GL024960.

Juhls, B., S. Antonova, M. Angelopoulos, N. Bobrov, M. Grigoriev, M. Langer, G. Maksimov, F. Miesner, and P. P. Overduin (2021). "Serpentine (Floating) Ice Channels and their Interaction with Riverbed Permafrost in the Lena River Delta, Russia." In: *Frontiers in Earth Science* 9.689941. ISSN: 2296-6463. DOI: 10.3389/feart.2021.689941.

Juutinen, S., M. Rantakari, P. Kortelainen, J. T. Huttunen, T. Larmola, J. Alm, J. Silvola, and P. J. Martikainen (2009). "Methane dynamics in different boreal lake types." In: *Biogeosciences* 6.2, 209–223. ISSN: 1726-4170. DOI: 10.5194/bg-6-209-2009.

Juutinen, S., J. Alm, T. Larmola, J. T. Huttunen, M. Morero, P. J. Martikainen, and J. Silvola (2003). "Major implication of the littoral zone for methane release from boreal lakes." In: *Global Biogeochemical Cycles* 17.4. ISSN: 0886-6236. DOI: 10.1029/2003GB002105.

Kaimal, J. C. and J. J. Finnigan (1994). *Atmospheric boundary layer flows: their structure and measurement*. Oxford university press. ISBN: 9780195062397 (print). DOI: 10.1093/oso/9780195062397.001.0001.

Kartoziia, A. (2019). "Assessment of the Ice Wedge Polygon Current State by Means of UAV Imagery Analysis (Samoylov Island, the Lena Delta)." In: *Remote Sensing* 11.13, 1627. ISSN: 2072-4292. DOI: 10.3390/rs11131627.

Kim, Y. (2015). "Effect of thaw depth on fluxes of CO_2 and CH_4 in manipulated Arctic coastal tundra of Barrow, Alaska." In: *Science of The Total Environment* 505, 385–389. ISSN: 0048-9697. DOI: 10.1016/j.scitotenv.2014.09.046.

Kling, G. W., G. W. Kipphut, and M. C. Miller (1992). "The flux of CO_2 and CH_4 from lakes and rivers in arctic Alaska." In: *Hydrobiologia* 240.1, 23–36. ISSN: 00188158. DOI: 10.1007/BF00013449.

Knight, W. R. (1966). "A Computer Method for Calculating Kendall's Tau with Ungrouped Data." In: *Journal of the American Statistical Association* 61.314, 436–439. ISSN: 0162-1459. DOI: 10.1080/01621459.1966.10480879.

Knoblauch, C., O. Spott, S. Evgrafova, L. Kutzbach, and E. M. Pfeiffer (2015). "Regulation of methane production, oxidation, and emission by vascular plants and bryophytes in ponds of the northeast Siberian polygonal tundra." In: *Journal of Geophysical Research-Biogeosciences* 120.12, 2525–2541. ISSN: 2169-8953. DOI: 10.1002/2015jg003053.

Koch, J. C., M. T. Jorgenson, K. P. Wickland, M. Kanevskiy, and R. Striegl (2018). "Ice Wedge Degradation and Stabilization Impact Water Budgets and Nutrient Cycling in Arctic Trough Ponds." In: *Journal of Geophysical Research-Biogeosciences* 123.8, 2604–2616. ISSN: 2169-8953. DOI: 10.1029/2018jg004528.

Kormann, R. and F. X. Meixner (2001). "An analytical footprint model for non-neutral stratification." In: *Boundary-Layer Meteorology* 99.2, 207–224. DOI: 10.1023/A:1018991015119.

Kraemer, B. M. et al. (2015). "Morphometry and average temperature affect lake stratification responses to climate change." In: *Geophysical Research Letters* 42.12, 4981–4988. ISSN: 0094-8276. DOI: 10.1002/2015GL064097.

Kuhn, M. A., R. K. Varner, D. Bastviken, P. Crill, S. MacIntyre, M. Turetsky, K. Walter Anthony, A. D. McGuire, and D. Olefeldt (2021). "BAWLD-CH4: a comprehensive dataset of methane fluxes from boreal and arctic ecosystems." In: *Earth Syst. Sci. Data* 13.11, 5151–5189. ISSN: 1866-3516. DOI: 10.5194/essd-13-5151-2021.

Kuhn, M., E. J. Lundin, R. Giesler, M. Johansson, and J. Karlsson (2018). "Emissions from thaw ponds largely offset the carbon sink of northern permafrost wetlands." In: *Scientific Reports* 8.9535. ISSN: 2045-2322. DOI: 10.1038/s41598-018-27770-x.

Kutzbach, L., D. Wagner, and E. M. Pfeiffer (2004). "Effect of microrelief and vegetation on methane emission from wet polygonal tundra, Lena Delta, Northern Siberia." In: *Biogeochemistry* 69.3, 341–362. ISSN: 0168-2563. DOI: 10.1023/B:BIOG.0000031053.81520.db.

Kutzbach, L., C. Wille, and E. M. Pfeiffer (2007). "The exchange of carbon dioxide between wet arctic tundra and the atmosphere at the Lena River Delta, Northern Siberia." In: *Biogeosciences* 4.5, 869–890. ISSN: 17264189. DOI: 10.5194/bg-4-869-2007.

LI-COR (2019). *EddyPro Version 7.0.6*.

Labrecque, S., D. Lacelle, C. R. Duguay, B. Lauriol, and J. Hawkings (2009). "Contemporary (1951 - 2001) Evolution of Lakes in the Old Crow Basin, Northern Yukon, Canada: Remote Sensing, Numerical Modeling, and Stable Isotope Analysis." In: *Arctic* 62.2, 225–238. ISSN: 00040843. DOI: 10.14430/arctic134.

Langer, M., S. Westermann, K. W. Anthony, K. Wischnewski, and J. Boike (2015). "Frozen ponds: production and storage of methane during the Arctic winter in a lowland tundra landscape in northern Siberia, Lena River delta." In: *Biogeosciences* 12.4, 977–990. ISSN: 1726-4170. DOI: 10.5194/bg-12-977-2015.

Langer, M., S. Westermann, J. Boike, G. Kirillin, G. Grosse, S. Peng, and G. Krinner (2016). "Rapid degradation of permafrost underneath waterbodies in tundra landscapes-Toward a representation of thermokarst in land surface models." In: *Journal of Geophysical Research-Earth Surface* 121.12, 2446–2470. ISSN: 2169-9003. DOI: 10.1002/2016jf003956.

Lara, M. J., D. H. Lin, C. Andresen, V. L. Lougheed, and C. E. Tweedie (2019). "Nutrient Release From Permafrost Thaw Enhances CH_4 Emissions From Arctic Tundra Wetlands." In: *Journal of Geophysical Research: Biogeosciences* 124.6, 1560–1573. ISSN: 2169-8953. DOI: 10.1029/2018JG004641.

Laurion, I., W. F. Vincent, S. MacIntyre, L. Retamal, C. Dupont, P. Francus, and R. Pienitz (2009). "Variability in greenhouse gas emissions from permafrost

thaw ponds." In: *Limnology and Oceanography* 55.1, 115–133. ISSN: 0024-3590. DOI: 10.4319/lo.2010.55.1.0115.

Lehmann, M., M. Simona, S. Wyss, J. Blees, C. Frame, H. Niemann, M. Veronesi, and J. Zopfi (2015). "Powering up the "biogeochemical engine": the impact of exceptional ventilation of a deep meromictic lake on the lacustrine redox, nutrient, and methane balances." In: *Frontiers in Earth Science* 3.45. ISSN: 2296-6463. DOI: 10.3389/feart.2015.00045.

Lewis, W. M. (1983). "A Revised Classification of Lakes Based on Mixing." In: *Canadian Journal of Fisheries and Aquatic Sciences* 40.10, 1779–1787. DOI: 10.1139/f83-207.

Liebner, S. and D. Wagner (2007). "Abundance, distribution and potential activity of methane oxidizing bacteria in permafrost soils from the Lena Delta, Siberia." In: *Environmental Microbiology* 9.1, 107–117. ISSN: 1462-2912. DOI: 10.1111/j.1462-2920.2006.01120.x.

Liebner, S., J. Zeyer, D. Wagner, C. Schubert, E.-M. Pfeiffer, and C. Knoblauch (2011). "Methane oxidation associated with submerged brown mosses reduces methane emissions from Siberian polygonal tundra." In: *Journal of Ecology* 99.4, 914–922. ISSN: 0022-0477. DOI: 10.1111/j.1365-2745.2011.01823.x.

Liljedahl, A. K. et al. (2016). "Pan-Arctic ice-wedge degradation in warming permafrost and its influence on tundra hydrology." In: *Nature Geoscience* 9.4, 312–318. ISSN: 1752-0908. DOI: 10.1038/ngeo2674.

Lim, D. S. S., M. S. V. Douglas, J. P. Smol, and D. R. S. Lean (2001). "Physical and Chemical Limnological Characteristics of 38 Lakes and Ponds on Bathurst Island, Nunavut, Canadian High Arctic." In: *International Review of Hydrobiology* 86.1, 1–22. ISSN: 1434-2944. DOI: 10.1002/1522-2632(200101)86:1<1::AID-IROH1>3.0.CO;2-E.

Ling, F. and T. Zhang (2003). "Numerical simulation of permafrost thermal regime and talik development under shallow thaw lakes on the Alaskan Arctic Coastal Plain." In: *Journal of Geophysical Research: Atmospheres* 108.D16, 4511. ISSN: 0148-0227. DOI: 10.1029/2002JD003014.

Liss, P. S. and P. G. Slater (1974). "Flux of gases across the Air-Sea interface." In: *Nature* 247.5438, 181–184. ISSN: 00280836. DOI: 10.1038/247181a0.

Lofton, D. D., S. C. Whalen, and A. E. Hershey (2014). "Effect of temperature on methane dynamics and evaluation of methane oxidation kinetics in shallow Arctic Alaskan lakes." In: *Hydrobiologia* 721.1, 209–222. ISSN: 0018-8158. DOI: 10.1007/s10750-013-1663-x.

Lundin, E. J., R. Giesler, A. Persson, M. S. Thompson, and J. Karlsson (2013). "Integrating carbon emissions from lakes and streams in a subarctic catchment." In: *Journal of Geophysical Research: Biogeosciences* 118.3, 1200–1207. ISSN: 21698961. DOI: 10.1002/jgrg.20092.

MATLAB (2019). *MATLAB Software 2019b*. The MathWorks, Natick, MA, USA.

MacIntyre, S., A. Jonsson, M. Jansson, J. Aberg, D. E. Turney, and S. D. Miller (2010). "Buoyancy flux, turbulence, and the gas transfer coefficient in a stratified lake." In: *Geophysical Research Letters* 37.24, L24604. ISSN: 0094-8276. DOI: 10.1029/2010gl044164.

Martin, A. F., T. C. Lantz, and E. R. Humphreys (2017). "Ice wedge degradation and CO_2 and CH_4 emissions in the Tuktoyaktuk Coastlands, Northwest Territories." In: *Arctic Science* 4.1, 130–145. ISSN: 2368-7460. DOI: 10.1139/as-2016-0011.

Martinez-Cruz, K., A. Sepulveda-Jauregui, K. Walter Anthony, and F. Thalasso (2015). "Geographic and seasonal variation of dissolved methane and aerobic methane oxidation in Alaskan lakes." In: *Biogeosciences* 12.15, 4595–4606. ISSN: 1726-4189. DOI: 10.5194/bg-12-4595-2015.

Matthews, C. J. D., V. L. St Louis, and R. H. Hesslein (2003). "Comparison of three techniques used to measure diffusive gas exchange from sheltered aquatic surfaces." In: *Environmental Science & Technology* 37.4, 772–780. ISSN: 0013-936X. DOI: 10.1021/es0205838.

Matthews, E., M. S. Johnson, V. Genovese, J. Du, and D. Bastviken (2020). "Methane emission from high latitude lakes: methane-centric lake classification and satellite-driven annual cycle of emissions." In: *Scientific Reports* 10.1, 12465. ISSN: 2045-2322. DOI: 10.1038/s41598-020-68246-1.

Mauder, M and T Foken (2004). "Documentation and instruction manual of the eddy covariance software package TK2, Univ." In: *Bayreuth, Abt. Mikrometeorol., ISSN* 161489166.26, 1–45.

Mauritsen, T. et al. (2019). "Developments in the MPI-M Earth System Model version 1.2 (MPI-ESM1.2) and Its Response to Increasing CO_2." In: *Journal of Advances in Modeling Earth Systems* 11.4, 998–1038. DOI: 10.1029/2018MS001400.

McGuire, A. D. et al. (2012). "An assessment of the carbon balance of Arctic tundra: Comparisons among observations, process models, and atmospheric inversions." In: *Biogeosciences* 9.8, 3185–3204. ISSN: 17264170. DOI: 10.5194/bg-9-3185-2012.

Minayeva, T., A. Sirin, P. Kershaw, and O. Bragg (2016). "Arctic Peatlands." In: *The Wetland Book*. Ed. by C. Finlayson, G. Milton, R. Prentice, and N. Davidson. Springer, Dordrecht, 1–15. ISBN: 978-94-007-6173-5 (online). DOI: 10.1007/978-94-007-6173-5_109-2.

Miner, K. R., M. R. Turetsky, E. Malina, A. Bartsch, J. Tamminen, A. D. McGuire, A. Fix, C. Sweeney, C. D. Elder, and C. E. Miller (2022). "Permafrost carbon emissions in a changing Arctic." In: *Nature Reviews Earth & Environment* 3.1, 55–67. ISSN: 2662-138X. DOI: 10.1038/s43017-021-00230-3.

Minke, M., N. Donner, N. S. Karpov, P. de Klerk, and H. Joosten (2007). "Distribution, diversity, development and dynamics of polygon mires: examples from Northeast Yakutia (Siberia)." In: *Peatlands International 2007.1*. International Peatland Society, 36–40.

Mironov, D. V. (2005). *Parameterization of Lakes in Numerical Weather Prediction. Part 1: Description of a Lake Model*. Report. German Weather Service, 1–41.

Moncrieff, J., R. Clement, J. Finnigan, and T. Meyers (2004). "Averaging, detrending, and filtering of eddy covariance time series." In: *Handbook of micrometeorology*. Springer, 7–31. DOI: 10.1007/1-4020-2265-4_2.

Muster, S., M. Langer, B. Heim, S. Westermann, and J. Boike (2012). "Subpixel heterogeneity of ice-wedge polygonal tundra: a multi-scale analysis of land cover and evapotranspiration in the Lena River Delta, Siberia." In: *Tellus Series B-Chemical and Physical Meteorology* 64.1, 17301. ISSN: 0280-6509. DOI: 10.3402/tellusb.v64i0.17301.

Muster, S. et al. (2017). "PeRL: a circum-Arctic Permafrost Region Pond and Lake database." In: *Earth System Science Data* 9.1, 317–348. ISSN: 1866-3508. DOI: 10.5194/essd-9-317-2017.

Muster, S. et al. (2019). "Size Distributions of Arctic Waterbodies Reveal Consistent Relations in Their Statistical Moments in Space and Time." In: *Frontiers in Earth Science* 7.5. ISSN: 2296-6463. DOI: 10.3389/feart.2019.00005.

Myneni, R., Y. Knyazikhin, and T Park (2015). *MOD15A2H MODIS/Terra Leaf Area Index/FAPAR 8-Day L4 Global 500m SIN Grid V006. NASA EOSDIS Land Processes DAAC*. http://doi.org/10.5067/MODIS/MOD15A2H.006 [last access: January 12, 2021], distributed by the Land Processes Distributed Active Archive Center (LP DAAC), located at the U.S. Geological Survey (USGS) Earth Resources Observation and Science (EROS) Center (lpdaac.usgs.gov), provided with de-coded quality flags and per grid cell latitude / longitude information in netCDF format by the Integrated Climate Data Center (ICDC), CEN, University of Hamburg, Germany.

Natchimuthu, S., I. Sundgren, M. Galfalk, L. Klemedtsson, P. Crill, A. Danielsson, and D. Bastviken (2015). "Spatio-temporal variability of lake CH_4 fluxes and its influence on annual whole lake emission estimates." In: *Limnology and Oceanography* 61.S1, S13–S26. ISSN: 0024-3590. DOI: 10.1002/lno.10222.

Neff, J. C. and G. P. Asner (2001). "Dissolved organic carbon in terrestrial ecosystems: Synthesis and a model." In: *Ecosystems* 4.1, 29–48. ISSN: 14329840. DOI: 10.1007/s100210000058.

Negandhi, K., I. Laurion, and C. Lovejoy (2014). "Bacterial communities and greenhouse gas emissions of shallow ponds in the High Arctic." In: *Polar Biology* 37.11, 1669–1683. ISSN: 0722-4060. DOI: 10.1007/s00300-014-1555-1.

Negandhi, K., I. Laurion, and C. Lovejoy (2016). "Temperature effects on net greenhouse gas production and bacterial communities in arctic thaw ponds." In: *Fems Microbiology Ecology* 92.8, fiw117. ISSN: 0168-6496. DOI: 10.1093/femsec/fiw117.

Negandhi, K., I. Laurion, M. J. Whiticar, P. E. Galand, X. M. Xu, and C. Lovejoy (2013). "Small Thaw Ponds: An Unaccounted Source of Methane in the Canadian High Arctic." In: *Plos One* 8.11, e78204. ISSN: 1932-6203. DOI: 10.1371/journal.pone.0078204.

Nitzbon, J., M. Langer, S. Westermann, L. Martin, K. S. Aas, and J. Boike (2019). "Pathways of ice-wedge degradation in polygonal tundra under different hydrological conditions." In: *The Cryosphere* 13.4, 1089–1123. ISSN: 1994-0424. DOI: 10.5194/tc-13-1089-2019.

Ortiz-Llorente, M. J. and M. Alvarez-Cobelas (2012). "Comparison of biogenic methane emissions from unmanaged estuaries, lakes, oceans, rivers and wetlands." In: *Atmospheric Environment* 59, 328–337. ISSN: 1352-2310. DOI: 10.1016/j.atmosenv.2012.05.031.

Osudar, R., S. Liebner, M. Alawi, S. Z. Yang, I. Bussmann, and D. Wagner (2016). "Methane turnover and methanotrophic communities in arctic aquatic ecosystems of the Lena Delta, Northeast Siberia." In: *Fems Microbiology Ecology* 92.8, fiw116. ISSN: 0168-6496. DOI: 10.1093/femsec/fiw116.

Pedregosa, F., G. Varoquaux, A. Gramfort, V. Michel, B. Thirion, O. Grisel, M. Blondel, P. Prettenhofer, R. Weiss, and V. Dubourg (2011). "Scikit-learn: Machine

learning in Python." In: *the Journal of machine Learning research* 12, 2825–2830. ISSN: 1532-4435.

Peeters, F., J. Encinas Fernandez, and H. Hofmann (2019). "Sediment fluxes rather than oxic methanogenesis explain diffusive CH_4 emissions from lakes and reservoirs." In: *Scientific Reports* 9.1, 243. ISSN: 2045-2322. DOI: 10.1038/s41598-018-36530-w.

Pernica, P., M. G. Wells, and S. MacIntyre (2014). "Persistent weak thermal stratification inhibits mixing in the epilimnion of north-temperate Lake Opeongo, Canada." In: *Aquatic Sciences* 76.2, 187–201. ISSN: 1420-9055. DOI: 10.1007/s00027-013-0328-1.

Pienitz, R., P. T. Doran, and S. F. Lamoureux (2008). "Origin and geomorphology of lakes in the polar regions." In: *Polar lakes and rivers: limnology of Arctic and Antarctic aquatic ecosystems*, 25–41.

Polishchuk, Y. M., A. N. Bogdanov, I. N. Muratov, V. Y. Polishchuk, A. Lim, R. M. Manasypov, L. S. Shirokova, and O. S. Pokrovsky (2018). "Minor contribution of small thaw ponds to the pools of carbon and methane in the inland waters of the permafrost-affected part of the Western Siberian Lowland." In: *Environmental Research Letters* 13.4, 1–15. ISSN: 1748-9326. DOI: 10.1088/1748-9326/aab046.

Praetzel, L. S. E., M. Schmiedeskamp, and K.-H. Knorr (2021). "Temperature and sediment properties drive spatiotemporal variability of methane ebullition in a small and shallow temperate lake." In: *Limnology and Oceanography* 66.7, 2598–2610. ISSN: 0024-3590. DOI: 10.1002/lno.11775.

Prėskienis, V., I. Laurion, F. Bouchard, P. M. J. Douglas, M. F. Billett, D. Fortier, and X. Xu (2021). "Seasonal patterns in greenhouse gas emissions from lakes and ponds in a High Arctic polygonal landscape." In: *Limnology and Oceanography* 66.S1, S117–S141. ISSN: 0024-3590. DOI: 10.1002/lno.11660.

Ramsar Convention Secretariat (2016). *An introduction to the ramsar convention on wetlands (previously The Ramsar Convention Manual)*. Ramsar Convention Secretariat, Gland, Switzerland.

Rautio, M., F. Dufresne, I. Laurion, S. Bonilla, W. F. Vincent, and K. S. Christoffersen (2011). "Shallow freshwater ecosystems of the circumpolar Arctic." In: *Écoscience* 18.3, 204–222. ISSN: 1195-6860. DOI: 10.2980/18-3-3463.

Read, J. S. et al. (2012). "Lake-size dependency of wind shear and convection as controls on gas exchange." In: *Geophysical Research Letters* 39.9, L09405. ISSN: 0094-8276. DOI: 10.1029/2012gl051886.

Rehder, Z., A. Zaplavnova, and L. Kutzbach (2020). "Dissolved-gas concentrations, physical and chemical properties of 41 ponds as well as key meteorological parameters in the Lena River Delta, Siberia." In: PANGAEA. DOI: 10.1594/PANGAEA.922399.

Rehder, Z., A. Zaplavnova, and L. Kutzbach (2021). "Identifying Drivers Behind Spatial Variability of Methane Concentrations in East Siberian Ponds." In: *Frontiers in Earth Science* 9.183, 617662. ISSN: 2296-6463. DOI: 10.3389/feart.2021.617662.

Repo, M. E., J. T. Huttunen, A. V. Naumov, A. V. Chichulin, E. D. Lapshina, W. Bleuten, and P. J. Martikainen (2007). "Release of CO_2 and CH_4 from small wetland lakes in western Siberia." In: *Tellus, Series B: Chemical and Physical Meteorology* 59.5, 788–796. ISSN: 02806509. DOI: 10.1111/j.1600-0889.2007.00301.x.

Rinta, P., D. Bastviken, J. Schilder, M. Van Hardenbroek, T. Stotter, and O. Heiri (2017). "Higher late summer methane emission from central than northern European lakes." In: *Journal of Limnology* 76.1, 52–67. ISSN: 1129-5767. DOI: 10.4081/jlimnol.2016.1475.

Riordan, B., D. Verbyla, and A. D. McGuire (2006). "Shrinking ponds in subarctic Alaska based on 1950–2002 remotely sensed images." In: *Journal of Geophysical Research: Biogeosciences* 111.G4, G04002. ISSN: 0148-0227. DOI: 10.1029/2005JG000150.

Rößger, N., C. Wille, D. Holl, M. Göckede, and L. Kutzbach (2019a). "Scaling and balancing carbon dioxide fluxes in a heterogeneous tundra ecosystem of the Lena River Delta." In: *Biogeosciences* 16.13, 2591–2615. ISSN: 17264189. DOI: 10.5194/bg-16-2591-2019.

Rößger, N., C. Wille, G. Veh, J. Boike, and L. Kutzbach (2019b). "Scaling and balancing methane fluxes in a heterogeneous tundra ecosystem of the Lena River Delta." In: *Agricultural and Forest Meteorology* 266-267.August 2017, 243–255. ISSN: 01681923. DOI: 10.1016/j.agrformet.2018.06.026.

Runkle, B. R., T. Sachs, C. Wille, E. M. Pfeiffer, and L. Kutzbach (2013). "Bulk partitioning the growing season net ecosystem exchange of CO_2 in Siberian tundra reveals the seasonality of it carbon sequestration strength." In: *Biogeosciences* 10.3, 1337–1349. ISSN: 17264189. DOI: 10.5194/bg-10-1337-2013.

Sabrekov, A. F., B. R. K. Runkle, M. V. Glagolev, I. E. Terentieva, V. M. Stepanenko, O. R. Kotsyurbenko, S. S. Maksyutov, and O. S. Pokrovsky (2017). "Variability in methane emissions from West Siberia's shallow boreal lakes on a regional scale and its environmental controls." In: *Biogeosciences* 14.15, 3715–3742. ISSN: 1726-4170. DOI: 10.5194/bg-14-3715-2017.

Sachs, T., C. Wille, J. Boike, and L. Kutzbach (2008). "Environmental controls on ecosystem-scale CH_4 emission from polygonal tundra in the Lena River Delta, Siberia." In: *Journal of Geophysical Research-Biogeosciences* 113.G3, G00A03. ISSN: 2169-8953. DOI: 10.1029/2007jg000505.

Sachs, T., M. Giebels, J. Boike, and L. Kutzbach (2010). "Environmental controls on CH_4 emission from polygonal tundra on the microsite scale in the Lena river delta, Siberia." In: *Global Change Biology* 16.11, 3096–3110. ISSN: 1354-1013. DOI: 10.1111/j.1365-2486.2010.02232.x.

Sander, R. (2015). "Compilation of Henry's law constants (version 4.0) for water as solvent." In: *Atmospheric Chemistry and Physics* 15.8, 4399–4981. ISSN: 1680-7316. DOI: 10.5194/acp-15-4399-2015.

Sang, X., X.-Q. Yang, L. Tao, J. Fang, and X. Sun (2022). "Decadal changes of wintertime poleward heat and moisture transport associated with the amplified Arctic warming." In: *Climate Dynamics* 58.1, 137–159. ISSN: 1432-0894. DOI: 10.1007/s00382-021-05894-7.

Santos Fonseca, A. L. dos, C. C. Marinho, and F. de Assis Esteves (2017). "Potential Methane Production Associated with Aquatic Macrophytes Detritus in a Tropical Coastal Lagoon." In: *Wetlands* 37.4, 763–771. ISSN: 1943-6246. DOI: 10.1007/s13157-017-0912-6.

Saunois, M. et al. (2020). "The Global Methane Budget 2000–2017." In: *Earth System Science Data* 12.3, 1561–1623. DOI: 10.5194/essd-12-1561-2020.

Schneider, J., G. Grosse, and D. Wagner (2009). "Land cover classification of tundra environments in the Arctic Lena Delta based on Landsat 7 ETM+ data and its application for upscaling of methane emissions." In: *Remote Sensing of Environment* 113.2, 380–391. ISSN: 0034-4257. DOI: 10.1016/j.rse.2008.10.013.

Schwamborn, G., V. Rachold, and M. N. Grigoriev (2002). "Late Quaternary sedimentation history of the Lena Delta." In: *Quaternary International* 89.1, 119–134. ISSN: 1040-6182. DOI: 10.1016/S1040-6182(01)00084-2.

Screen, J. A. and I. Simmonds (2010a). "Increasing fall-winter energy loss from the Arctic Ocean and its role in Arctic temperature amplification." In: *Geophysical Research Letters* 37.16, L16707. ISSN: 0094-8276. DOI: 10.1029/2010GL044136.

Screen, J. A. and I. Simmonds (2010b). "The central role of diminishing sea ice in recent Arctic temperature amplification." In: *Nature* 464.7293, 1334–1337. ISSN: 1476-4687. DOI: 10.1038/nature09051.

Sepulveda-Jauregui, A., K. M. W. Anthony, K. Martinez-Cruz, S. Greene, and F. Thalasso (2015). "Methane and carbon dioxide emissions from 40 lakes along a north-south latitudinal transect in Alaska." In: *Biogeosciences* 12.11, 3197–3223. ISSN: 1726-4170. DOI: 10.5194/bg-12-3197-2015.

Serreze, M. C. and R. G. Barry (2011). "Processes and impacts of Arctic amplification: A research synthesis." In: *Global and Planetary Change* 77.1-2, 85–96. ISSN: 0921-8181. DOI: 10.1016/j.gloplacha.2011.03.004.

Sieczko, A. K., N. T. Duc, J. Schenk, G. Pajala, D. Rudberg, H. O. Sawakuchi, and D. Bastviken (2020). "Diel variability of methane emissions from lakes." In: *Proceedings of the National Academy of Sciences* 117.35, 21488–21494. ISSN: 0027-8424. DOI: 10.1073/pnas.2006024117.

Smith, L. C., Y. Sheng, G. M. MacDonald, and L. D. Hinzman (2005). "Disappearing Arctic Lakes." In: *Science* 308.5727, 1429. DOI: doi:10.1126/science.1108142.

Squires, M. M. and L. F. Lesack (2003). "The relation between sediment nutrient content and macrophyte biomass and community structure along a water transparency gradient among lakes of the Mackenzie Delta." In: *Canadian Journal of Fisheries and Aquatic Sciences* 60.3, 333–343. ISSN: 0706652X. DOI: 10.1139/f03-027.

Stepanenko, V. M., E. E. Machul'skaya, M. V. Glagolev, and V. N. Lykossov (2011). "Numerical Modeling of Methane Emissions from Lakes in the Permafrost Zone." In: *Izvestiya Atmospheric and Oceanic Physics* 47.2, 252–264. ISSN: 0001-4338. DOI: 10.1134/S0001433811020113.

Stow, D. A. et al. (2004). "Remote sensing of vegetation and land-cover change in Arctic Tundra Ecosystems." In: *Remote Sensing of Environment* 89.3, 281–308. ISSN: 0034-4257. DOI: 10.1016/j.rse.2003.10.018.

Ström, L., A. Ekberg, M. Mastepanov, and T. Røjle Christensen (2003). "The effect of vascular plants on carbon turnover and methane emissions from a tundra wetland." In: *Global Change Biology* 9.8, 1185–1192. ISSN: 1354-1013. DOI: 10.1046/j.1365-2486.2003.00655.x.

Ström, L., M. Mastepanov, and T. R. Christensen (2005). "Species-specific Effects of Vascular Plants on Carbon Turnover and Methane Emissions from Wetlands." In: *Biogeochemistry* 75.1, 65–82. ISSN: 1573-515X. DOI: 10.1007/s10533-004-6124-1.

Ström, L., T. Tagesson, M. Mastepanov, and T. R. Christensen (2012). "Presence of Eriophorum scheuchzeri enhances substrate availability and methane emission

in an Arctic wetland." In: *Soil Biology and Biochemistry* 45, 61–70. ISSN: 0038-0717. DOI: 10.1016/j.soilbio.2011.09.005.

Surdu, C. M., C. R. Duguay, L. C. Brown, and D. Fernández Prieto (2014). "Response of ice cover on shallow lakes of the North Slope of Alaska to contemporary climate conditions (1950-2011): radar remote-sensing and numerical modeling data analysis." In: *The Cryosphere* 8.1, 167–180. ISSN: 1994-0424. DOI: 10.5194/tc-8-167-2014.

Swaminathan, C. R. and V. R. Voller (1992). "A general enthalpy method for modeling solidification processes." In: *Metallurgical Transactions B* 23.5, 651–664. ISSN: 1543-1916. DOI: 10.1007/BF02649725.

Tan, Z. L. and Q. L. Zhuang (2015). "Methane emissions from pan-Arctic lakes during the 21st century: An analysis with process-based models of lake evolution and biogeochemistry." In: *Journal of Geophysical Research-Biogeosciences* 120.12, 2641–2653. ISSN: 2169-8953. DOI: 10.1002/2015jg003184.

Treat, C. C. et al. (2018). "Tundra landscape heterogeneity, not interannual variability, controls the decadal regional carbon balance in the Western Russian Arctic." In: *Global Change Biology* 24.11, 5188–5204. ISSN: 13652486. DOI: 10.1111/gcb.14421.

Tuovinen, J.-P., M. Aurela, J. Hatakka, A. Räsänen, T. Virtanen, J. Mikola, V. Ivakhov, V. Kondratyev, and T. Laurila (2019). "Interpreting eddy covariance data from heterogeneous Siberian tundra: land-cover-specific methane fluxes and spatial representativeness." In: *Biogeosciences* 16.2, 255–274. DOI: 10.5194/bg-16-255-2019.

Turner, J. C., C. J. Moorberg, A. Wong, K. Shea, M. P. Waldrop, M. R. Turetsky, and R. B. Neumann (2020). "Getting to the Root of Plant-Mediated Methane Emissions and Oxidation in a Thermokarst Bog." In: *Journal of Geophysical Research: Biogeosciences* 125.11, e2020JG005825. ISSN: 2169-8953. DOI: 10.1029/2020JG005825.

Tveit, A. T., T. Urich, P. Frenzel, and M. M. Svenning (2015). "Metabolic and trophic interactions modulate methane production by Arctic peat microbiota in response to warming." In: *Proceedings of the National Academy of Sciences of the United States of America* 112.19, E2507–E2516. ISSN: 0027-8424. DOI: 10.1073/pnas.1420797112.

U.S. Geological Survey, EROS Center (1965). *CORONA Satellite Photographs*.

Vachon, D., T. Langenegger, D. Donis, and D. F. McGinnis (2019). "Influence of water column stratification and mixing patterns on the fate of methane produced in deep sediments of a small eutrophic lake." In: *Limnology and Oceanography* 64.5, 2114–2128. ISSN: 0024-3590. DOI: 10.1002/lno.11172.

Vickers, D. and L. Mahrt (1997). "Quality control and flux sampling problems for tower and aircraft data." In: *Journal of Atmospheric and Oceanic Technology* 14.3, 512–526. ISSN: 07390572. DOI: 10.1175/1520-0426(1997)014<0512:QCAFSP>2.0.CO;2.

Villarreal, S., R. D. Hollister, D. R. Johnson, M. J. Lara, P. J. Webber, and C. E. Tweedie (2012). "Tundra vegetation change near Barrow, Alaska (1972–2010)." In: *Environmental Research Letters* 7.1, 015508. ISSN: 1748-9326. DOI: 10.1088/1748-9326/7/1/015508.

Virtanen, P. et al. (2020). "SciPy 1.0: fundamental algorithms for scientific computing in Python." In: *Nature Methods* 17.3, 261–272. ISSN: 1548-7105. DOI: 10.1038/s41592-019-0686-2.

Vizza, C., W. E. West, S. E. Jones, J. A. Hart, and G. A. Lamberti (2017). "Regulators of coastal wetland methane production and responses to simulated global change." In: *Biogeosciences* 14.2, 431–446. ISSN: 1726-4189. DOI: 10.5194/bg-14-431-2017.

Vonk, J. E. et al. (2015). "Reviews and syntheses: Effects of permafrost thaw on Arctic aquatic ecosystems." In: *Biogeosciences* 12.23, 7129–7167. ISSN: 1726-4170. DOI: 10.5194/bg-12-7129-2015.

Wagner, D., S. Kobabe, E. M. Pfeiffer, and H. W. Hubberten (2003). "Microbial controls on methane fluxes from a polygonal tundra of the Lena Delta, Siberia." In: *Permafrost and Periglacial Processes* 14.2, 173–185. ISSN: 1045-6740. DOI: 10.1002/ppp.443.

Walter Anthony, K. M. and P. Anthony (2013). "Constraining spatial variability of methane ebullition seeps in thermokarst lakes using point process models." In: *Journal of Geophysical Research: Biogeosciences* 118.3, 1015–1034. ISSN: 21698961. DOI: 10.1002/jgrg.20087.

Walter, B. P., M. Heimann, and E. Matthews (2001). "Modeling modern methane emissions from natural wetlands 1. Model description and results." In: *Journal of Geophysical Research-Atmospheres* 106.D24, 34189–34206. ISSN: 2169-897X. DOI: 10.1029/2001JD900165.

Walter, B. P., M. Heimann, R. D. Shannon, and J. R. White (1996). "A process-based model to derive methane emissions from natural wetlands." In: *Geophysical Research Letters* 23.25, 3731–3734. ISSN: 0094-8276. DOI: 10.1029/96GL03577.

Walter, B. P. and M. Heimann (2000). "A process-based, climate-sensitive model to derive methane emissions from natural wetlands: Application to five wetland sites, sensitivity to model parameters, and climate." In: *Global Biogeochemical Cycles* 14.3, 745–765. ISSN: 0886-6236. DOI: 10.1029/1999GB001204.

Walter, K. M., J. P. Chanton, F. S. Chapin III, E. A. G. Schuur, and S. A. Zimov (2008). "Methane production and bubble emissions from arctic lakes: Isotopic implications for source pathways and ages." In: *Journal of Geophysical Research: Biogeosciences* 113.G3, G00A08. ISSN: 0148-0227. DOI: 10.1029/2007JG000569.

Walter, K. M., S. A. Zimov, J. P. Chanton, D. Verbyla, and F. S. Chapin (2006). "Methane bubbling from Siberian thaw lakes as a positive feedback to climate warming." In: *Nature* 443.7107, 71–75. ISSN: 0028-0836. DOI: 10.1038/nature05040.

Wanninkhof, R. (1992). "Relationship between Wind-Speed and Gas-Exchange over the Ocean." In: *Journal of Geophysical Research-Oceans* 97.C5, 7373–7382. ISSN: 0148-0227. DOI: 10.1029/92jc00188.

Wanninkhof, R. (2014). "Relationship between wind speed and gas exchange over the ocean revisited." In: *Limnology and Oceanography-Methods* 12.6, 351–362. ISSN: 1541-5856. DOI: 10.4319/lom.2014.12.351.

Webb, E. K., G. I. Pearman, and R. Leuning (1980). "Correction of flux measurements for density effects due to heat and water vapour transfer." In: *Quarterly Journal of the Royal Meteorological Society* 106.447, 85–100. ISSN: 1477870X. DOI: 10.1002/qj.49710644707.

Wetterich, S., L. Schirrmeister, H. Meyer, F. A. Viehberg, and A. Mackensen (2008). "Arctic freshwater ostracods from modern periglacial environments in the Lena River Delta (Siberian Arctic, Russia): geochemical applications for palaeoenviron-

mental reconstructions." In: *Journal of Paleolimnology* 39.4, 427–449. ISSN: 0921-2728. DOI: 10.1007/s10933-007-9122-1.

Whiting, G. J. and J. P. Chanton (1992). "Plant-dependent CH_4 emission in a subarctic Canadian fen." In: *Global Biogeochemical Cycles* 6.3, 225–231. ISSN: 0886-6236. DOI: 10.1029/92GB00710.

Wickland, K. P., M. T. Jorgenson, J. C. Koch, M. Kanevskiy, and R. G. Striegl (2020). "Carbon Dioxide and Methane Flux in a Dynamic Arctic Tundra Landscape: Decadal-Scale Impacts of Ice Wedge Degradation and Stabilization." In: *Geophysical Research Letters* 47.22, e2020GL089894. ISSN: 0094-8276. DOI: 10.1029/2020GL089894.

Wieners, K.-H. et al. (2019). *MPI-M MPI-ESM1.2-LR model output prepared for CMIP6 CMIP 1pctCO2*. Generic. DOI: 10.22033/ESGF/CMIP6.6435.

Wik, M., R. K. Varner, K. W. Anthony, S. MacIntyre, and D. Bastviken (2016). "Climate-sensitive northern lakes and ponds are critical components of methane release." In: *Nature Geoscience* 9.2, 99–105. ISSN: 1752-0894. DOI: 10.1038/ngeo2578.

Wille, C., L. Kutzbach, T. Sachs, D. Wagner, and E.-M. Pfeiffer (2008). "Methane emission from Siberian arctic polygonal tundra: eddy covariance measurements and modeling." In: *Global Change Biology* 14.6, 1395–1408. ISSN: 1354-1013. DOI: 10.1111/j.1365-2486.2008.01586.x.

Winkler, A. J. et al. (2021). "Slowdown of the greening trend in natural vegetation with further rise in atmospheric CO_2." In: *Biogeosciences* 18.17, 4985–5010. ISSN: 1726-4189. DOI: 10.5194/bg-18-4985-2021.

Wrona, F. J., M. Johansson, J. M. Culp, A. Jenkins, J. Mård, I. H. Myers-Smith, T. D. Prowse, W. F. Vincent, and P. A. Wookey (2016). "Transitions in Arctic ecosystems: Ecological implications of a changing hydrological regime." In: *Journal of Geophysical Research: Biogeosciences* 121.3, 650–674. ISSN: 2169-8953. DOI: 10.1002/2015JG003133.

Yang, X.-Y., J. C. Fyfe, and G. M. Flato (2010). "The role of poleward energy transport in Arctic temperature evolution." In: *Geophysical Research Letters* 37.14, L14803. ISSN: 0094-8276. DOI: 10.1029/2010GL043934.

Yoshikawa, K. and L. D. Hinzman (2003). "Shrinking thermokarst ponds and groundwater dynamics in discontinuous permafrost near council, Alaska." In: *Permafrost and Periglacial Processes* 14.2, 151–160. ISSN: 1045-6740. DOI: 10.1002/ppp.451.

Yvon-Durocher, G., A. P. Allen, D. Bastviken, R. Conrad, C. Gudasz, A. St-Pierre, N. Thanh-Duc, and P. A. del Giorgio (2014). "Methane fluxes show consistent temperature dependence across microbial to ecosystem scales." In: *Nature* 507.7493, 488–491. ISSN: 0028-0836. DOI: 10.1038/nature13164.

Yvon-Durocher, G., C. J. Hulatt, G. Woodward, and M. Trimmer (2017). "Long-term warming amplifies shifts in the carbon cycle of experimental ponds." In: *Nature Climate Change* 7.3, 209–213. ISSN: 1758-678x. DOI: 10.1038/Nclimate3229.

Zabelina, S. A. et al. (2020). "Carbon emission from thermokarst lakes in NE European tundra." In: *Limnology and Oceanography* 66.S1, S216–S230. ISSN: 0024-3590. DOI: 10.1002/lno.11560.

Zhu, Y., K. J. Purdy, Ö. Eyice, L. Shen, S. F. Harpenslager, G. Yvon-Durocher, A. J. Dumbrell, and M. Trimmer (2020). "Disproportionate increase in freshwater

methane emissions induced by experimental warming." In: *Nature Climate Change* 10.7, 685–690. ISSN: 1758-6798. DOI: 10.1038/s41558-020-0824-y.

Zubrzycki, S., L. Kutzbach, G. Grosse, A. Desyatkin, and E. M. Pfeiffer (2013). "Organic carbon and total nitrogen stocks in soils of the Lena River Delta." In: *Biogeosciences* 10.6, 3507–3524. ISSN: 1726-4189. DOI: 10.5194/bg-10-3507-2013.

EIDESSTATTLICHE VERSICHERUNG

Hiermit erkläre ich an Eides statt, dass ich die vorliegende Dissertationsschrift selbst verfasst und keine anderen als die angegebenen Quellen und Hilfsmittel benutzt habe.

Hamburg, February 2022

Zoé Rehder

Hinweis / Reference

Die gesamten Veröffentlichungen in der Publikationsreihe des MPI-M
„Berichte zur Erdsystemforschung / Reports on Earth System Science“,
ISSN 1614-1199

sind über die Internetseiten des Max-Planck-Instituts für Meteorologie erhältlich:
http://www.mpimet.mpg.de/wissenschaft/publikationen.html

All the publications in the series of the MPI -M
„Berichte zur Erdsystemforschung / Reports on Earth System Science“,
ISSN 1614-1199

are available on the website of the Max Planck Institute for Meteorology:
http://www.mpimet.mpg.de/wissenschaft/publikationen.html